DOI:10.15774/PPKE.ITK.2020.001

Tissue Characterization and Custom Manufactured Phantoms for Modelling of Medical Ultrasound Images

Krisztián Füzesi

Supervisor: Dr. Miklós Gyöngy

Faculty of Information Technology and Bionics

Pázmány Péter Catholic University

A thesis submitted for the degree of *Doctor of Philosophy*

2019

DOI:10.15774/PPKE.ITK.2020.001

Contents

DOI:10.15774/PPKE.ITK.2020.001

DOI:10.15774/PPKE.ITK.2020.001

DOI:10.15774/PPKE.ITK.2020.001

List of Figures

DOI:10.15774/PPKE.ITK.2020.001

DOI:10.15774/PPKE.ITK.2020.001

List of Tables

DOI:10.15774/PPKE.ITK.2020.001

Chapter 1

Introduction

Until the end of the previous decade, techniques for manufacturing ultrasound (US) tissue-mimicking materials were limited; also advanced in-house material fabrication techniques were unavailable. Speaking in simple language, as current technology enables one to have a device with higher computational power in the pocket than what a PC had some years ago, similarly, near to industrial level material forming technologies are becoming gradually the part of our everyday life, such as the most common 3D printing technologies: namely Fused Deposition Modelling (FDM) or Digital Light Processing (DLP)-based printing. As there are more and more plastics becoming available along with countless number of 3D printing techniques, our attention turned to them: Why don't we try to use them? Possibly there are some materials, which are able to mimick acoustic properties of tissue. However, why is it relevant to mimic human tissues for ultrasound imaging? Or making a step backwards, as the devil's advocate one can ask: why do we still make research in ultrasound at all? Would not be it more advantageous, to use full-body scans of patients using e.g. computed tomography (CT) or magnetic resonance imaging (MRI), instead of scanning some sector of the body and displaying some (typically) grayscale and strange-looking data to the doctors?

The intention of the author is to clarify these questions in this introduction, providing an easy to follow framework to the reader. The chapter is starting with the motivation behind this dissertation, including the relevance of ultrasound imaging, phantoms and tissue characterization. Also, a brief overview of the dissertation is

DOI:10.15774/PPKE.ITK.2020.001

presented. Next, ultrasound phantom manufacturing methods are discussed. Finally, an overview of tissue thermometry, in particular using ultrasound for temperature mapping is presented.

1.1 Motivation

Motivation of current work stems from the questions: is there a way to learn more about ultrasound imaging systems, including the equipment and the efficiency of image enhancement algorithms as well? Is it possible to experimentally recover the transfer function (also called Point Spread Function - PSF) of an imaging system?

The PSF in US is a signal packet, which is scattered back to the transmit/receive unit (usually called transducer) from a tiny inhomogeneity – at the size of the wavelength of the transmitted signal (usually called scatterer) – in an acoustically transparent medium (usually called propagation medium). For quantitative measurement of the PSF, it would be important to be able to place scatterers arbitrarily in the propagation medium.

The next step is, if we are able to place such scatterers precisely, is it also possible to fully copy the exact scatterer structure of a medical ultrasound image? And if yes, how to do this? If we could provide solutions for these questions, quantitative measurement of the efficiency of image enhancement algorithms on real ultrasound images would become possible.

1.1.1 Relevance of ultrasound imaging

A sound wave having a frequency over the range of human perception (approximately above 20 kHz) is called ultrasound. In nature, many animals use it for navigation, for example bats or dolphins. Using this recognition the first technological application was developed by Paul Langevin in 1917, where the goal was the detection of submarines. [1]

Nowadays, US has a wide variety of applications such as non-destructive testing, range finding, security systems, low energy data-transfer, welding of plastic parts or biomedical applications. [1–5]

DOI:10.15774/PPKE.ITK.2020.001

In medicine US is one of the most widespread medical imaging techniques. In medical imaging the frequency range of 1-20 MHz is usually applied. Since penetration depth and resolution are inversely proportional to each other, lower frequencies are used where higher depths of penetration are required, while higher frequencies will achieve higher resolution at the cost of limited depth of penetration. The main advantage of using US is that it is a non-invasive technique in the classical sense. Namely, only heating and mechanical effects emerge as a safety issue during examinations. Nevertheless, thermal and mechanical indices are always kept under control and displayed on the screen during operation of the imager. [1]

US is cost-effective compared to MRI and CT, and safe compared to imaging methods using ionizing radiation, while its portability is also a key advantage. In common, US, MRI and CT have their spatial resolution at the same magnitude (usually around a millimeter) [6] and can work in real-time, depending of course on the actually employed algorithm running on a computer.

However, while for example in CT-imaging more complex algorithms are aiming to reduce dosage of ionizing radiation and speed up examinations [7], in ultrasound imaging usually algorithms are aiming to acquire more and more detailed and meaningful images while keeping temporal resolution on a reasonable level for real-time imaging [8, 9]. Ultrasound is also useful when fast moving organs like the heart are examined due to its high frame rate [10]. For example combining with Doppler, it is the easiest, cheapest and most safe way to diagnose heart valve disorders [11, 12]. In the other hand, due to its portability and scalability it can practically supply a plethora of medical devices and interventions, ranging from monitoring heat deposition during radiofrequency (RF) ablations [13], measuring distances and volumes inside the body, to superficial, high resolution diagnostic devices like DERMUS (http://dermusvision.com).

There are several sources of noise in ultrasound; image quality is often degraded by the presence of speckle artefact, fatty tissues or heated regions can distort and defocus beams as they are acting as acoustic lens [1, 6].

DOI:10.15774/PPKE.ITK.2020.001

1.1.2 Importance of ultrasound phantoms

In addition to previously mentioned artefacts and noise, it is important to mention that two equivalent subjects of imaging does not exist. This means that using animal models or human volunteers is inadequate to even qualitatively test any properties of an ultrasound imaging equipment [14]. For this reason, ultrasound phantoms are important for checking of image quality and of image resolution enhancement algorithms. Without them current quality of ultrasound imagers and their widespread use would be impossible.

To date, phantom manufacturing methods in ultrasound laboratories are rudimentary. Usually phantoms are built up from a propagation medium having acoustic and physical properties similar to average human soft tissue (speed of sound: 1540 m/s [6]; acoustic attenuation: $0.5 - 1$ dB/cm/MHz; density: 1000 kg/m^3 [15]). As will be shown in Chapter 3, myocardial tissue shows slightly higher speed of sound values and also different acoustic attenuation. For a specific anthropomorphic phantom that mimics heart, values obtained in Chapter 3 would be more relevant. However, those phantoms are usually designed to include the capability of mimicking blood flow as well as heart movement. The topic of the current thesis is limited to general-tissue stationary phantoms, where the goal is to achieve the above mentioned values for the acoustic parameters.

After an adequate propagation medium was chosen that will be usually doped with sub-wavelength scatterers like microspheres, graphite powder [14] or glass beads [16], which - similarly to real human tissues - introduce speckle into the images. The targets - that reflect strong echoes - are usually made of nylon strings or similar 1D structures comparable in size to the wavelength of the beam (< 0.3 mm) [17]. Exact positioning of these strings are possible, however, their number is obviously limited. Another disadvantage that only the Line Spread Function (LSF) could be extracted instead of the PSF, which is the transfer function of the imaging system. These phantoms are often used for calibration and other quality assurance purposes on imaging equipment [18]. Other type of phantoms are tissue-mimicking phantoms, which can be used for example for training of radiologists or research purposes, e.g. qualitative testing of algorithms. Here acoustic properties are usually tuned on a

DOI:10.15774/PPKE.ITK.2020.001

macroscopic level; the aim is to create a medium similar in shape and size to organs of the human body.

In summary, current phantoms are capable of mimicking a part of human body on a macroscopic scale and are adequate for qualitative and some quantitative tests as well. However, current phantoms lack fully customizable scatterer structure, thus the PSF of a system is unknown (usually modelled using computer simulations) and for this reason, performance of algorithms can be only tested qualitatively.

1.1.3 Importance of tissue characterization

Good quality phantom design relies on accurate characterization of human tissue. With the widespread adoption of rapid prototyping techniques, a plethora of new materials has appeared for 3D printing. Tissue characterization methods could be also used to characterize these potential tissue-mimicking materials. The most important parameters are the speed of sound and acoustic attenuation, and depending on the exact application, their temperature and frequency dependence as well. The density and the speed of sound determines the characteristic acoustic impedance (Z) of a medium. (For a detailed discussion, see the next chapter.) Based on these properties macroscopic acoustic features of human tissue could be mimicked sufficiently.

Precise characterization is also important for the accurate functioning of advanced ultrasound imaging methods such as ultrasound-based thermometry, which should be sensitive for very small changes (e.g. speed of sound change around 1 m/s).

1.1.4 Overview of current thesis

Here, a brief overview of the following sections and chapters are presented to help the reader.

In the remaining two sections of this chapter, an introduction to medical phantoms and their manufacturing methods, as well as an introduction to tissue thermometry, are given.

DOI:10.15774/PPKE.ITK.2020.001

In Chapter 2, the theory of ultrasound imaging is presented, starting with an overview of ultrasound imaging itself. This is followed by sections where physical principles behind the current work are introduced and derived. Finally, characterization of speed of sound and attenuation and the use of Kramers-Kronig relation in ultrasound are discussed.

In the further chapters, the scientific work of the author is presented. In Chapter 3, the temperature and frequency dependence of speed of sound and attenuation in porcine myocardium are presented.

In Chapters 4 and 5, the applicability of 3D printing techniques in US tissue mimicking are shown.

In Chapter 4, two cost-effective, widespread methods (FDM and DLP) are presented as an alternative of currently used calibration phantoms. Here 2D patterns were created, using strings between two supporting walls.

In Chapter 5, an advanced, high resolution 3D printing method (photopolymer jetting - PJ) was used to create arbitrary 3D scatterer distributions. Using such phantoms an image enhancement algorithm was quantitatively tested. Finally, an algorithm is presented, which was developed to create scatterer maps to mimic real ultrasound images. The algorithm allows to tailor properties of the scatterer maps to the printer, like density (spacing) of scatterers.

1.1.5 Declaration of original work used

In this subsection the main references of the current thesis are shown, including the publications of the author, which gives the main basis for the corresponding chapters or sections.

Section 1.2 is based on a part of the Master Thesis of the author [19], which is itself based on [14]. The information used to write Section 1.3 were taken primarily from [20].

In Chapter 2 (Theory of Ultrasound Imaging), Section 2.1 is also partially based on the Master Thesis of the author [19]. In Chapter 2 the further two sections, presenting the derivations of the linear wave equation and scattering are based on [1, 21, 22] and [23], respectively. The discussion of the Kramers-Kronig relation

DOI:10.15774/PPKE.ITK.2020.001

(Subsection 2.5.3) is based on [23, 24].

The further chapters rest on the scientific work of the author published recently in peer-reviewed journals or in conference proceedings as follows. Chapter 3 is based on [25]. Chapter 4 is based on [26]. In Chapter 5, two conference publications are used as a basis of the text; Section 5.3 relies on [27]. The paper, which provides the basis for Section 5.4 was published at ICU 2017 conference [28].

1.2 Overview of medical phantoms

The aim of this section is to provide the reader a brief summary of the currently used phantoms and phantom manufacturing methods in particular for ultrasound imaging. As mentioned in 1.1.5, the following overview is based on [14].

The idea of phantoms was born in the beginning of the 20th century. After X-ray imaging started to spread and people realized the harmful effects of ionizing radiation the need for tissue substitutes were raised to measure the effects of kilo and megavoltage beams. While in X-ray and CT the most important feature was dosimetry in the first times, quality assurance (QA) became more and more important there and in other imaging modalities (MRI, US, PET) as well. First, very simple phantoms were constructed, e.g. baths filled with water or wax . These were applicable for image uniformity and dosimetry measurements. As materials developed to be more reliable and manufacturing methods evolved as well, reproducibility of more complex phantoms became available, introducing some inhomogeneities inside the imaged volume. Thus, these phantoms could fulfil several QA requirements. As an example, the most general of these are resolution and contrast measurements, where distinctness of two objects in the region of interest are investigated by the means of spatial distance and signal intensity respectively.

Besides QA, another aim of phantoms is the help of the training of radiologists. In both cases, a phantom is intend to mimic different physical and radiological properties of human tissue. Movement of organs or the patient (e.g. in CT or MRI) can also be simulated using advanced phantoms.

Exact design of a phantom is specific to its purpose. For example in radiography

DOI:10.15774/PPKE.ITK.2020.001

dosimetry phantoms must contain at least one dosimeter placed inside, which in some cases can be moved as well. There are also several types of dosimeters, which could be chosen based on exact design specification of the current phantom. Another example is resolution and image quality measurements, where typically rod or wire targets are placed in a phantom to predefined locations.

1.2.1 Manufacturing of ultrasound phantoms

The first ultrasound phantoms were simple containers with metal rods at specific locations, filled with water providing distance calibration of ultrasound equipment. The evolution of ultrasound devices demanded better materials with specified and more accurate speed of sound and attenuation that are similar to the properties of living tissue.

These phantoms are useful in ultrasound quality control, and helps better our understanding of the exact physics of ultrasonic wave propagation in tissues that influence imaging performance. Therefore some phantoms are made for experimental purposes, for example to measure attenuation, backscatter, and ultrasound exposimetry or bulk material characteristics.

There are three key parameters of ultrasonic phantoms that significantly influence the performance: (1) speed of sound in the phantom, (2) acoustic attenuation (including frequency-dependent attenuation) and (3) scattering (for detailed discussion, see next chapter). There are also other physical parameters like nonlinearity (B/A parameter), but these are not critically important for successful tissue mimicking when applying baseband frequency of the imager. Importance of nonlinear parameters emerges when considering harmonic imaging, however, this is beyond the subject of the current thesis, thus not detailed further. Various methods have been published to prepare “in-house” phantoms made of several materials for teaching and for equipment verifications. The advantage of these phantoms is their low cost and ease of preparation. Nevertheless, the absolute verification of acoustic properties is lacking. [18]

DOI:10.15774/PPKE.ITK.2020.001

Material	Speed of sound [m/s]	Attenuation [dB/cm/MHz]	Impedance [MRayl]	Ref.
Agarose-based	$1498 - 1600$	$0.04 - 1.40$	$1.52 - 1.76$	[14]
Avg. Soft Tissue	1540	$0.5 - 1$	$1.5 - 1.7$	[6, 15]
Gelatin-based	$1520 - 1650$	$0.12 - 1.50$	$1.60 - 1.73$	[14]
Oil Gel-based	$1480 - 1580$	$0.4 - 1.8$	$1.54 - 1.67$	[14]
PAA-based	1540	0.7 @$5MHz$	1.7	[14]
Polyurethane	1468	0.13	1.66	[14]
PVA-based	$1520 - 1610$	$0.07 - 0.35$	$1.60 - 1.77$	[14]
PVC-based	$1270 - 1580$	n.a.	n.a.	[19, 29]
PJ FC	1617	39 @$20MHz$	1.87	[30, 31]
PJ VW	2633	110 @$20MHz$	3.1	[30, 31]
Silicone	1030	14.0 @$5MHz$	1.1	[32]
Urethane Rubber	1460	$0.5 - 0.7$	1.31	[14]
Zerdine®	1540	$0.5 - 0.7$	n.a.	[14]

Table 1.1: Acoustic properties of US phantom manufacturing materials. The abbreviations are as follows: PAA – polyacrylamide; PVC – polyvinylchloride; PJ – photopolymer jetting (3D printing technology), FC – Full Cure, which is a support material for PJ 3D printing; VW – VeroWhite, which is a printing material for PJ 3D printing. Urethane Rubber and Zerdine® are two materials used in commercial phantoms.

Overview of US phantom materials

There are many phantom materials, which are used primarily to prepare "in house" phantoms or for common use. Some of them are discussed in this paragraph. In the text they are presented qualitatively. A quantitative overview is made in Table 1.1.

Gelatin-based phantoms were widely used as 'in house' tools, whose raw material is a homogenous colloid gel derived from collagen – which was extracted from animal tissues – and was one of the earliest attempts to mimic tissues. These can be mixed with alcohol to adjust the speed of sound and graphite powder to adjust scattering.

DOI:10.15774/PPKE.ITK.2020.001

The phantom should be stored in benzoic acid in order to avoid bacterial pollution. The advantage of this material is the relatively good speed of sound and durability at room temperature, when stored in distilled water. It is also cost effective and easy to manufacture. Disadvantages are the temperature sensitivity, the sensitivity against bacteria and the difficulty to achieve uniform scattering.

Another option is the most widely used agarose-gel based techniques. There is also graphite powder used to adjust attenuation and scattering properties. The advantages are the well-characterized performance, the ease and flexibility of the preparation, which allows mixing of several other ingredients to achieve a range of acoustic properties. Recent papers also published on fine-tuning [33] and temperature dependence of acoustic parameters [34] of agarose phantoms. The disadvantages are that agarose phantoms require careful handling, because it is easy to damage, microbial invasion and drying can also occur during storage like in the case of gelatin-based phantoms.

Oil-gel based tissue substitutes containing propylene glycol, a gelatinizer and polymethyl-methacrylate (PMMA) microspheres are also used [14] for phantom manufacture. Their advantages are the immunity to bacterial infection and relatively good physical properties. Unfortunately, since this solution is very rarely used, few information is available about the ease of preparation and applicability.

Polyacrylamide-based phantoms made of acrylamide monomer have speed of sound around 1540 m/s but are highly toxic, and need special precautions.

Polyurethane (PU) phantoms have relatively good physical properties; they are durable and have immunity from bacterial invasion. The disadvantage is that its molecular structure is complex, therefore the standardization is harder, but nowadays 3D printing could give an acceptable solution for standardization. In my previous work [19] PU also investigated using FDM printing, however, with low success factor. The main problem was presumably the air stucked between layers and printed threads.

Polyvinyl-alcohol (PVA) based tissue substitutes have also good physical properties and durability, but the disadvantage here is the emerging difficulties during preparation. It needs several freeze-thaw cycles.

DOI:10.15774/PPKE.ITK.2020.001

Silicone was also tested as a material of phantoms because its durability, but it has very low speed of sound and high attenuation, especially in high (above 10MHz) frequencies [14], however, found to be very stable over time and could be suitable for training purposes [32].

Commercially used materials are agarose (preservative technique used, 48 months warranty), Zerdine® (a patented solid elastic material), urethane rubber and thermoplastics. [35]

In our lab, agarose-gel based phantoms are typically used, but the problem is that they are sensitive to physical contact. In addition, due to their high (95−99%) water content, they are liable to drying out, which manifests in damage and extreme size reduction. An alternative could be PVC, which compared to other available materials for "in house" phantom manufacturing has several advantages, for example its chemical resistance and durability. It can be in contact with acids, leaches, oil and petrol, it is also heat resistant in some measure (usually below 80 °C). Moreover it has a low water absorption, which makes it suitable for underwater ultrasonic measurements. Its speed of sound is lower ($\sim$ 1400 m/s) than propagation speed in average soft tissue ($\sim$ 1540 m/s), however, it is still considered a proper tissue mimicking material. The main drawbacks are that toxic fumes could be formed during its manufacture and the acoustic properties of the final product largely depends on the exact heat-dose what the material suffered, moreover the storage of the phantom is circumstantial due to the softener base used [19, 36]. This softener base gives the majority of these phantoms that also affects longevity of them, as over time leakage of the softener base is observed [19], which affects speed of sound of the propagation medium.

Acoustic characterization of thermoplastics used for 3D printing in ultrasound phantoms were also lacking, however, polyurethane has the same positive properties as PVC that also turned our attention to investigate 3D printing techniques. Nowadays, 3D printing is mostly used to create mold and vasculature for anthropomorphic US phantoms [37, 38], or to create bone-mimicking materials [39–43]. In Chapter 4 applicability of these materials for filament target phantoms are investigated. Recent paper of Jacquet et. al. [30, 31] reported the use of special 3D

DOI:10.15774/PPKE.ITK.2020.001

printing photopolymer materials as propagation medium as well. Using a similar technique, the work of the author on the quantitative performance analysis of image restoration methods and manufacturing phantoms with fully customizable scatterer structure are presented in Chapter 5.

1.3 Overview of tissue thermometry

The aim of current section is to provide the reader a brief introduction to tissue thermometry techniques and their relevance both using MR, CT and in particular ultrasound imaging. As mentioned in 1.1.5, the following overview is based on [20]. Nevertheless, the current section is an outlook from the main subject of the dissertation, it is aimed to place the topic of Chapter 3 into context.

There are several procedures in medicine where the intervention involves heating or cooling of tissue. There is a plethora of ablation methods, including radiofrequency-, microwave-, laser-, cryo-, and ferromagnetic ablation, irreversible electroporation and high intensity focused ultrasound (HIFU) as well [44–46].

Tissue thermometry methods are essential, as they make it available to track actual condition of the medical intervention, since the result of the above mentioned treatments are mainly related to the temperature distribution. Using thermal information of the tissue, the medical staff is able to judge which part of tissue remains healthy and which part suffer irreversible changes. Thermal therapies could lead to instant cell death (necrosis), or initiating programmed cell death (apoptosis) – in both cases, the goal is the destruction of undesirable tissue, which is in most of the cases a tumor. Nowadays, minimally invasive – or if available – non-invasive techniques becoming more and more popular, thus for temperature measurements non-invasive techniques are favorable as well [47].

The main aspects choosing between imaging modalities for thermometry are including patient safety, costs, availability, ease of use and compatibility with other devices. Also, the sensitivity, tissue dependence and spatio-temporal resolution are important parameters.

There are three main techniques described below, which are able to acquire data

DOI:10.15774/PPKE.ITK.2020.001

deep inside the tissue.

The first one is CT-based techniques. Here the advantages are the compatibility of the imager with other devices, relatively low cost and wide availability of CT machines. However, it is important to note that in this case the patient is exposed to harmful ionizing radiation. The X-ray dose can be reduced with image reconstruction algorithms [7], in turn the result of the temperature measurement could be distorted due to artefacts of image reconstruction [20, 46].

MR-based techniques are precise tool of temperature monitoring, although the high cost, the limited availability of these machines and difficulties in compatibility are obstructing their usage. For example, during a surgery all used equipment should be non-magnetic and all of the instrumentation should be resistant for such enormous magnetic fields, which are further increasing the cost of interventions monitored by MRI [46, 48, 49].

The final group of noninvasive methods are ultrasound-based techniques. US has a relatively low cost, and similar spatial resolution to CT and MR – both performing around some millimeter [20, 45, 49, 50]. However, US thermometry techniques suffer from high tissue-dependence. Nevertheless, US is a safe imaging modality and used many times for guidance of medical equipment inside the body. Once it is used for imaging, it would be also practical to use for thermometry.

1.3.1 Non-ultrasound thermometry

Theoretical background of CT based thermometry

In computed tomography slices of the body are insonified with X-ray radiation. Data is displayed based on measuring the linear attenuation coefficient of insonified materials. Applying a linear transformation, Hounsfield Units (HU) – or in other words CT numbers – are extracted for each pixel:

$$CT(x,y) = 1000\frac{[\mu(x,y)) - \mu_{H_2O}]}{\mu_{H_2O}} \tag{1.1}$$

where $\mu(x,y)$ is the average linear attenuation coefficient at pixel position (x,y) and μ_{H_2O} is the linear attenuation coefficient of water. Temperature measurement

DOI:10.15774/PPKE.ITK.2020.001

with CT is based on thermal expansion – and hence, density change – of heated tissue. Rate of density change is given by the following equation:

$$\rho(T) = \frac{\rho(T_0)}{1 + \alpha\Delta T} \tag{1.2}$$

where T_0 is the calibration temperature of the CT machine, α is the volumetric expansion coefficient, which is characteristic of the material, and ΔT is the temperature difference between T and T_0.

The change in linear attenuation coefficient can be calculated as:

$$\mu(T) = \mu_m \rho(T) \tag{1.3}$$

where μ_m is the mass attenuation coefficient and $\rho(T)$ is the density of the material at temperature T.

In summary, the density, and with this, the CT number will decrease as temperature increases as follows:

$$CT(T) = CT(T_0) - \frac{100\mu(T_0)\alpha\Delta T}{\mu_{H_2O}(T_0)} \tag{1.4}$$

This relation is well illustrated in Figure 1.1, which is adopted from [20].

Theoretical background of MR thermometry

In MR imaging, the resonance frequency of protons is temperature dependent, while the temperature measurements are tissue independent, except fatty tissues. The reason for this difference is while in water the proton resonance frequency is $\alpha = 0.01$ ppm/°C (also called the proton resonance frequency shift coefficient), the proton resonance frequency in lipids are independent from temperature. [50]. The relation between proton resonance frequency phase shift $\Delta\phi$ and temperature change ΔT is given by the following equation [45]:

$$\Delta\phi = -\Delta T \cdot 2\pi \cdot \alpha \cdot \psi \cdot B_0 \cdot TE \tag{1.5}$$

where ψ is the gyromagnetic ratio, B_0 is the magnetic field and TE is the echo time. So, the proton resonance frequency phase shift will be negative if the temperature is rising.

DOI:10.15774/PPKE.ITK.2020.001

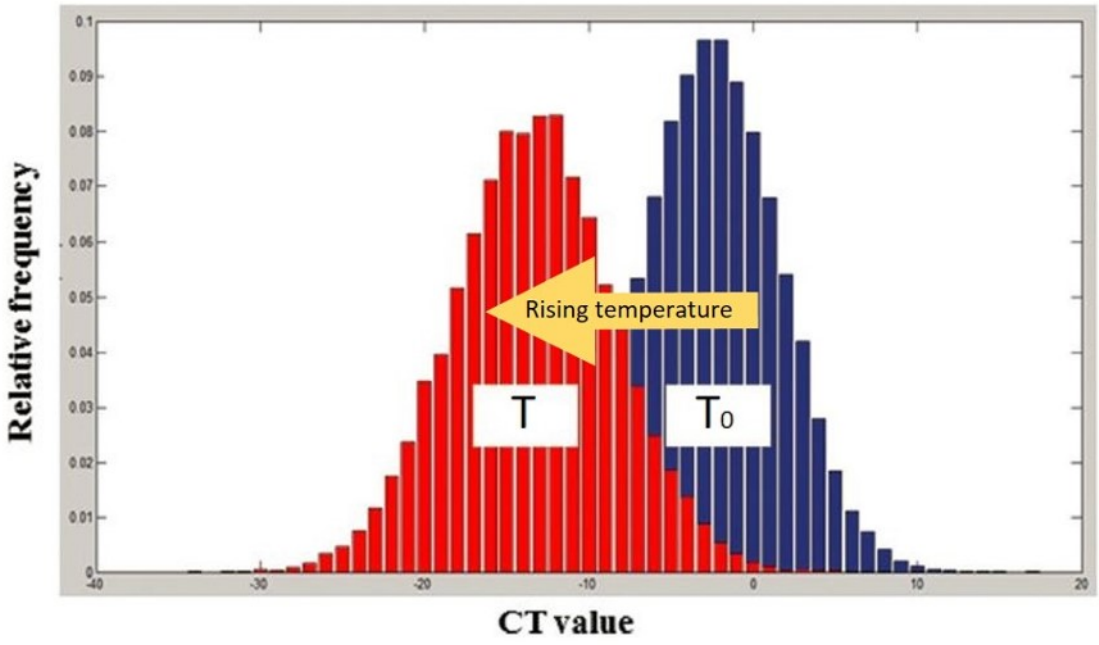

Figure 1.1: Change of CT value histograms in a water phantom. T_0 corresponds to histogram at calibration temperature and T is the histogram at $T_0 + \Delta T$. Source of figure: [20]

1.3.2 Ultrasound-based thermometry

In ultrasound imaging, thermometry is usually carried out using the knowledge of the speed of sound at ambient temperature inside tissues (generally assumed to be 1540 m/s in soft tissues [13]). Here, similarly to MR imaging, fatty tissues introduce difficulties in temperature monitoring. In normal soft tissues speed of sound is increasing parallel with temperature up to 50-60 °C, and the attenuation coefficient becoming lower simultaneously [51]. This trend turns to the reverse at higher temperatures, moreover, during the cooling back of the previously heated tissue, these values usually does not follow the course which was obtained during heating, due to the irreversible changes in treated tissues. Heat expansion here also plays an important role, as the distance between scatterers becoming bigger.

Active ultrasound

One approach using active ultrasound is temperature monitoring, using channel data delays. As it was mentioned previously, an increase in temperature causes an

DOI:10.15774/PPKE.ITK.2020.001

increase in speed of sound of non-fatty tissues. This phenomena will decrease arrival time of the signal where this backscattered beam crosses the heated regions of tissue.

There are examples, where the used tissue model is simple; consist of regions, heated transversely to the imaging plane [13]. To build such models, knowledge of temperature dependence of imaged tissue is essential.

Having the knowledge of temperature dependence of tissue, these simple models can be built and practical to use, when considering a smaller region. In this specific example, monitoring of cardiac radiofrequency ablation was investigated using a transoesophageal (TEE) and an intra-cardiac (ICE) probe. Their aperture are in the range of the extent of heated area, which confirm the choice of the model.

If the aperture is bigger (e.g. a commonly used phased array is employed), there are several techniques, such as speckle tracking, to investigate smaller region of interests. Speckle is usually undesirable, and considered a kind of noise, which makes the images grainy. The phenomenon is arising from sub-wavelength size scatterers. Thus, in thermometry one can benefit from speckle patterns, as it allows to estimate tissue motion and deformation with high resolution. [50] The estimation of echo-shift is obtained by determining the peak of cross-correlation between consecutive frames (at t and $t + 1$).

There are some artefacts, which are limiting the accuracy of such temperature monitoring systems. Usually these models are ignoring thermal lensing artefacts and assume tissue heterogeneity. Thermal lensing artefact occurs when the backscattered beam travels through the heated area. As temperature gradients are higher, this distortion is becoming stronger. Using spatial compounding, it is possible to reduce the effect of lensing at the cost of temporal resolution.

As mentioned earlier, the difference between tissues – in particular muscle and fat – can significantly distort the results of such algorithms as they rely on a specific tissue model. In reality both temperature dependence of speed of sound and acoustic attenuation greatly varies from tissue to tissue. The solution is usually to introduce a post-processing algorithm taking into account some known constraints about temperature fields. [50]

DOI:10.15774/PPKE.ITK.2020.001

Passive ultrasound

Passive ultrasound thermometry is based on receiving acoustic radiation from the tissues without any acoustic transmission from the imaging transducers. The main difficulty here is that the received signal has very low amplitude compared to active ultrasound methods. Therefore, it usually requires a more complex model, to exclude noise and exclude information outside from the region of interest and acquisition takes much more time usually as well. The basic difference is that in active ultrasound one knows the exact time of sound emission, meanwhile in passive ultrasound one has only a receiver unit without the knowledge of the depth of the incoming signal explicitly.

In passive ultrasound, one can measure natural signals radiated by the human body, or in another hand, it can be used to monitor e.g. HIFU treatment. In the first setup, radiation is emitted by chaotic motions inside tissues, which system usually called as an acoustic black body [48, 49]. In the case of HIFU treatment, region of interest (ROI) is irradiated using a high Q number transducer – which means it is emitting long pulses with a very short bandwidth. Thus, cavitation is induced in the ROI. As the focal region is usually a small spatial region (several mm^3), the transducer should be moved to destroy all the undesired tissue. For this reason, the time of treatment should be several hours long. During such long treatments, except CT all modalities mentioned in this review are suitable to detect the changes inside, however, it is reasonable to use a method, which does not introduce additional acoustic beam into the ROI. Hence, one convenient way to measure effects of HIFU treatment is using a transducer (-array), which passively detects these changes. The receiver array practically placed transversely to the HIFU beam. [44]

Optoacoustics

Optoacoustics is a phenomena, where a light source irradiates a boundary of the body (this can be the skin, or the intestinal wall using as transrectal probe [47] as well). When the light waves reach such a boundary, some part of it is converted into acoustic energy. During heating or cooling the tissue, the thermoacoustic efficiency (Grüneisen parameter) changes in a linear fashion. Petrova et. al. [47] has

DOI:10.15774/PPKE.ITK.2020.001

shown that heat monitoring in highly vascularized tissue can be done, due to the exclusive compartmentalisation of absorbing molecules in hemoglobin. Moreover, this temperature-dependent optoacoustic response was found to be independent of oxygen saturation of blood – so the same response could be obtained from both arterial and venal blood.

1.3.3 Tissue thermometry for cardiac interventions

Nowadays, the most widespread method of cardiac interventions is RF ablation, where different types cardiac arrhythmias are usually cured with high (>95 %) success rate and low morbidity rates [52, 53]. During the intervention current flows through cardiac tissue, heating it due to its electric impedance. It is of major importance to measure temperature in the treated area, to minimize side-effects and complications. Usually, the temperature should not exceed 100 °C to avoid tissue boiling – that means the measured temperature should stay below 70 °C due to temperature measurement uncertainty – which could cause intramyocardial superheating, 'pop' lesions [52] and bleeding of tissue [54]. The standard technique for thermometry is using temperature sensors, usually built in the catheter tip [52]. The main issue with this approach is that the temperature deviation inside the tissue could only be estimated based on the temperature measured on the surface. As it is a living system with great fluid motion, the cooling effect of the blood is also present, which makes this type of temperature monitoring more uncertain. It is also a known issue that RF intervention can cause oesophageal lesion formation and further complications. For this reason, more precise temperature monitoring techniques would be essential. In the literature there are several investigations, where oesophageal lesion formation is intended to be excluded and oesophageal temperature probes were included in the monitoring of the interventions [55,56]. However, Müller et. al. [57] highlights that the use of these probes used for monitoring luminar oesophageal temperature is controversial, as they appears to be a risk factor for the development of oesophageal lesions.

Other approaches are injectable micro-size temperature sensors [58] or IR thermometry, recently presented by Daly et. al. [59]. However, here ultrasound ther-

DOI:10.15774/PPKE.ITK.2020.001

mometry could be a nice alternative as it has been also shown by Pasternak et. al. [13], as a small transducer would be possible to be inserted into the catheter and knowledge of temperature distribution in the axial dimension would be appropriate to avoid – or at least further decrease the occurrence of – above mentioned complications.

1.3.4 Summary

In summary, the main concept behind image modalities, which are suitable for deep-tissue thermometry, were shown. These are CT, MR and ultrasound. The general advantages and limitations of each were discussed. Each methods can have a spatial resolution around 1mm and provides real-time imaging of the ROI, except some techniques using passive ultrasound where the temporal resolution can be even 1 minute. Finally, an overview of tissue thermometry methods used during cardiac interventions is given, mentioning the opportunities given by ultrasound as well.

DOI:10.15774/PPKE.ITK.2020.001

Chapter 2

Theory of Ultrasound Imaging

2.1 Overview of ultrasound imaging

The basic concept of ultrasound imaging consists of three steps: first, a transducer transforms a short, high voltage ($\sim$ ns, 100 V) electric signal into a high frequency ($\sim$ MHz) longitudinal pressure wave in a medium; the waves propagate throughout the medium, some of which is scattered or reflected back to the transmitting transducer (or reaches another receiver transducer, depending on the actual setup). Finally, the receiving transducer converts back the pressure changes into an electrical signal, which can then be processed to form an image of the medium properties, such as of the scattering strength distribution in the medium.

The most common type of ultrasound images is the so called B-mode (brightness-mode) image, where the amplitude of the received signal is converted into a grayscale image. The depth that can be seen on these images calculated from the arrival time of the received signal: if the reflector was in a deeper region, the backscattered signal arrives later. To be able to transform time to distance in a trustworthy way, the exact speed of sound of the examined tissue (or other material) must be known or at least well estimated. (Note: the speed of sound in this paper always refers to the propagation velocity of the above-mentioned longitudinal waves in a medium.) For conciseness this introduction will not go into other ultrasound image types, most of them similarly need knowledge of the speed of sound.

One of the basic properties of ultrasound devices is their center frequency that

DOI:10.15774/PPKE.ITK.2020.001

highly influence the resolution and penetration depth. These two are inversely proportional, and this gives the most important limitation of ultrasound imaging: if deeper structures are aimed to be imaged, lower frequencies are used and the resolution worsens.

There are two main sources of backscattered energy defined: scattering and reflection. Scattering is usually referred as the interaction of the sound wave with particles smaller than the wavelength, while reflection is such an interaction with particles or objects greater than the wavelength. Both effects are related to the change of density and compressibility of the materials in the way of wave propagation and described by the scattering wave equation (see Section 2.3).

Reflection of waves from the interface of two media is described by the reflection coefficient. The reflection coefficient can be derived from the characteristic acoustic impedances (Z) of the two neighbouring media. Characteristic acoustic impedance (Z) could be derived from the linear wave equation (see Section 2.2), and is specified by the speed of sound (c) and the density (ρ) of a medium:

$$Z = \rho \cdot c \tag{2.1}$$

Consider a planar wave travelling from medium 0 to medium 1, having acoustic impedances of Z_0 and Z_1 respectively. The reflection coefficient r describing the proportion (in terms of amplitude) of an incident pressure wave reflected from the interface between two media as follows:

$$r = \frac{Z_1 - Z_0}{Z_1 + Z_0}, \tag{2.2}$$

The above means that in terms of amplitude $1 - r$ part of the incoming wave propagates further into the next medium (acoustic impedance of it is signed as Z_1), the proportion of r is reflected back to medium 0 (having an acoustic impedance of Z_0). [6]

One important consequence of this relation that ultrasound is best suited to visualize soft tissue, as some structures – for instance bone or airy lungs – are difficult to examine due to the excessively high acoustic impedance contrast with surrounding soft tissue.

DOI:10.15774/PPKE.ITK.2020.001

During the development of ultrasound imaging devices or methods, it is often necessary to test the device or method using an object whose properties (mainly speed of sound, attenuation, characteristic acoustic impedance) are similar to tissue, which is, nevertheless, standardized in some way, thus the operator knows what is imaged. When testing for specific image quality metrics of the imaging system, such objects are called calibration or quality assessment (QA) phantoms; these can also be used to assess the degradation of a transducer performance with time. Phantoms may also be used to model human anatomy and tissue characteristics – called anthropomorphic phantoms – which can be useful for training ultrasound technicians in a comfortable environment [18]. This is especially useful when training for uncomfortable and technically demanding procedures such as needle biopsies and rectal examinations.

To manufacture phantoms that fit our purpose, it is first important to know how the physical system works, what is aimed to be mimicked. For this reason, in the next sections the linear wave equation – an idealized but well-working model of pressure wave propagation – is derived first. Thereafter the scattering wave equation is shown briefly, which shows how an inhomogenous system could be modelled. Based on these, modelling of image formation is presented. Finally, measurement methods of two main phenomena of ultrasound; speed of sound and attenuation are shown complementing the chapter with their linking through the Kramers-Kronig relation.

2.2 Modelling of propagation using linear wave equation

As mentioned in 1.1.5, the following derivation is based on [1, 21, 22].

In the current thesis only the fundamental frequency of ultrasound imagers are used. Avoiding the use of harmonic imaging allows us to consider the homogenous linear wave equation (LWE) as a good approximation of the underlying physical processes of the examined systems.

However, it is important to note which assumptions and simplifications are made

DOI:10.15774/PPKE.ITK.2020.001

to be aware of the limitations of this model. The theory of LWE are best fit for ultrasound pulses travelling in idealized – lossless and homogenous – media. Generally, in soft tissues (but not in hard tissues, such as bone) high frequency shear waves can be neglected due to the high rate of absorption (a factor of 535 for each wavelength travelled [23] p. 87). Due to this simplification, ultrasound wave propagation can be described by a scalar pressure field. However, it should be noted that scalar waves are also affected by attenuation (on the order of 0.5 dB/cm/MHz in tissue, as described in the previous chapter, Section 1.1), which effect in the following derivation is ignored for simplicity. For a discussion of various attenuation phenomena and its effect on wave propagation, please see [6] Chapter 4.

To derive the LWE, the three governing equations of acoustics first need to be derived, namely: I. State equation, II. Continuity equation, III. Force equation.

I. State equation

When a wave propagates through a medium, the local density will change with pressure. This relation is generally superlinear (growing faster than a linear relationship); however, if the changes in density (ρ) and pressure (p) are small compared to the environmental set points ρ_0, p_0, the relationship can be approximated as linear:

$$p_{total} = p_0 + p\,,\; p << p_0 \tag{2.3}$$

$$\rho_{total} = \rho_0 + \rho\,,\; \rho << \rho_0 \tag{2.4}$$

Expecting a linear relationship, the pressure (p) could be expressed as:

$$p = \varepsilon\rho \tag{2.5}$$

where ε is a constant and could be expressed from ρ_0 and the compressibility of the medium κ or its inverse; the elastic modulus K:

$$\varepsilon = \frac{1}{\kappa\rho_0} = \frac{K}{\rho_0} \tag{2.6}$$

DOI:10.15774/PPKE.ITK.2020.001

II. Continuity equation

The continuity equation is based on the principle of conservation of mass. Let us suppose we have a cubic control volume V with dimensions $dx \cdot dy \cdot dz$ (see Figure 2.1).

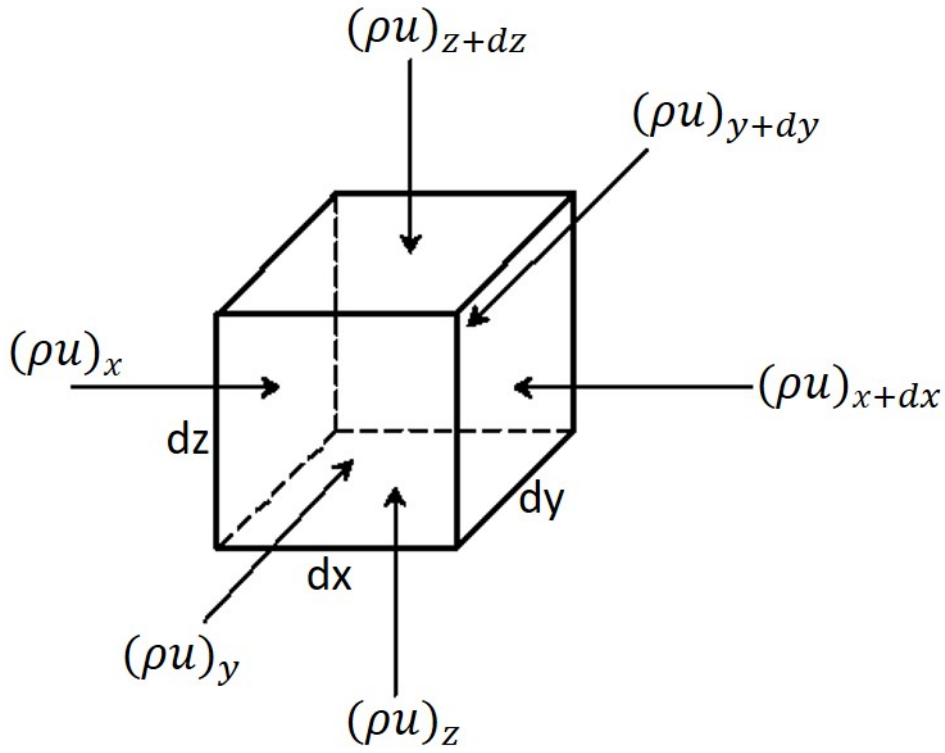

Figure 2.1: Pressure wave acts on a cubic control volume. The pressure change will induce density change of the faces of the cube combined with particle motion. The figure is adopted from [22] .

The mass entering the control volume from face x eqauls:

$$\dot{m}_x = \rho_{total} \vec{u}_x \, dy \cdot dz \tag{2.7}$$

where $\vec{u}$ denotes 'particle velocity'; which describes the local motion of small elements of the medium displaced by the pressure. We can use the Taylor series expansion for the mass entering the face at $x + dx$:

$$\dot{m}_{x+dx} = \dot{m}_x + \frac{\partial \dot{m}_x}{\partial x} \, dx + ... \cong \rho_{total} \vec{u}_x \, dydz + \frac{\partial \rho_{total} \vec{u}_x}{\partial x} \, dx \cdot dy \cdot dz \tag{2.8}$$

DOI:10.15774/PPKE.ITK.2020.001

Applying this to all directions, the total mass gain per V could be written as:

$$\begin{aligned}\dot{m}_{total} &= \dot{m}_x - \dot{m}_{x+dx} + \dot{m}_y - \dot{m}_{y+dy} + \dot{m}_z - \dot{m}_{z+dz} \\ &= \left(-\frac{\partial \rho_{total} \vec{u}_x}{\partial x} - \frac{\partial \rho_{total} \vec{u}_y}{\partial y} - \frac{\partial \rho_{total} \vec{u}_z}{\partial z} \right) dx \cdot dy \cdot dz\end{aligned} \tag{2.9}$$

We know also that the mass gain in V could be written as:

$$\dot{m}_{total} = \dot{\rho}_{total}\, dxdydz = \dot{\rho}_{total}\, dV \tag{2.10}$$

Thus, comparing equations 2.9 and 2.10 the following could be written:

$$\dot{\rho}_{total}\, dV = -\nabla \cdot \rho_{total} \vec{u}\, dV \tag{2.11}$$

From this (original) form of the continuity equation, using Equation 2.4, after simplification and linearisation the final form will be:

$$-\rho_0 \nabla \cdot \vec{u} = \frac{\partial \rho}{\partial t} \tag{2.12}$$

III. Force equation

For the investigation of the conservation of momentum we use Newton's law. In the calculations the applied force can be derived from the acceleration $\vec{a}$ of particles as follows:

$$d\vec{f} = dm \cdot \vec{a} = dm \frac{\partial \vec{u}}{\partial t} \tag{2.13}$$

where dm is the mass of the control volume and equals $\rho_{total}\, dV$.

As can be seen in Figure 2.2, using the pressure, the net force acting in the x direction could be written as:

$$d\vec{f}_x = p_{total}(x)\, dydz - p_{total}(x + dx)\, dy \cdot dz \tag{2.14}$$

Using Taylor series expansion, the force acting on $x + dx$ face could be expanded as:

$$p_{total}(x + dx) = p_{total}(x) + \frac{\partial p_{total}}{\partial x} + ... \tag{2.15}$$

Thus, the net force acting in the x direction could be rewritten as:

$$d\vec{f}_x = -\frac{\partial p_{total}}{\partial x}\, dx \cdot dy \cdot dz \tag{2.16}$$

DOI:10.15774/PPKE.ITK.2020.001

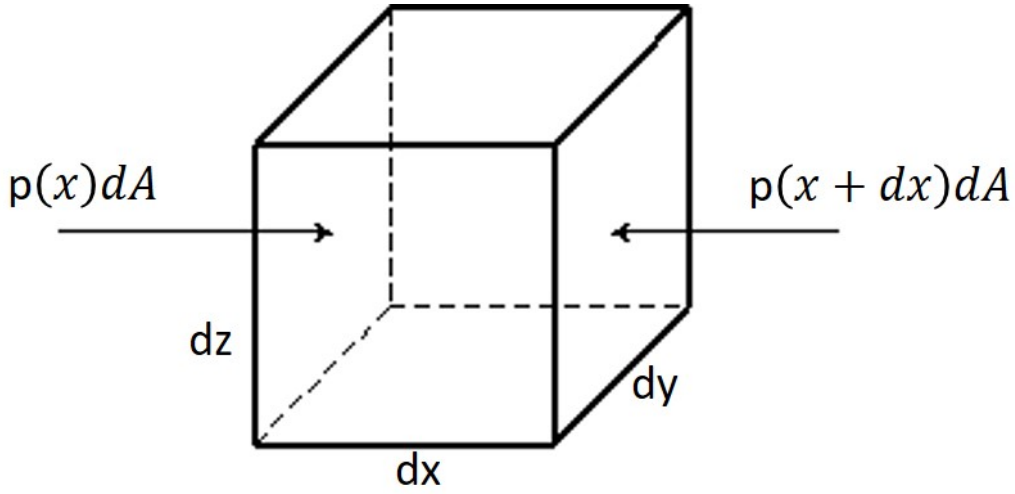

Figure 2.2: Force acting in the x direction on the faces of the control volume. The figure is adopted from [22].

Applying Equation 2.16 for all directions, the net force acting on the whole control volume will be:

$$d\vec{f} = -\nabla p_{total}\, dV \tag{2.17}$$

Combining Equation 2.13 knowing that $dm = \rho_{total}\, dV$ and Equation 2.17 we get:

$$\rho_{total}\, dV \frac{\partial \vec{u}}{\partial t} = -\nabla p_{total}\, dV \tag{2.18}$$

which can be further simplified, using equations 2.3 and 2.4, to the final form of the force equation:

$$\rho_0 \frac{\partial \vec{u}}{\partial t} = -\nabla p \tag{2.19}$$

The linear wave equation

To derive the linear wave equation, divergence of the right side of the force equation multiplied by -1 should be taken first. This will give us:

$$\nabla^2 p = \nabla \cdot \nabla p = -\rho_0 \nabla \cdot \frac{\partial \vec{u}}{\partial t} = \frac{\partial}{\partial t}\left(-\rho_0 \nabla \cdot \vec{u}\right) \tag{2.20}$$

Using the continuity equation (2.12), this could be rewritten as:

$$\frac{\partial}{\partial t}\left(-\rho_0 \nabla \cdot \vec{u}\right) = \frac{\partial}{\partial t}\frac{\partial \rho}{\partial t} = \frac{\partial^2 \rho}{\partial t^2} \tag{2.21}$$

DOI:10.15774/PPKE.ITK.2020.001

Combining this with the state equation (Equation 2.5) arranged to $\rho = p/\varepsilon$ and comparing it with the standard form of the wave equation, we see that ε should equal the square of the speed of sound c^2. Thus, we will get the final form of the homogenous LWE:

$$\nabla^2 p = \frac{1}{c^2}\frac{\partial^2 p}{\partial t^2} \tag{2.22}$$

Derivation of characteristic acoustic impedance

The acoustic impedance is defined as the ratio of pressure to particle velocity, in other words, it represents the resistance of the medium to acoustic wave propagation. It can be derived from the force equation (Equation 2.19). After rearrangement and integration in time we get:

$$\vec{u} = \int \frac{-\nabla p}{\rho_0} dt \tag{2.23}$$

In the special case of planar wave propagation, a simple constant specific to the material is obtained, termed the characteristic acoustic impedance, as it is characteristic of the material itself. Without loss of generality, let us suppose the wave propagates in the +x direction, so it can be written as $p = A\, f(x - ct)$, where $f(.)$ is an arbitrary function describing the shape of the wave. Knowing that the resting state density of the medium ρ_0 is independent of space and time we can get:

$$\begin{aligned} \vec{u} &= -\frac{1}{\rho_0}\int \frac{\partial A f\,(x-ct)}{\partial x} dt = -\frac{1}{\rho_0}\int A f'\,(x-ct)\, dt \\ &= -\frac{1}{\rho_0}\cdot\frac{1}{-c} A f\,(x-ct) = \frac{p}{\rho_0 c} \end{aligned} \tag{2.24}$$

So, acoustic impedance Z could be defined as:

$$Z = \frac{p}{\vec{u}} = \rho_0 c \tag{2.25}$$

where c is the longitudinal propagation speed of sound in the medium.

2.3 Derivation of scattering from the LWE

As mentioned in 1.1.5, the following derivation is based on [23].

Scattering is a phenomenon caused by small inhomogeneities of the medium. In a physical sense it arises from variations in the compressibility κ and density ρ

DOI:10.15774/PPKE.ITK.2020.001

of the medium. Defining the incident field as the field that would arise without such medium variations, the total pressure field $p(r,t)$ (to be precise, this total pressure field does not include the equilibrium pressure, so it is different from p_{total} in Equation 2.3) can be modelled as the sum of the incident $p_i(r,t)$ and scattered $p_s(r,t)$ pressure fields:

$$p(r,t) = p_i(r,t), +p_s(r,t) \tag{2.26}$$

In other words, scattering creates virtual sources of the pressure field. To include this into our model, governing equations of acoustics should be expanded as follows. Equation 2.3 remains the same, however, to take into account the variations in density Equation 2.4 will be:

$$\rho_{total} = \rho_0 + \Delta\rho + \rho = \rho_\upsilon + \rho \tag{2.27}$$

and considering the variations of compressibility we get:

$$\kappa_\upsilon = \kappa_0 + \Delta\kappa \tag{2.28}$$

Thus, the state equation (Equation 2.5) could be modified as:

$$p = \frac{1}{\kappa_\upsilon \rho_\upsilon}\rho \tag{2.29}$$

In the continuity equation the density will change in space, thus it should be rewritten as:

$$-\nabla \cdot \rho_\upsilon \vec{u} = \frac{\partial \rho}{\partial t} \tag{2.30}$$

Similarly, the force equation will be:

$$\rho_\upsilon \frac{\partial \vec{u}}{\partial t} = -\nabla p \tag{2.31}$$

Thus, the scattering LWE could be written as:

$$\nabla \cdot \left(\frac{1}{\rho_\upsilon}\nabla p\right) - \kappa_\upsilon \frac{\partial^2 p}{\partial t^2} = 0 \tag{2.32}$$

Using the above described relationships, the equation could be reformed to express separately the incident and scattered pressure field:

$$\nabla^2 p - \frac{1}{c_0^2}\frac{\partial^2 p}{\partial t^2} = -\nabla \cdot \left(\frac{\Delta\rho}{\rho_0}\nabla p\right) + \frac{\Delta\kappa}{\kappa_0}\frac{1}{c_0^2}\frac{\partial^2 p}{\partial t^2} \tag{2.33}$$

DOI:10.15774/PPKE.ITK.2020.001

2.4 Modelling of image formation

Image formation in ultrasound is mainly affected by the underlying scattering structure of the imaged medium. Scatterers introduce the well-known grainy noise in the US images, which usually considered as a kind of random noise that degrades image quality; hide parts of the underlying tissue structure in diagnostic imaging, thus adding a subjective judgement of the radiologist to the examination outcome.

Nevertheless, it was found that the speckle artefact on an image is fully deterministic. This means that it is caused by the interference of the waves scattered back from the same sub-wavelength particles. Extending the Fraunhofer approximation – introduced originally in optics – ultrasound image formation could be approximated by a linear system. The Fraunhofer approximation states that the far-field complex amplitude pattern created by a complex aperture amplitude function could be approximated by the Fourier transform of that function. [60, 61]

Thus, a radiofrequency ultrasound image y could be decomposed to a scatterer map or scattering function x (also known as the tissue reflectivity function [62]) – which includes the Cartesian space coordinates of every scatterer involved in the image – and a point spread function (PSF or h) [60], which is the transfer function of the exact imager:

$$y = h * x \,(+n) \tag{2.34}$$

where $*$ is the 2D convolution operator and n represents additive random noise (e.g. electrical noise) in the system.

Figure 2.3 illustrates a typical PSF with two types of windowing and the modelling of image formation compared to a real ultrasound image.

DOI:10.15774/PPKE.ITK.2020.001

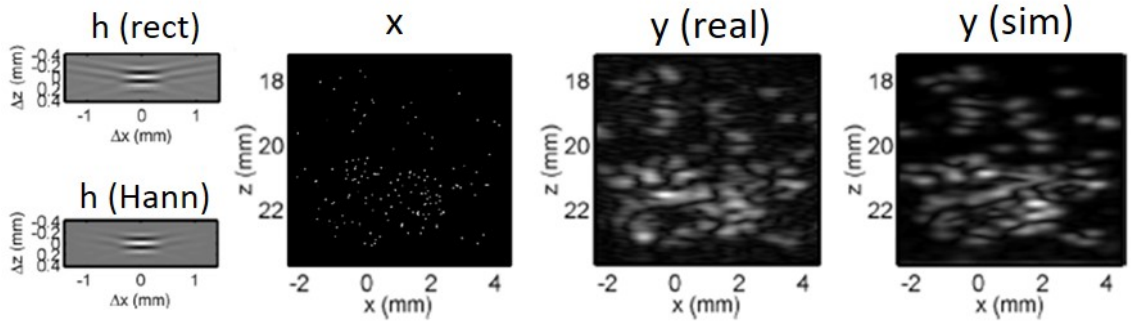

Figure 2.3: Example for the modelling of image formation. On the left side of the image, two simulated PSFs are shown plotted using a 2D rectangular and a Hanning window. To the right there is a typical image of a scattering function can be seen. On the right side a real B-mode image and a simulated B-mode image are shown. The simulated image is generated by using Equation 2.34. Figure is adopted from [63]

2.5 Acoustic material characterization

2.5.1 Speed of sound measurement

A variety of speed of sound estimation methods exist, in the literature the two main groups are usually called absolute and relative methods [1]. In absolute methods time of flight (TOF) of the wave is measured without the knowledge of speed of sound of a reference medium. Using absolute methods there are pulsed and continuous wave techniques published.

In relative methods the measurements rely on the knowledge of speed of sound of the reference medium. As a reference medium there are several existing material, which are homogeneous and for which the acoustic properties could be well characterized. These are usually liquids, for example water or saline are usually used for tissue characterization.

In this work relative methods are used for speed of sound measurements, using distilled water as a reference medium. There are two branches of relative methods. One is the reflection-based method, where the same transducer is used in transmit/receive mode and the backscattered signal is investigated to calculate speed of

DOI:10.15774/PPKE.ITK.2020.001

sound values. The other method is the through-transmission measurement, where two transducers are aligned opposite to each other. One of them is the transmitter transducer, which can emit e.g. burst signals at predefined frequencies, the other one is the receiver transducer. Here two measurements are performed in sequence. First, TOF – and knowing this, speed of sound – in the reference medium is measured, knowing the distance between the surfaces of the transmitter and receiver transducers. Second, TOF in the same path – but with the investigated medium inserted as well – is measured.

Reflection-based measurements

A method, which is similar to that presented below, was used by Dunn et al. [64], however, to fit the measurements to our hardware we used the time-domain instead of frequency domain, although a correct mathematical relationship is lacking in that case. Therefore Equation 2.35 was derived.

For the better understanding, Figure 2.4 illustrates a reflection-based measurement setup. Using Equation 2.35 the unknown speed of sound (v_s) of a sample could be calculated based on the measured TOF values (t_{sum} – between the transducer and the bottom of the bath, without sample; t_{ref} – between the transducer and the top of the sample trough reference medium , t_s – between the two adverse surfaces of the sample) and using the knowledge of the speed of sound in the reference material (v_{ref}):

$$v_s = v_{ref}\left(\frac{t_{sum} - t_{ref}}{2 * t_s}\right) \tag{2.35}$$

The time parameters of each measurement can be easily read from an oscilloscope, however, there are several ways to evaluate speed of sound, depending on where the signal is picked from. In this work the starting point of the wave-package was chosen, however, this is an overestimate of values [1]. Nevertheless, every method has its own source of error. In the equations above v_{ref} is the speed of sound of the fluid in the bath, which was water in our measurements. This value is temperature dependent and well known in literature [65, 66].

DOI:10.15774/PPKE.ITK.2020.001

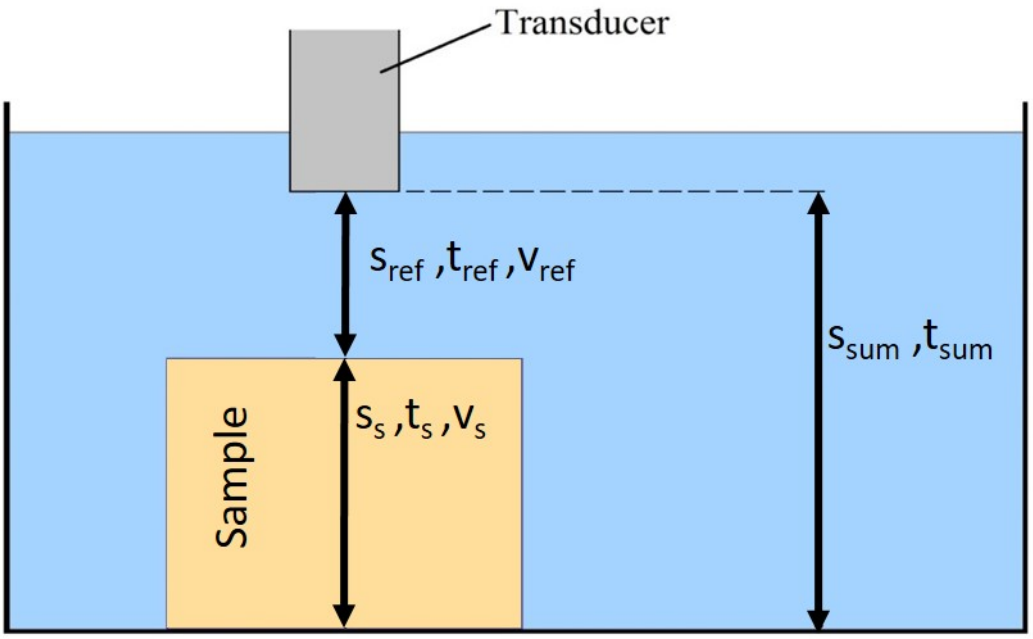

Figure 2.4: The schematic setup for reflection-based speed of sound measurements. The figure shows the corresponding time, distance and speed of sound values for the reference medium and the sample. s_s is the height of the sample, s_{sum} is the distance between transducer head and the bottom of the bath. Latter is given by the speed of sound of the water and the TOF without the sample. It is important that during the measurements s_{sum} should be permanent.

Through-transmission measurements

A disadvantage here compared to reflection-based measurements is that the path length of the wave must be known. Measurement error of path length will equal to the measurement error in speed of sound – expressed in percentages (i.e. 0.1 mm error at 10 mm length will introduce 15.4 m/s error in speed of sound when measuring on average soft tissue). This could be fended off using longer path lengths, where the measurement error of path length could be considered negligible. When measuring on thinner samples, a reference medium should be used.

An adequate alignment of the two transducers is crucial. Simple holders for this purpose could be manufactured e.g. using PMMA plates, which have the exact sized holes laser cut into them.

DOI:10.15774/PPKE.ITK.2020.001

The speed of sound of the sample (c) can be estimated by the following equation:

$$c = \frac{z}{\left(\frac{z}{c_0} + \Delta t\right)} \tag{2.36}$$

Where z is the thickness of the sample, c_0 is the speed of sound of the reference medium and δt is the time difference between incoming waves in the reference measurement and incoming waves in the present measurement.

2.5.2 Acoustic attenuation

Attenuation or total loss of sound energy in a medium is a complex phenomenon, which basically consist of absorption, scattering, reflection and refraction. In reality perfectly plane waves do not exist, so diffraction gives an additional source of loss. [1]

Acoustic attenuation – similarly to speed of sound – can be measured using relative and absolute methods.

For absolute measurement of attenuation coefficient, both a reflection-based and a through transmission setup is practical. Avoiding material boundaries (i.e. between the sample and a reference medium) reflection and refraction based errors are minimized. However, it is important to note that in this case the measurement usually takes place in the near filed, thus power of the beam varies with the propagation distance. For this reason, acoustic field of the used transducer(s) should be tested or simulated and the results of the measurements should be interpreted including these corrections.

In a reflection-based setup, when assessing acoustic attenuation coefficient measured at a particular frequency ($\alpha(@f_c)$) it is practical to have two blocks of samples having different thicknesses (a thinner and a thicker one: d_{thick} and d_{thin}; practically equal to 5 mm and 10 mm to get the results in dB/cm) and a reflector surface, which is perpendicular to the beam propagation. Dividing the maximal amplitudes of received signals A_{thin} and A_{thick} and comparing them to the acoustic path lengths on a logarithmic scale will give the attenuation coefficient at the used center frequency f_c.

$$\alpha = 20log\left(\frac{A_{thin}}{A_{thick}} \cdot \frac{2}{d_{thick} - d_{thin}}\right) \qquad [dB/cm\ @f_c\ MHz] \tag{2.37}$$

DOI:10.15774/PPKE.ITK.2020.001

A trough-transmission setup works similarly; only the numerator of the last fraction of Equation 2.37 should be changed to 1, as the beam propagates only forward in the sample.

To get a more precise knowledge on the attenuation coefficient, a through transmission setup using a relative method should be used. Here, it is practical to choose the reference medium having negligible attenuation compared to the measured medium and similar acoustic impedance as the sample itself to avoid reflections from boundaries. Using such setup, ideally, samples of any shape could be measured. However, in real world, there will be always some difference in acoustic impedance, so for a precise measurement a special care should be also taken to use samples having smooth surfaces parallel to each other and to adjust the sample surfaces perpendicular to the direction of beam propagation, thus minimizing loss caused by reflection and refraction. Also, if possible, the measurement should take place in the far-field of the transducers.

2.5.3 Kramers-Kronig relationship

As mentioned in 1.1.5, the following overview is based on [23, 24]. In ultrasound, experiments have shown that the attenuation of a medium is proportional to the nth power of the frequency. For classical viscous media, like water, $n \cong 2$ and for tissues a typical value is $1 \leq n < 2$. [24] The speed of sound in a medium is also changing with the frequency. This phenomenon is called speed of sound dispersion and interestingly does not arise for $n = 0$ or 2. [23]

As mentioned previously, absorption and scattering both contribute to attenuation, and thus to the above-mentioned behaviours. However, the contribution of scattering to the attenuation is not well documented and is significantly lower than absorption. Thus, effects of scattering is usually ignored and simply dispersion equations can be used. [24]

This relationship of the speed of sound dispersion and frequency dependent attenuation are described by the Kramers-Kronig relation. The Kramers-Kronig relation was obtained first for electromagnetic waves [23], however, as it is the result of linearity and causality, the Kramers-Kronig relation could be used for any other

DOI:10.15774/PPKE.ITK.2020.001

waves, i. e. acoustic waves. A generalized form of the equation could be written as [24]:

$$\frac{1}{c(\omega)} = \frac{1}{c_0} + \alpha_0 \, tan\left(\frac{\pi n}{2}\right)\left(|\omega|^{n-1} - |\omega_0|^{n-1}\right) \tag{2.38}$$

As was shown previously, speed of sound and attenuation coefficient could be measured. Absorption – using a nearly ideal setup – could be considered to be identical to the measured acoustic attenuation values neglecting the effects scattering. Using Kramers-Kronig relation, experimental results could be validated, if both speed of sound dispersion and attenuation of a material were measured.

DOI:10.15774/PPKE.ITK.2020.001

Chapter 3

Acoustic Characterization of Porcine Myocardium

3.1 Introduction

In this chapter my work of characterization of speed of sound and attenuation coefficient in porcine myocardium is shown. The results were verified using Kramers-Kronig relation, which as mentioned previously (Chapter 1) connects the speed of sound dispersion with a measured reference attenuation coefficient and its exponent.

The current study is useful for two reasons: the acquired values could help us in tissue thermometry and also essential for building realistic muscle phantoms.

3.1.1 Relevance of the current study

Cardiac ablation is a common medical intervention to treat cardiac arrhythmias such as ventricular tachycardia [67]. It is typically performed using RF ablation [68], although the use of HIFU is also being investigated [69]. Thermal ablation relies on irreversible denaturation of the myocardial tissue, which at 43 °C takes around 170 minutes [70]. Since every degree above 43 °C halves the expected time to reach the same thermal dose [71], this value translates to keeping the tissue at 50 °C for 80 seconds. In cardiac ablation, the tissue of interest is generally raised to above 50 °C for at least 35-45 seconds [67, 72].

DOI:10.15774/PPKE.ITK.2020.001

The elevated temperatures caused by cardiac ablation can also damage nearby healthy tissue, such as other areas of the heart, the pulmonary veins, or the esophagus [67]. Therefore, a temperature monitoring method would help safer delivery of cardiac ablation. Since ultrasound phase velocity and attenuation change with temperature [51], one possibility is to use ultrasound imaging as a monitoring method. A brief discussion of such acoustic changes follows.

In general, non-fatty tissues exhibit an increase in the speed of sound with temperature, and a decrease in attenuation with temperature, for temperatures of up to about $40 - 50\,^{\circ}\mathrm{C}$, while fatty tissues show an opposite trend [51]. The difficulty of defining an exact temperature at which the trends reverse stems from the fact that above $43\,^{\circ}\mathrm{C}$, the delivered thermal dose also plays an important part in the measured acoustic properties [73, 74]. For instance, Damianou et al. [75] showed that in canine soft tissue, attenuation increased with time for a thermal dose of around 100-1000 minutes at $43\,^{\circ}\mathrm{C}$.

Although the acoustic properties of the myocardium have received the attention of many researchers, studies on the changes of such properties with temperature are sparse. Several papers have found that phase velocity [76–78] and attenuation slope with frequency [79, 80] increase as the propagation direction with respect to the fibers changes from perpendicular to parallel. In particular, typical values of speed of sound at room temperature are 1557 m/s and 1565 m/s (a 0.5% increase) [78], while attenuation increases from $0.5 - 0.6$ dB/cm/MHz to $1.2 - 2.2$ dB/cm/MHz (a 2-4-fold increase).

Regarding changes of myocardial tissue attenuation with temperature, O'Donnell et al. [81] reported that attenuation decreases by -0.06 dB/cm/ $^{\circ}\mathrm{C}$ at 10 MHz in the $20 - 37\,^{\circ}\mathrm{C}$ temperature range. Concerning changes in speed of sound, Seo et al. [82] showed that the flattening and eventual reversal of the apparent speed of sound was a good indicator of tissue necrosis, pointing out that above 50°C, thermal expansion of the tissue becomes a significant contributor to the apparent speed of sound. This was later confirmed by Baki et al. [83], who showed that thermal expansion is the main contributor to apparent speed of sound changes for temperatures above $55\,^{\circ}\mathrm{C}$. These works provide a methodology for detecting thermal damage from thermal

DOI:10.15774/PPKE.ITK.2020.001

dose and thus ensure treatment efficacy. However, a method is needed to monitor lower temperatures ($< 50\,^{\circ}\mathrm{C}$) before thermal dose effects take place, to ensure timely treatment modification before surrounding myocardial tissue is damaged. Baki et al. [83] state that there is a speed of sound increase of around 45 m/s from $20\,^{\circ}\mathrm{C}$ to $55\,^{\circ}\mathrm{C}$ at 20 MHz, corresponding to a temperature coefficient of speed of sound of 1.29 m/s/ $^{\circ}\mathrm{C}$; however, no uncertainty on the measurement is reported.

Motivated by the need for monitoring moderate ($< 50\,^{\circ}\mathrm{C}$) temperatures during cardiac ablation using ultrasound, the aim of the current work is to calculate the temperature coefficients of speed of sound and attenuation coefficient and compare them with the existing values provided by O'Donnell et al. [81] and Baki et al. [83], respectively. The temperature range ($25 - 45\,^{\circ}\mathrm{C}$) is chosen such that variation of the acoustic parameters with temperature is expected to be linear [51, 84] and irreversible protein denaturation from thermal dose effects are avoided. The wide frequency range used (2.5-13.0 MHz) aims to ensure relevance of the obtained results for a wide set of diagnostic ultrasound transducers. In addition, since frequency-dependent attenuation is related to phase velocity dispersion via the Kramers-Kronig relation [24], comparison of the expected dispersion from attenuation with the actually measured phase velocity dispersion may provide validation of the measurements.

3.2 Experimental methods

3.2.1 Experimental setup

A through-transmission setup was used with two unfocused 10 MHz single element transducers (12.7 mm diameter, 4.5-15.5 MHz -6 dB bandwidth; Model V311-SU, Panametrics NDT, Waltham, MA) separated by a distance of 100 mm (Figure 3.1a). The measurements were carried out in a lab heating bath (Model SW-20C, Julabo GmbH, Seelbach, Germany). The bath contained a heater element controlled by a thermometer with $1\,^{\circ}\mathrm{C}$ resolution.

The overall experimental measuring equipment consisted of off the shelf signal generation and data acquisition hardware from National Instruments (NI, Austin, TX). Transmission and reception were controlled by a standard laptop connected

DOI:10.15774/PPKE.ITK.2020.001

to an NI PXIe-1073 platform through an NI ExpressCard-8360. The transmission signal was generated by an NI PXI-5412 arbitrary waveform generator (AWG) module inside the PXI platform, which was then amplified (Research Model 150A100B, Amplifier Research, Souderton, PA) and sent to one of the transducers. The receiving transducer was directly connected to an NI PXI-5122 digitizer module inside the PXI platform, sampling at 100 MHz. All hardware was software controlled by NI LabVIEW. The software was programmed to perform a discrete frequency sweep from 0.5 to 20.0 MHz in 0.25 MHz steps, with the number of periods in each burst waveform equal to 12f, where f is the frequency in MHz [85].

The choice of propagation medium to place in the bath was not simple. Some researchers have opted to use distilled water as its speed of sound is well characterized [65, 86], noting however, that swelling occurs as the sample reaches osmotic equilibrium [77, 79]. Some researchers have used a saline bath [75] to ensure isotonic conditions, which works fine for attenuation measurements, but complicates speed of sound calculations. Still others filled the bath with distilled water, but kept the tissue sealed inside a plastic bag with saline solution [51]. Even in the latter approach, however, the complex variation of the saline solution properties in the bag may need to be accounted for [74]. Moreover, reflections from the bag may also complicate the calculation of attenuation coefficients. The current work used a bath of distilled water that was free to mix with the tissue sample.

3.2.2 Preliminary testing of the experimental setup

As the final experiments on the freshly excised porcine left ventricles (LV) needed to be carried out in a very limited time window, preliminary validation of the measurement setup was essential. Firstly, the size of the hole in the tissue holder (for details of the setup, see figure 3.1) and its spatial position between the transducers were determined. For both, a semi-empirical workflow was employed.

The size of the hole should be as small as possible, to ensure planar surface of the inserted tissue. Two candidates for the diameter of the circular cut in the holder were 20 and 25 mm based on simulations of the acoustic beam width of the transducers. Investigation of the position of the tissue holder was also partially

DOI:10.15774/PPKE.ITK.2020.001

based on acoustic field simulations of the transducer. There positions of the tissue holders were compared: I. next to the transmitter transducer, II. midway between the transmitter and receiver transducers, III. next to the receiver transducer.

The final diameter of the hole and the position of the holder was chosen based on measurements performed in distilled water. Comparing measurement results with the reference of deionized water [87], the larger, 25 mm diameter hole was found to be adequate positioning the holder midway between the transmitter and receiver transducers.

Using this holder position, several other measurements were carried out using 6 left atrial (LA) and 3 right ventricular (RV) samples, measured at 16 sites in total, to test the time dependent behaviour of the samples. Namely, how their acoustic properties change over time due to water infiltration, stiffening or degradation. Before the experiments these samples were stored in PBS solution (sometimes in fridge – depending on the time of the experiments) to decelerate degradation. During the experiments the samples were stored in a water bath filled with distilled water at room temperature for 55 minutes. Measurements were started from the fifth minute and repeated at every 10 minutes.

The mass of the samples were also checked with a simple lab balance with an accuracy of 0.1 g before and after the experiments. The mass of the samples were always measured after inserting them into the tissue holder, thus ensuring identical conditions for each measurement pair. Before the mass measurements after the experiments, the water was removed from the surface of holder and the sample with paper towels.

As storing time was less controlled before the experiments and as the type of specimens were less controlled (e.g. information of the sacrificed animals such as their age and weight were lacking), the measured phase velocity values between the samples showed high variance (values obtained between 1550-1630 m/s with a mean around 1560 m/s), while the obtained attenuation values seemed to be unreliable (results showed $3.5 - 4$ dB/cm/MHz). However, the maximum recorded deviation between the first and last time point for a single sample site was less than 10m/s. The most probable reason for the speed of sound deviation between the samples could

DOI:10.15774/PPKE.ITK.2020.001

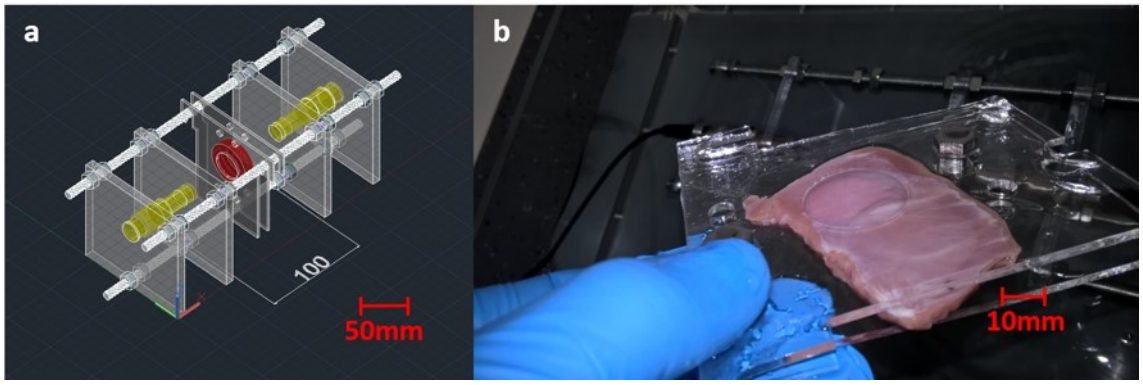

Figure 3.1: AutoCAD model (left) of the measurement setup and photo of the sample and its holder (right). The transducers (indicated with yellow color on the left) are fixed with 8 mm thick PMMA plates. The distance between the transducer surfaces could be changed and properly aligned by adjusting the position of the plates on the threaded rods. The tissue holder for the sample (indicated with red color on the left) can also be positioned and fixed using the threaded rods. The diameter of the window in the tissue holder was 25 mm.

be the difference in the fat content of the tissues used. Also, as the thicknesses of LA and RV are usually smaller (~ 3 and $5-7$ mm) than that of the LV (usually >9 mm), thus the rate of deviation of thickness measurements were also higher, especially for the LA.

The mass measurements of each samples showed ~ 0.2 g variance. The obtained speed of sound values were linear over time. As a conclusion, water infiltration to the tissue considered to be negligible.

3.2.3 Sample preparation

As part of a separate, ethically approved experiment, 3-4-month-old pigs were sacrificed. Altogether, N=5 left ventricle samples were obtained for the purposes of the current experiment, with an original thickness of 10 mm for 4 samples and 9 mm for 1 sample.

Since fixation of tissue creates protein cross-links and thus changes in acoustic properties [88], the tissue samples used in this experiment were freshly excised and

DOI:10.15774/PPKE.ITK.2020.001

were stored in phosphate-buffered saline (PBS). As recommended by O'Donnell et al. [81], measurements were carried out within 4 hours after excision.

Prior to placement in the heating bath, the tissue samples were inserted between two 2 mm thick poly-methyl methacrylate (PMMA) plates with circular windows of 25 mm diameter (see Figure 3.1b). The windows ensured that additional reflections in the measurement pathway were avoided. As can be seen in Figure 3.1, the holder setup allowed the two transducers and the sample to be all coaxially aligned, with the myocardial fibers perpendicular to the direction of the ultrasonic wave propagation.

3.2.4 Experimental protocol

The starting temperature of the water bath for each sample was 25 °C, which was then increased in discrete steps to 35, 40, and 45 °C. Ice was used to cool down the water (together with the inserted sample) to 35 °C, and then to 25 °C. The ice was added in small doses in order to avoid cryoablation of the tissue. The change in temperature of the water was not more than 2 °C per minute.

After reaching the desired temperature, an additional 10 minutes were considered to allow the entirety of the tissue sample to reach the surrounding temperature. In addition to the aforementioned bath thermometer, a kitchen thermometer with 0.1 °C resolution was used to continuously monitor the temperature near the sample. The maximum deviation from the desired temperature during a measurement was 0.2 °C. Immediately before each tissue measurement - at all discrete temperatures for all individual samples - a reference measurement without the tissue was performed.

During the experiments, the thickness of the samples was measured using a Vernier caliper with 0.05 mm resolution. Compression of the tissue during measurement was avoided as much as possible. The largest thickness difference recorded over a sample was 1.0 mm, limiting the measurement precision to ± 0.5 mm.

DOI:10.15774/PPKE.ITK.2020.001

3.3 Estimation of the acoustic parameters

The received signals were stored and used to calculate the phase velocity and attenuation characteristics within the aforementioned NI LabVIEW environment [85]. Additional post-processing and visualization was carried out in MATLAB (Mathworks, Natick, MA). Whereas the original range of measurement was 0.5-20.0 MHz, we decided to exclude those measurements that had a signal to noise ratio (SNR) below 20 dB. Therefore, only the results between 2.5 and 13.0 MHz will be considered in the final evaluation.

In the following, we briefly recall the equations used to calculate the two relevant acoustic parameters.

3.3.1 Phase velocity estimation

The phase velocity *c(f,T)* at frequency f of the sample, measured at a fixed temperature T, was estimated as:

$$c(f,T) = \frac{z}{\frac{z}{c_0(T)} + \Delta t(f,T)} \tag{3.1}$$

where z is the thickness of the sample [m], c_0 *(T)* is the speed of sound [m/s] of the reference medium (assuming negligible dispersion, see later) and Δ *t(f,T)* is the time difference [s] between incoming waves in the reference measurement and incoming waves in the actual measurement with a sample in place, at the central transmission frequency *f*.

3.3.2 Attenuation estimation

The attenuation coefficient α *(f,T)* at frequency f of the sample, expressed in [Np m^{-1}] and measured at a temperature T, was estimated as:

$$\alpha(f,T) = -\frac{1}{z} ln\left(\frac{p(f,T)}{p_{ref} f(f,T)}\right) \tag{3.2}$$

where z is again the thickness of the sample [m]. Here, *p(f,T)* is the received pressure amplitude through the sample, whereas p_{ref} *(f,T)* is the pressure amplitude received through the reference medium. Both are measured at frequency f and

DOI:10.15774/PPKE.ITK.2020.001

temperature T. To investigate the frequency-dependence of the attenuation, the attenuation coefficient was modelled using a power law:

$$\alpha(f) = \alpha_0 \left(\frac{f}{f_0}\right)^n \tag{3.3}$$

where f_0 is the reference frequency (10 MHz) and n is dimensionless. Doing so, α_0 is the attenuation coefficient at the reference frequency f_0 and has units of [Np m^{-1}]. Using log-log regression, the exponential coefficient n can be easily estimated for each measurement.

3.3.3 Linear regression of phase velocity and attenuation with temperature

The temperature variation of the phase velocity and the attenuation coefficient, measured at the reference frequency f_0=10 MHz, were plotted and analyzed using a linear regression fitting routine. Linear regression was applied to increasing temperatures (from 25 °C to 45 °C) and decreasing temperatures (45 °C to 25 °C) for each sample separately, and the mean and standard deviation of the regression coefficients over all tissue samples were calculated (i.e. a statistical two-step procedure). The unit of attenuation coefficient was converted to [dB cm]$^{-1}$ to provide easier comparison with literature.

3.3.4 Comparison of expected phase velocity dispersion with observed values

According to the Kramers-Kronig relation [24] (for detailed discussion, see Chapter 2, Subsection 2.5.3), the phase velocity $c(f)$ depends on the attenuation power law coefficient n, introduced in Equation (3.3), in the following manner:

$$c(f) = [c_{f0}^{-1} - \alpha_0 (2\pi f_0)^{-1} \tan(0.5\pi n)(1 - (f/f_0)^{n-1})]^{-1} \tag{3.4}$$

where c_{f0} is the reference speed of sound [m/s] and α_0 the reference attenuation [Np m^{-1}], both measured at the reference frequency f_0. Using an estimated or experimentally derived value of n, this equation thus allows us to predict *c(f)* from a

DOI:10.15774/PPKE.ITK.2020.001

single speed of sound measurement c_{f0} and reference attenuation α_0, and to compare it with the measured variation of *c(f)* across the entire frequency range. It should be noted that for n=2 (as in the case of the distilled water used as the reference medium), Equation (3.4) predicts no dispersion.

3.4 Results and discussion

3.4.1 Measurement results

Figure 3.2 shows the mean phase velocity dispersion profiles over all samples at different temperatures. For all tissue samples and temperature values, a linear regression was applied to the change of phase velocity with temperature, which yielded an average gradient of 0.27 ± 0.04 m/s/MHz. As a general observation, we notice that the absolute phase velocity increases with an increase of the temperature (red curves at $25-35-40-45\,^{\circ}$C), and then decreases again following a temperature reduction (red curve at $45\,^{\circ}$C, together with the blue curves at $35-25\,^{\circ}$C). Looking at the data in more detail, the results show different phase velocities during heating and cooling for the 25 and $35\,^{\circ}$C data point. The reason behind this difference will be discussed later.

Figure 3.3 shows the mean and standard deviation of the phase velocity, calculated over all samples at the reference frequency of 10 MHz, and plotted as function of the increasing and decreasing temperatures range. The plot is representative for data at all other frequencies. It can be observed that the results for the decreasing temperature branch ($45-35-25\,^{\circ}$C) appear more consistent, which is also confirmed by the lower standard deviation on the linear regression coefficients calculated for the individual samples (Table 3.1).

Performing the same analysis for the dispersion of the attenuation coefficient over all samples at different temperatures, Figure 3.4 clearly shows that the attenuation coefficient increases non-linearly with frequency. For each temperature, the mean attenuation coefficient was calculated over all samples, from which the attenuation

DOI:10.15774/PPKE.ITK.2020.001

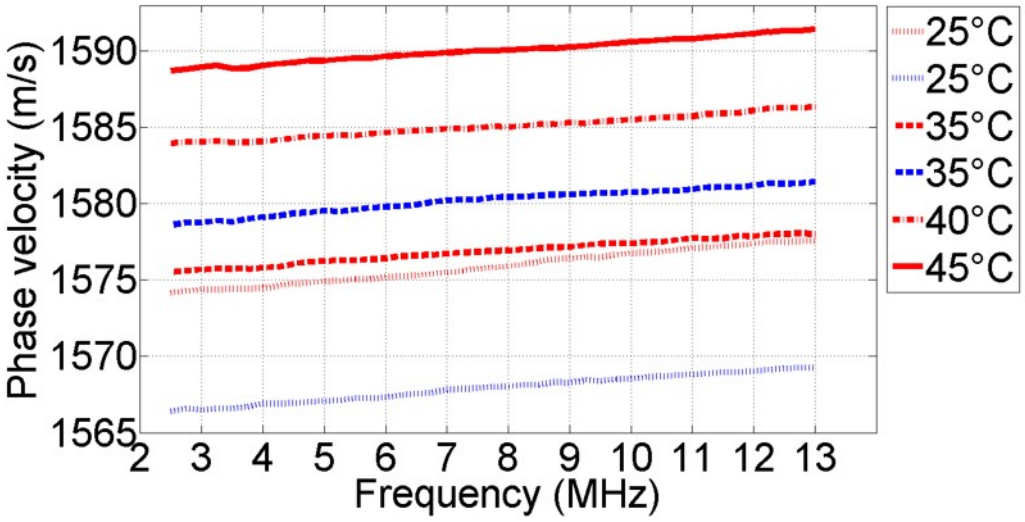

Figure 3.2: Averaged phase velocity dispersion curves calculated over all samples in the frequency range of 2.5-13.0 MHz. Red and blue colors indicate the data acquired during heating and cooling of the surrounding medium, respectively. Dispersion of the phase velocity is clearly visible and can be described by a linear function of frequency with a slope of 0.2705 ± 0.042 m/s/MHz.

	Increasing temperature	Decreasing temperature
Speed of sound slope (m/s/ °C)	0.70 ± 0.23	1.10 ± 0.04
Speed of sound intercept (m/s at 0 °C)	1557.2 ± 11.4	1541.4 ± 3.5

Table 3.1: Fitted linear regression parameters (slope and intercept) of the phase velocity versus temperature over the range of 25 to 45 °C*, calculated at 10MHz. The fitting parameters are expressed as 'mean ± standard deviation', calculated for N=5 samples.*

power law coefficient n was calculated. The value was found to be 1.434 ± 0.025; there was no observable trend with temperature.

Similarly to Figure 3.3, Figure 3.5 shows the change in attenuation coefficient with temperature at the reference frequency of 10 MHz. Although, there is a con-

DOI:10.15774/PPKE.ITK.2020.001

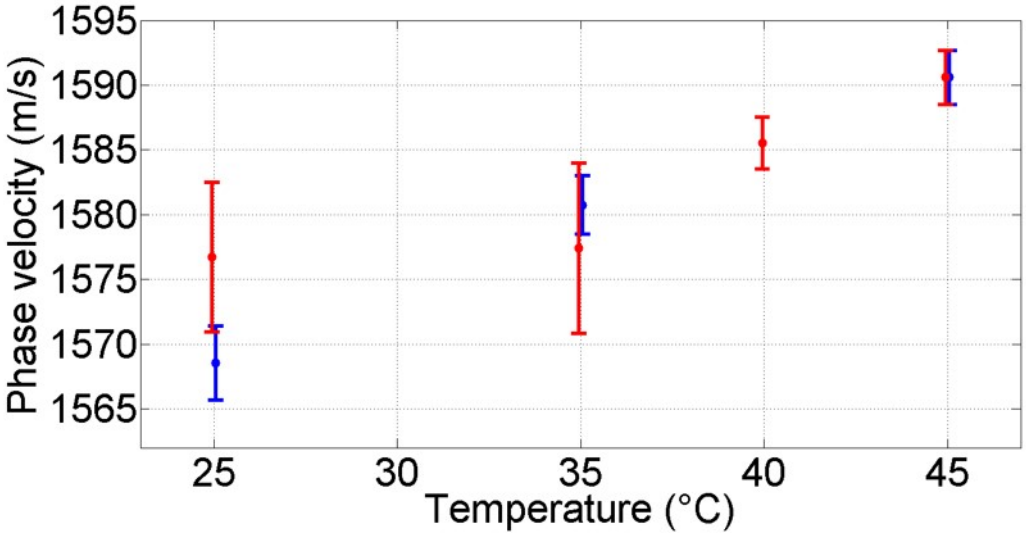

Figure 3.3: Averaged phase velocity values and standard deviations calculated over all samples at 10 MHz excitation frequency as the function of temperature. Red and blue colors indicate the results obtained during heating and cooling of the surrounding medium, respectively. Averaged data points are shown as dots, while error bars indicate the standard deviation. The slightly higher standard deviation observed at the first temperature points (at 25 °C *and* 35 °C*) during heating is due to the swelling of tissue in the beginning of the experiment, which is also the reason for the quite similar phase velocity values at those two temperature readings. Please note that the* 45 °C *data are indicated both in red and blue colors as they are a common endpoint to the heating and cooling regressions.*

siderable variation in the measured attenuation, there is a clear downward trend in the attenuation coefficient with temperature, as also quantified and summarized in Table 3.2, with a change of attenuation with temperature of -0.11 dB/cm/ °C.

3.4.2 Variation of speed of sound with temperature

The speed of sound (measured at a reference frequency of 10 MHz) of porcine left ventricular myocardium, obtained at room temperature was 1568.5 $\pm$.2.85.m/s. This is consistent with previously reported data for human myocardium, namely 1570-1571 m/s [87, 89]. The values reported by Verdonk et al. [76] are considerably

DOI:10.15774/PPKE.ITK.2020.001

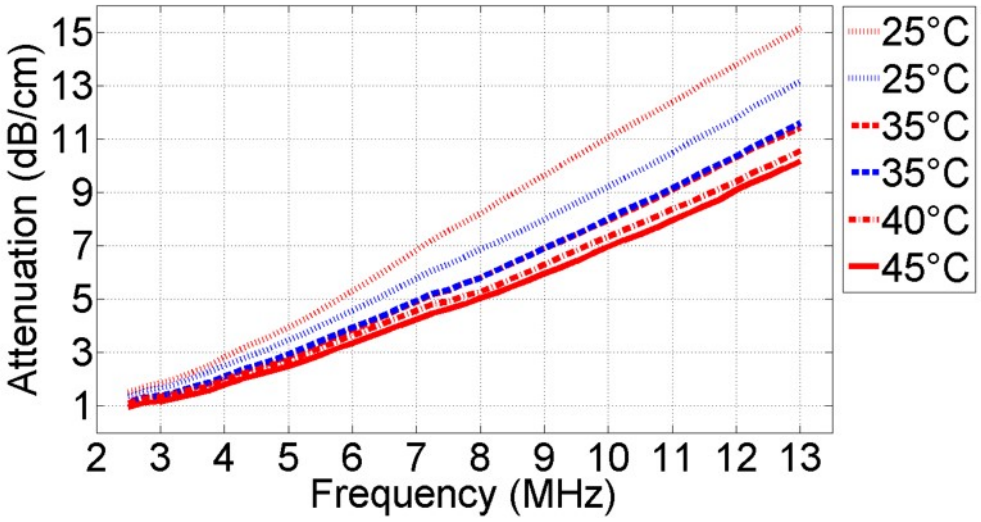

Figure 3.4: Averaged attenuation coefficients calculated over all samples over the frequency range of 2.5-13.0 MHz. Red and blue colors indicate the data acquired during heating and cooling of the surrounding medium, respectively. Discrepancies in the 25 °C *data are probably caused by the swelling of the samples. The attenuation power law coefficient* n *is* 1.4336 ± 0.025.

	Increasing temperature	Decreasing temperature
Attenuation slope (dB/cm/ °C)	-0.21 ± 0.05	-0.11 ± 0.04
Attenuation intercept (dB/cm at 0 °C)	15.90 ± 3.26	11.98 ± 2.81

Table 3.2: Fitted linear regression parameters (slope and intercept) of the attenuation coefficient versus temperature over the range of 25 to 45 °C*, calculated at 10MHz. The fitting parameters are expressed as 'mean ± standard deviation', calculated for N=5 samples.*

lower (around 1530 and 1550 m/s for measurements perpendicular and parallel to the myofibers, respectively), presumably due to the myofibers being measured as opposed to bulk myocardium, as in the current case. The slope of the temperature-dependence of the speed of sound (also measured at a reference frequency of 10 MHz) obtained in the current work for decreasing temperatures ($1.103 m/s/$ °C) is slightly

DOI:10.15774/PPKE.ITK.2020.001

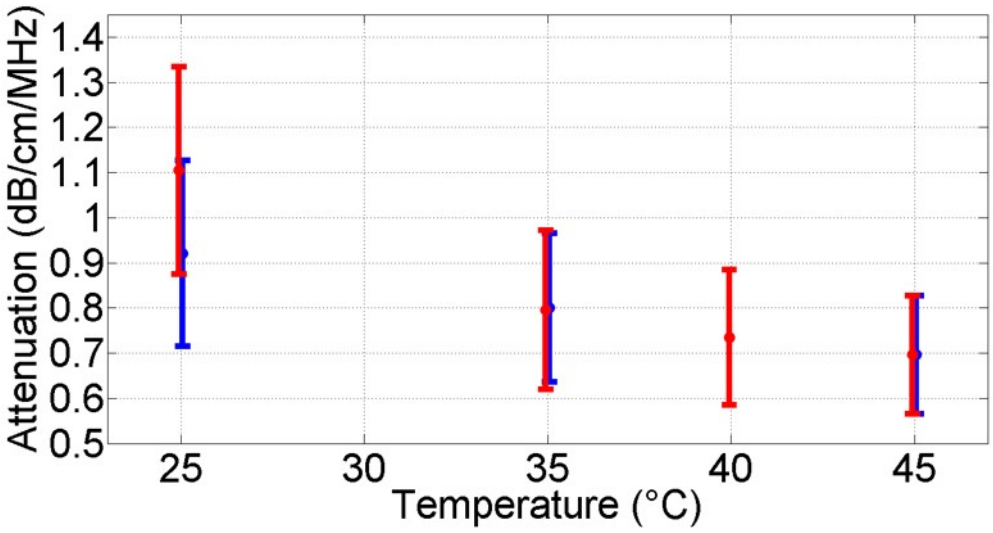

Figure 3.5: Averaged attenuation coefficient values and standard deviations calculated over all samples at 10 MHz excitation frequency as the function of temperature. Red and blue colors indicate the results obtained during heating and cooling of the surrounding medium, respectively. A good agreement can be seen in the range of 35 - 45 °C. Discrepancies at 25 °C are due to initial swelling of the tissue. Standard deviation of the data at all temperatures is similar but relatively high, which is presumably due to the microstructure of the tissue, e.g. the position and size of the muscle fibers and their tissue composition. Please note that similarly to Figure 3.3, the 45 °C data are indicated both in red and blue colors as they are a common endpoint to the heating and cooling regressions.

lower than the results reported by Baki et al. [83] for porcine myocardium (around $1.29 m/s/\,^{\circ}\mathrm{C}$). The differences in the obtained speed of sound and slope can be attributed to a variety of causes, including different compositions (e.g. fat content), different reference frequency, use of distilled water versus saline solution, cell death, age of the animals, route to thermal equilibration, etc. Overall, the speed of sound measurements for decreasing temperatures seem to be consistent with previously obtained data.

DOI:10.15774/PPKE.ITK.2020.001

3.4.3 Variation of attenuation with temperature

The slope of the attenuation coefficient versus temperature was investigated by O'Donnell et al. [81] in canine myocardium for a range of temperatures between 20 and 37 °C. In this temperature range, a decrease of 1 dB/cm was observed at 10 MHz, which corresponds to a slope of around −0.06 dB/cm/ °C. Bamber and Hill [51] noted that the attenuation versus temperature slope for bovine liver varied substantially (strongly influenced by the fat content), but was mostly found to be in the range of −0.03 to −0.10 dB/cm/ °C at 7 MHz. The results of our study show a slope of −0.11 dB/cm/ °C at 10 MHz for decreasing temperatures. Although a difference in results from porcine myocardium versus bovine liver can be readily expected, the current results suggest that the attenuation characteristic of porcine myocardium are almost double than that observed by O'Donnell et al. for canine myocardium [81].

It should be mentioned that the acoustic impedance of typical human tissues (1.58-1.70 MRayl, reported in [90]) and in particular human myocardial tissue (1.64 MRayl [89]) differs somewhat from distilled water (1.5 MRayl [91]). However, based on the law of reflection and transmission, the loss of amplitude at the two water-tissue interfaces is not expected to exceed 0.79 dB, making the loss negligible compared to tissue attenuation, especially at higher frequencies.

The possibility of phase cancellation yielding overestimates of the attenuation coefficient should also be mentioned, especially given the anisotropic nature of myocardial tissue [79,92]. However, given the observed smooth variation of attenuation with frequency, the effect of phase cancellation is not expected to be significant [1,93].

3.4.4 Kramers-Kronig relationship between speed of sound and attenuation

Based on the above derived mean value of n and the reference speed of sound and attenuation coefficient at 10 MHz, the Kramers-Kronig relation (Equation 3.4) was applied to predict the dispersion profile over the frequency range between 2.5 and 13.0 MHz and to compare it with the measured phase velocity over this range. Fig-

DOI:10.15774/PPKE.ITK.2020.001

ure 3.6 displays the comparison for the data taken on a tissue sample at 35 °C as the temperature was rising. The speed of sound dispersion, predicted by Equation (3.3) from the attenuation data, shows a good agreement with the measured dispersion. A similarly good agreement was also found for data at other temperatures, and for other samples. This agreement provides an important validation of the accuracy of the attenuation and phase velocity measurements reported.

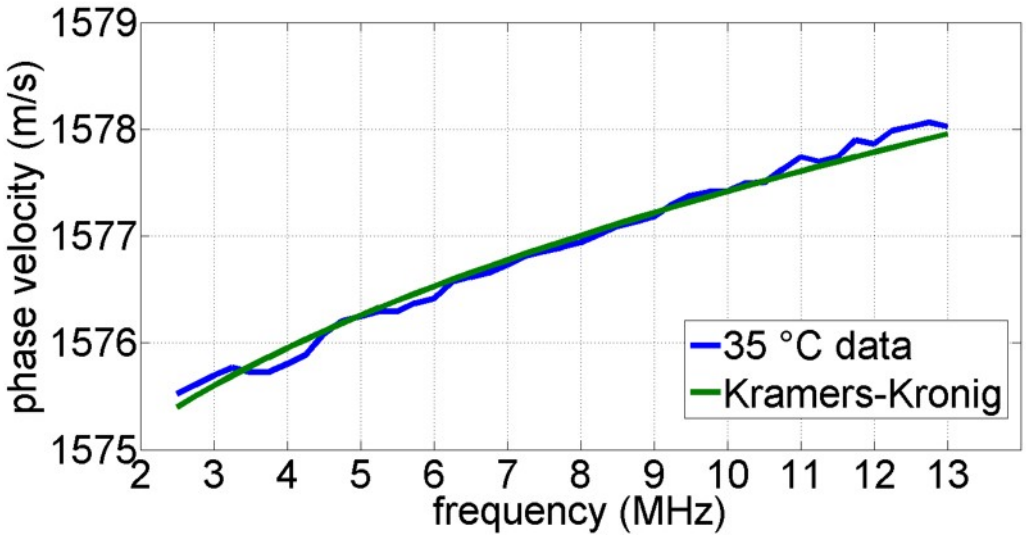

Figure 3.6: Comparison between the phase velocity dispersion data collected at 35°C (blue line) and the theoretically predicted phase velocity dispersion using the Kramers-Kronig relation Equation (3.4). The reference sound speed and averaged attenuation coefficient at 10 MHz, as well as n=1.434, were used as input for Equation 3.4

.

3.4.5 Tissue handling

As mentioned in Section 3.2 (Experimental Methods), the measurement precision of the tissue thickness was ±0.5 mm. This may induce a maximum error of 5 m/s in the phase velocity measurements (owing to the 9-10 mm sample thicknesses and maximum 100 m/s difference in phase velocity between the sample and reference medium). In comparison, the standard deviation of speed of sound was 11.4 m/s for

DOI:10.15774/PPKE.ITK.2020.001

increasing, and merely 3.5 m/s for decreasing temperatures, respectively (Table 3.1). Figure 3.3 shows that the first two data points for increasing temperatures have higher variance and seem to be outliers to the rest of the points. The observed higher variance is postulated to be related to osmotic equilibration, since the decrease in measurement variance coincided with the tissue reaching a final swelling thickness. However, the authors are uncertain as to the exact mechanism of measurement inaccuracy, since thickness measurements were performed directly before acoustic measurements.

In the case of attenuation measurements, Figure 3.5 suggests that the first data point for increasing temperatures has a higher than expected attenuation compared to the other data points. This is also hypothesized to be due to osmotic effects, since swelling will increase the relative proportion of water in the tissue, which has a negligible attenuation compared to tissue. However, the variance of the data points themselves is approximately similar throughout (around 20% relative standard deviation), suggesting that another source of measurement variance dominates. One possible explanation is that variations in tissue composition (such as fat [94], collagen [93]) have been shown to have a strong effect on attenuation. In contrast, speed of sound variations are expected to be less than 5% in the heart due to variations in collagen and fat content [95]. Another possibility, the influence of fiber orientation.

As discussed in Section 3.1 (Introduction), the speed of sound and attenuation increase by 0.5% and 100-300%, respectively, when the direction of ultrasound propagation with respect to the fibers changes from perpendicular to parallel. In the present study, we opted to investigate the temperature dependency of both the attenuation coefficient and the speed of sound when the wave propagation direction was perpendicular to the myocardial fibers. This type of setup was chosen as it is representative for the clinical scenario in which an ablation catheter is used at the inner side of the cardiac wall, which is orthogonal to the endocardial border and is pointing towards the epicardium. Thus, if an ultrasound transducer is installed on such a catheter for temperature monitoring purposes, this would indeed be the most relevant direction. In addition, for insonation at angles perpendicular to the heart surface, the circumference of the heart yields a minimal distortion to fiber alignment,

DOI:10.15774/PPKE.ITK.2020.001

as exemplified by negligible changes in attenuation for angular variations of $\pm 10^{\circ}$ from perpendicular [80]. Therefore, it is thought that other sources of variation, such as differences in tissue composition are more probable sources of measurement variation.

To investigate the inaccuracies in detail, a possible solution may be to perform further measurements on the tissue after the original measurements finished.

To establish the effect of fiber orientation, the samples could be inserted in a setup using a rotable tissue holder and be measured. Similar setup was used by Verdonk et. al. [76, 79]. Nevertheless, the samples would exceed the 4 hour limit recommended by O'Donnell et al. [81], the rate of the effect caused by fiber orientation may be measured in a more exact manner.

The rate of water absorption could be characterized by density measurements before and after the experiment, however, difficulties could be also emerged while determining the tissue volume. With MR such measurement would be also possible, however, feasibility could be a main issue as the cost rate may be too high compared to the benefits.

For the investigation of tissue composition a microtome based histology solution could be useful. Using histology, fiber orientation as well as tissue composition could determined on the measurement sites.

3.5 Conclusions

In conclusion, we have investigated the temperature dependence of the speed of sound and the attenuation characteristic of porcine myocardial tissue over a wide, clinically applicable frequency range ($2.5 - 13.0$ MHz) as well as over a relevant temperature range ($25 - 45$ °C). The obtained results are consistent with data reported elsewhere, which however, only considered either limited frequency or temperature ranges. In addition, experimental measurements of the phase velocity dispersion were obtained over a wide range of frequencies and the results were validated through comparison with theoretically predicted values using the Kramers-Kroning relation, revealing a good agreement.

DOI:10.15774/PPKE.ITK.2020.001

The current results also show, what are the optimal acoustic properties for creating a realistic muscle-tissue phantom. The obtained values are higher than the average 1540 m/s used for conventional B-mode imaging. Thus, when modelling or reconstructing myocardial tissue images the values obtained in the current work should be used to avoid image distortions. Moreover, considering standard B-mode images including myocardial tissue, distortions emerging from the difference in propagation speed could be also compensated for.

As a supplement of the current study, clarifying the source of inaccuracies arising from fiber orientation, water absorption, swelling and tissue composition would be useful. For this, multiple further measurements should be performed.

DOI:10.15774/PPKE.ITK.2020.001

Chapter 4

Customizable, Cost-Effective Ultrasound Phantoms

4.1 Introduction

Ultrasound phantoms are widely used for quality assurance (QA) testing of ultrasound imaging systems and validation of novel imaging methods, as well as the simulation of tissue images for training purposes [18]. As discussed in Chapter 1, wide variety of well-established phantom materials and manufacture methods exist, both commercial and in-house [14, 96]. One common need arising in phantom manufacture is the introduction of spatial structure into the phantom at various geometric scales. For instance, different concentrations of micrometer-scale scatterers are often added to achieve regions with different levels of hyperechogenicity, and the regions themselves can be separated from each other using molds [14, 18]. As another example, wires or string can be used to simulate vasculature [97]. Filaments are also used to measure axial and transverse image resolution as part of QA testing [17, 98–100], although their ability to relate these measures to clinical performance appears to be limited [101]. This is in part due to the difficulty of relating resolution in three dimensions to overall resolution and a frequency dependence of backscatter that differs from that of tissue [102]. As a result, alternative methods based on other inclusions, such as anechoic cylinders [103, 104], anechoic spheres [16] or step targets [102], are being explored.

DOI:10.15774/PPKE.ITK.2020.001

All of the phantoms described above are made using conventional manufacturing techniques that are unable to place a large number of discrete scatterers at exactly specified locations. Such an ability could enhance the realism of conventional tissue-mimicking phantoms, as well as allow experimental validation of imaging techniques such as adaptive beamforming that seek to separate otherwise unresolved scatterers [105–107].

One possible solution to the bespoke placement of discrete scatterers comes from recent advances in 3D printing technology. Three-dimensional printed materials are typically harder than soft tissue, finding wide use as a bone-mimicking material [39–42]. Although a plethora of 3D printing materials are available, it is difficult to find one whose acoustic properties (in particular, speed of sound and attenuation) closely match those of soft tissue. Recently, several groups have used a material (FullCure 705, Stratasys, Eden Prairie, MN, USA) with unpolymerizable components as the propagation medium to manufacture ultrasound phantoms using photopolymer jetting technology [30, 108]. Photopolymer jetting printers, however, are relatively expensive, typically costing more than $25,000. Moreover, the reported speed of sound of FullCure705, 1617 m/s, is somewhat above the typical value of 1540 m/s assumed for soft tissue. The current chapter describes the use of a FDM 3D printer and a custom-made 3D printer using a DLP projector to create inexpensive filament target phantoms. The space between the filaments can be filled with any material used in conventional phantom manufacture technology to produce the desired speed of sound and attenuation. In our phantoms, water was used as the propagation medium. The aim of the current work was to compare the feasibility of using FDM and DLP to create filament target phantoms, with a particular focus on the acoustic characteristics of the printing materials, the dimensions of the filaments and their appearance on ultrasound images.

The structure of the remainder of the chapter is as follows. First, the use of FDM and DLP printing is described under Section ‘Printing Methods’. Next, the methods of characterizing the printed materials, the filament structures and the resulting filament phantoms thereby obtained are described. This is followed by a presentation and discussion of the characterization results. Last, the results are

DOI:10.15774/PPKE.ITK.2020.001

summarized, with a view toward identifying future refinements and possibilities.

4.2 Printing methods

4.2.1 Fused deposition modelling printing

In FDM printing, a filament is passed through a heated nozzle that extrudes the molten material (Figure 4.1). The nozzle is moved in the x–y direction to form a layer of the material. When a layer is completed, the stage is moved in the z direction to allow the next layer to be constructed.

In the current work, a companion software (FlashPrint) of the commercially available FDM printer (Flashforge Dreamer, Flashforge, Jinhua, China) receives the commonly used STL file format for printing. Two commonly available 1.75-mm-diameter round filaments were used: acrylonitrile butadiene styrene (ABS) and polylactic acid (PLA), both manufactured by MakerBot (New York, NY, USA). A thermoplastic polyurethane (TPU) material was also tested (Filaflex, Recreus, Elda, Spain), although, as will be seen in the next section, the testing went only as far as the material characterization phase. Paper glue on masking tape was used to fix the first layer of printing on the platform. Printing parameters, according to manufacturer recommendations, are summarized in Table 4.1. Objects were designed in AutoCAD 2015 (Autodesk, San Rafael, CA, USA) and then exported to STL format for printing. When generating filaments at required positions, MATLAB was used to generate the required set of native commands for AutoCAD, which were then run to add the filaments to the model.

4.2.2 Digital light processing printing

The concept of DLP printing is that commonly used DLP projectors emit enough UV radiation to cure UV-sensitive photopolymers. In the current work, each successive layer of the printed object was formed by using a projector (MX717, BenQ, Taipei, Taiwan) as the output device of a laptop to shine images of successive layers

DOI:10.15774/PPKE.ITK.2020.001

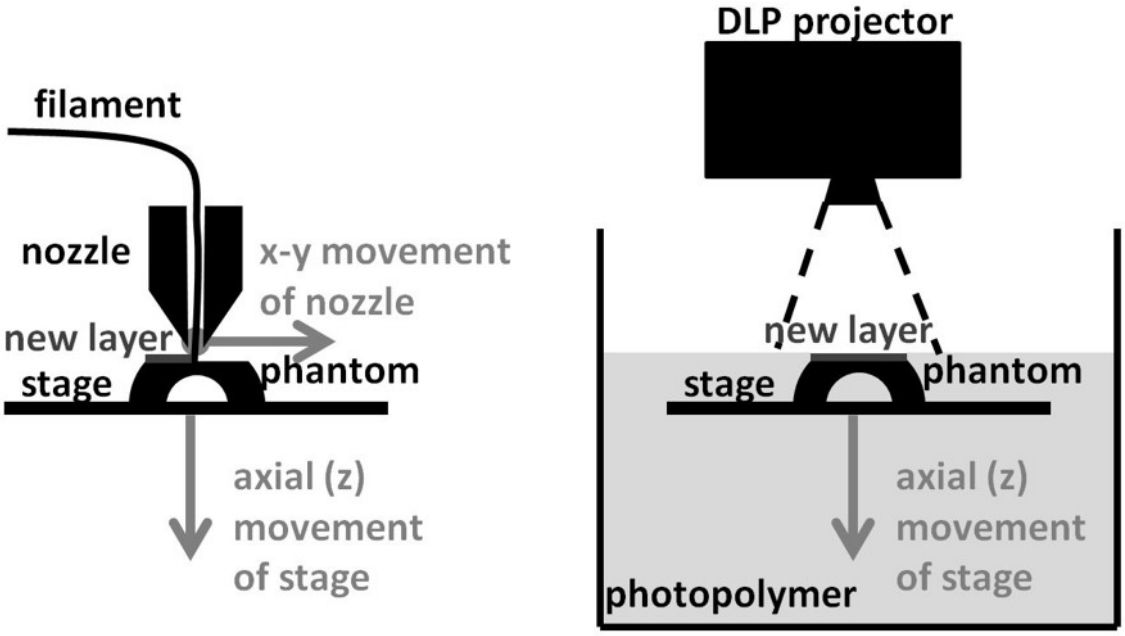

Figure 4.1: Schematics of the printing techniques employed in the current work. Left: FDM printing. By moving a heated nozzle in the x–y plane (one of the directions is out of the plane), a layer of molten material can be deposited. Movement of the stage in the z direction achieves 3D printing. Right: DLP printing. Similarly to the FDM technique, the phantom is manufactured layer by layer using a mechanical stage. However, in this case, each layer is formed simultaneously by projection of an image onto the surface of a liquid photopolymer. The photopolymer cures on exposure to the UV radiation emitted by the DLP projector.

.

onto the surface of a liquid photopolymer (Standard Blend, Fun To Do, Alkmaar, Netherlands), as in Figure 4.1. The liquid photopolymer was held in a PMMA container; inside of which was placed a horizontal stage made of a stainless steel sheet. This stage was moved vertically from one projection to another in 0.1 mm steps to build up a 3D volume (see Table 4.2), with the first projection taking place when the stage had been moved 0.1 mm below the surface of the liquid photopolymer. Stage motion was achieved using a MTS50/M-Z8 precision electric motor with ATP 32-bit control software, both from Thorlabs (Newton, NJ, USA). The images sent to the projector were generated with MATLAB.

DOI:10.15774/PPKE.ITK.2020.001

Printing parameter	General setting		
Layer step size (mm)	0.1		
Filament diameter (mm)	1.75		
Nozzle diameter (mm)	0.4		
Minimum object diameter (mm)	0.35		
Infill	100%		
Support material	None		
Printing Parameter	ABS setting	PLA setting	TPU setting
Nozzle temperature (°C)	220	205	230
Platform temperature (°C)	100	50	40
Print speed (mm/s)	50	80	80
Travel speed (mm/s)	60	120	120

Table 4.1: Fused deposition modelling printing parameters. (ABS = acrylonitrile butadiene styrene; PLA = polylactic acid; TPU = thermoplastic polyurethane.)

4.3 Characterization methods

The proposed methods for creating filament target phantoms were tested in three ways. First, solid blocks were printed to measure the acoustic properties of the printed materials. Second, a grid of filaments was printed to measure printing accuracy. Lastly, a filament target phantom was printed and evaluated qualitatively and quantitatively using ultrasound imaging. A detailed description follows.

Printing parameter	DLP setting
Layer step size (mm)	0.1
Projection distance (mm)	200
Exposure duration (s)	25

Table 4.2: DLP printing parameters

DOI:10.15774/PPKE.ITK.2020.001

4.3.1 Material characterization

Solid blocks of designed thicknesses 5 and 10 mm were printed. In the case of FDM printing, the block area was 30 x 60 mm, whereas for DLP printing, it was 50 x 50 mm. The actual thickness of the blocks was measured using a caliper with 0.05 mm accuracy. For each block material and block thickness, two samples were printed. For acoustic characterization, pairs of transducers with three different central frequencies were alternately used: 2.25 MHz (aperture D = 12.7 mm, Model C540), 5 MHz (D = 6.35 mm, Model C543), 10 MHz (D = 6.35 mm, Model C544), all from Olympus (Tokyo, Japan). The transducers were connected to a pulser-receiver (5073 PR, Olympus, Tokyo, Japan) set to through-transmission mode, which in turn was connected to a 0 to 200 MHz bandwidth digital oscilloscope (DS1204B, Rigol Technologies, Beijing, China).

To ensure better accuracy, the speed of sound was measured on the thicker 10 mm samples, using a through-transmission technique (Chapter 2) that measured the time elapsed between the transmission of the initial pulse and reception of the pulse on the receiver transducer [109]. Acoustic coupling gel (AquaUltra Clear, Budapest, Hungary) was placed on the surface of the transducers, which were then placed on opposite sides of the block sample and pressed firmly against it. For each sample, three measurements were made at different locations.

The significance of various changes in measurement conditions was tested, all comparing N = 3 samples using the independent two-sample two-tailed t-test, using p = 0.05 as a threshold for significance. The effect of submerging the samples in water for 72 h was tested with the 2.25 MHz transducer. Thereafter the samples were stored in water at 25.0 °C. The temperature was measured using a kitchen thermometer with an accuracy of 0.1 °C. Material isotropy in the FDM-printed samples was investigated by measuring the speed sound in the x–y and z directions (see Figure 4.1 for the orientations). To check whether the photopolymer had fully cured during DLP printing, the speed of sound was also measured after subjecting the sample to 15 min of UV radiation inside a household nail dryer with a 9 W UV lamp.

Attenuation of the samples was estimated using the same through-transmission

DOI:10.15774/PPKE.ITK.2020.001

setup as with the speed of sound. In this case, however, the drop in received signal amplitude from the 5-mm-thick block to the respective 10-mm-thick block was measured. This procedure eliminated errors arising from surface reflections [109]. As with speed of sound, three measurements were made for each sample.

Mass density was measured by placing 1-cm-wide cuts of the 5-mm-thick blocks into a beaker containing a measured mass of 85% aqueous glycerine solution, the density of which had been previously measured as 1224 kg m^{-3}. The beaker was placed on a scale with 0.1 g resolution, and de-ionized water (with a density of 998 kg m^{-3}) was slowly poured and mixed with the glycerine solution. By recording the scale reading at which each block stopped floating, density could be estimated. Finally, the characteristic acoustic impedance of the samples was obtained by multiplying density by the measured speed of sound [91].

4.3.2 Characterization of printing accuracy

To characterize the accuracy of the printing processes involved, two rows of 13 filaments, each with a square cross section of 0.5 mm, were designed and printed (Figure 4.2). Preliminary tests indicated this was the size FDM printing could handle consistently. The length of filaments was chosen as 10 mm, the longest length to still avoid sagging.

There were two aspects to printing accuracy. First, printing errors (number of incorrectly placed filaments, maximum position error of incorrectly placed filaments and number of erroneous extra threads) were quantified for all filaments using a caliper with 0.05 mm accuracy. These errors were expected to be less relevant for DLP printing, where each layer was formed simultaneously. Next, to provide an indication of the printing resolution, the caliper was used to measure the height and width of the four filaments at the edges (where there was easy access to measurements).

DOI:10.15774/PPKE.ITK.2020.001

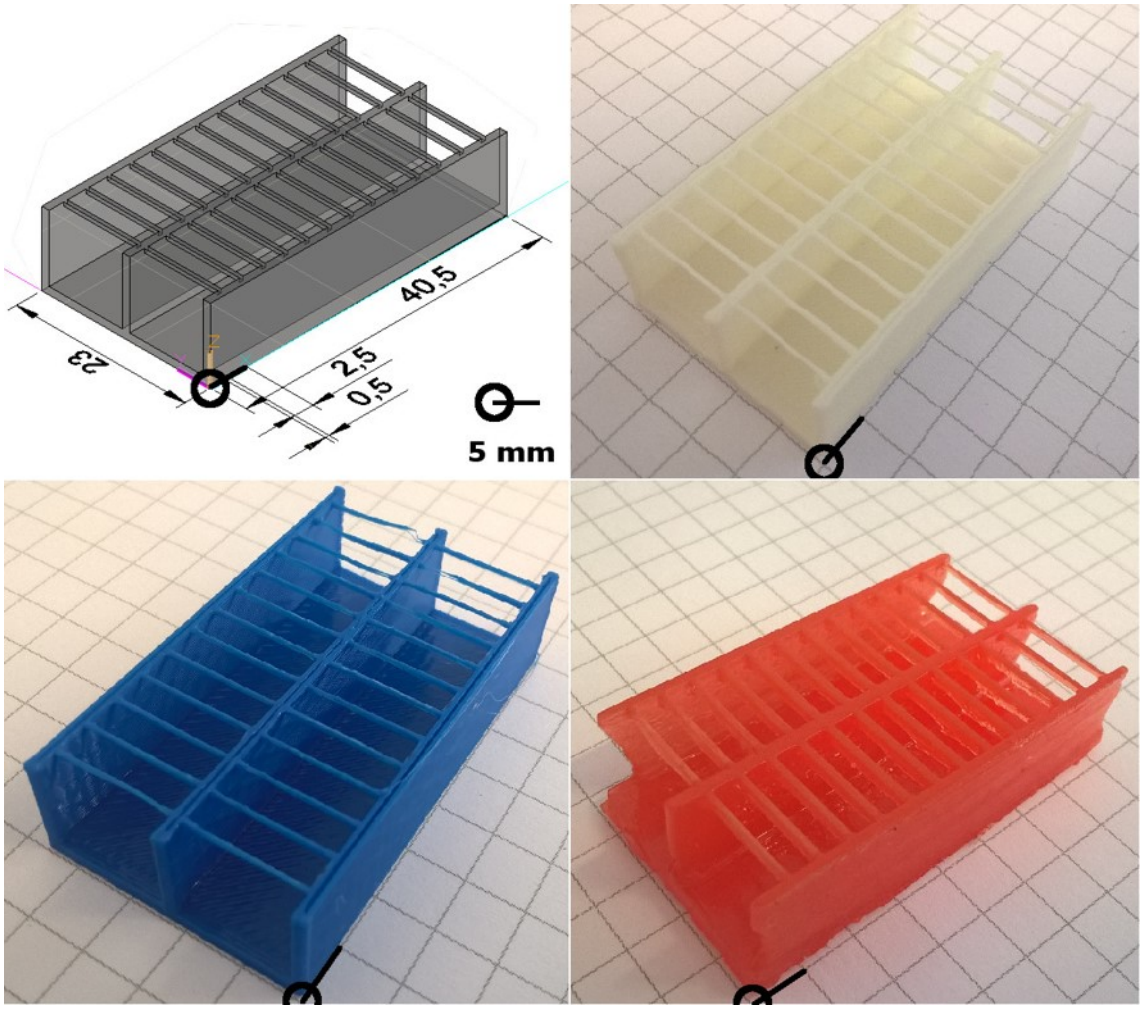

Figure 4.2: Grid of filaments for testing of printing accuracy. Two rows of 13 filaments were designed, each with a 0.5 mm length square cross section. The black circles represent the origin of the printing coordinates, with the line coming out of each circle depicting a 5 mm length along the x direction (see Figure 4.1). Printing was carried out from the base upward. Top left: Technical drawing of the grid design. Top right: thermoplastic acrylonitrile butadiene styrene phantom. Bottom left: Polylactic acid phantom. Bottom right: Photopolymer phantom.

.

DOI:10.15774/PPKE.ITK.2020.001

4.3.3 US characterization of filament target phantoms

To test how a custom pattern of filament targets would appear on an ultrasound imager, a pattern bearing the letters “ITK” (the native-language acronym of our faculty) was designed and printed (Figure 4.3). The resulting phantoms were placed in a PMMA holder filled with de-ionized water and then imaged using a 47.0 mm aperture, 3.3-10.0 MHz linear array (ULA-OP LA522E, Esaote, Genoa, Italy) connected to an ULA-OP Research US system (MSD Lab, University of Florence, Florence, Italy) that had access to the envelope data before dynamic range compression. Transmit focus depth was set to 20 mm, the same as the elevational focus of the transducer acoustic lens.

The axial and lateral full width at half-maximum (FWHM) values of the three filaments nearest to being at 20 mm depth (one from each letter) were measured. As multiple reflections were expected in the axial direction, a so-called full width at last half-maximum (FWLHM) measure was also defined and calculated in the axial direction. Here, within a 3 mm range around the maximum point, the furthest half-maximum points before and after the maximum were located to calculate the measure.

As means of comparison, the above values of FWHM and FWLHM were also calculated for a 100-mm-diameter nylon monofilament of a commercial phantom (Model 040 GSE, CIRS, Norfolk, VA, USA), as well as for a simulated image of a point scatterer. Both scatterers were placed at 20 mm depth. For the simulations, carried out using the Field II MATLAB toolbox [110, 111], linear array parameters matching those of the real array were used.

DOI:10.15774/PPKE.ITK.2020.001

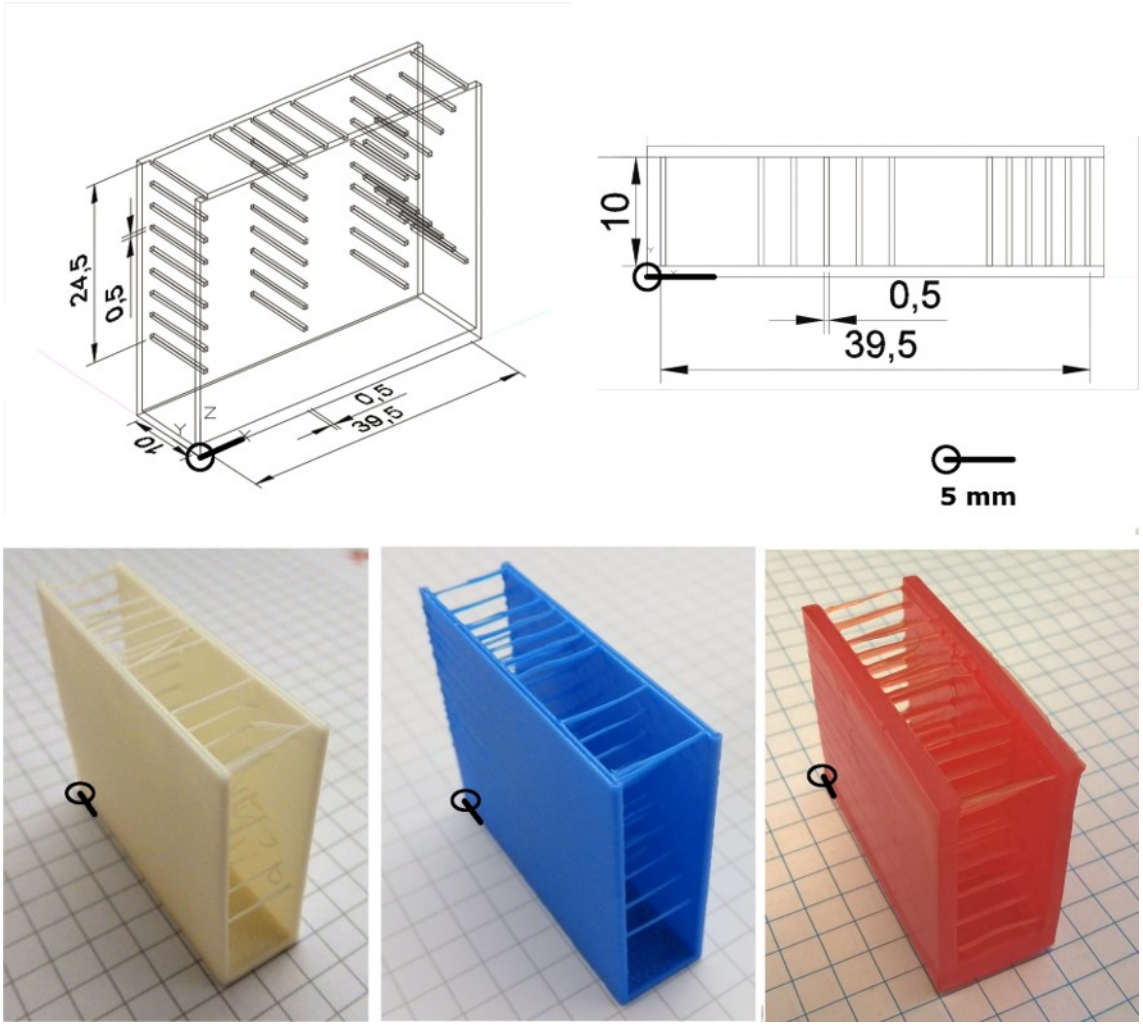

Figure 4.3: Filament target phantom bearing the letters "ITK." The black circles represent the origin of the printing coordinates, with the line coming out of each circle depicting a 5 mm length along the x direction (see Figure 4.1). Printing was carried out from the base upward. Top: Technical drawing of the filament target phantom. Bottom left: Acrylonitrile butadiene styrene (ABS) phantom. Bottom center: Polylactic acid (PLA) phantom. Bottom right: Photopolymer phantom. Note that contrary to the ABS and PLA phantoms, which were designed with 1 mm wall thickness, the digital light processing phantom was designed with 2 mm wall thickness for added structural robustness.

.

DOI:10.15774/PPKE.ITK.2020.001

4.4 Results and discussion

4.4.1 Material characterization

Thermoplastic polyurethane had been considered a promising material, because polyurethanes are already in use in ultrasound phantoms [14]. However, no signal above the noise floor was received in the through-transmission measurements. A significant amount of air seems to have been introduced into the material during the printing process; varying the nozzle temperature or the density of the printing did not help to avoid this phenomenon.

Table 4.3 lists the measured characteristics of the other three materials (ABS, PLA and photopolymer). The values are quoted for samples that had been placed in 25 °C de-ionized water for 72 h before the measurements, with measurements being conducted in the z direction (Figure 4.1) and no additional UV curing of the photopolymer. Leaving the blocks in water for 72 h did not have a significant effect on speed of sound at 2.25 MHz. Similarly, exposure of the photopolymer to an additional 15 min of UV radiation revealed no significant difference in speed of sound at 2.25 MHz. Significant differences were found, however, between the speed of sound measured in the z direction and that in the x–y direction, with the speed of sound at all three frequencies being on average 54.8 and 137.1 m/s higher in the x–y direction for ABS and PLA, respectively. The reason for this higher speed of sound is not clear. However, during imaging, the ultrasound wave travels primarily in the z direction, so these are the values quoted in Table 4.3.

Before discussing the other acoustic properties, the measured attenuation of the printing materials merits discussion. From the literature, the attenuation values of ABS and PLA are 2.2 and 0.59 dB/cm/MHz at 5 and 15 MHz, respectively [91, 112]. The former value corresponds well to the current measured value of 2.42 dB/cm/MHz at 5 MHz. However, for all three materials, the measured attenuation increases more slowly than linearly with frequency. Such frequency dependency is unusual for a material [113] and therefore raises the prospect of measurement errors. By use of the expression for diffraction correction found in Leveque et al.

DOI:10.15774/PPKE.ITK.2020.001

Material	ABS	PLA	Photopolymer
Mass density (kg m^{-3})	1032	1175	1107
Speed of sound (m/s)			
2.25 MHz	2078.2 ± 0.5	1924.5 ± 15.4	2136.9 ± 26.6
5 MHz	2117.8 ± 2.9	1990.3 ± 12.2	2193.2 ± 30.8
10 MHz	2156.3 ± 7.6	2008.0 ± 14.4	2217.8 ± 26.2
Characteristic acoustic impedance (MRayl)			
2.25 MHz	2.15	2.26	2.37
5 MHz	2.19	2.34	2.43
10 MHz	2.23	2.36	2.46
Attenuation/frequency ratio (dB/cm/MHz)			
2.25 MHz	4.30 ± 0.18	6.49 ± 0.35	2.56 ± 0.20
5 MHz	2.42 ± 0.06	2.35 ± 0.03	2.89 ± 0.14
10 MHz	1.39 ± 0.14	1.34 ± 0.04	1.26 ± 0.06

Table 4.3: Acoustic properties of the 3D printing materials investigated in the current work. ABS = acrylonitrile butadiene styrene; PLA = polylactic acid. Where multiple measurements were carried out, ± standard deviation values are provided (N = 3). Characteristic acoustic impedance was calculated from the product of density and speed of sound. For reference, typical values of mass density, speed of sound, acoustic impedance and attenuation/frequency ratio in tissue are 1050 kg m^{-3}, 1540 m/s, 1.62 MRayl and 0.3 - 1.1 dB/cm/MHz, respectively [15]

DOI:10.15774/PPKE.ITK.2020.001

[114], diffraction is expected to cause a less than 4% error in all of the attenuation measurements. Therefore, there is thought to be some other source of measurement error such as electrical noise or the inhomogeneous nature of block printing, especially in the case of FDM printing. In any case, provided that the partial volume of the propagation medium is sufficiently large, the attenuation of the phantom is expected to follow the attenuation of the propagation medium.

Because the proposed materials are used as scatterers with respect to the propagation medium (in the current work, de-ionized water), it is useful if their acoustic characteristics are close to those of the propagation medium (which itself should be close to tissue). This is to minimize artefacts from multiple reflections and phase aberration, arising from large changes in acoustic impedance and speed of sound, respectively. At the same time, the difference between the acoustic impedance of the scatterer and that of the surrounding medium should be large enough to generate a scattering signal that is above background scattering and the electric noise floor.

The acoustic impedance and speed of sound of the 3D printing materials were measured to be in the ranges 2.15-2.46 MRayl and 1909.1-2244.0 m/s, respectively (Table 4.3). For comparison, nylon, a commonly used filament scatterer in phantoms [14, 115], has corresponding values of 2.90 - 3.15 MRayl and 2600-2900 m/s [91]. Therefore, when placing filaments of equal dimensions in a 1.5 MRayl propagation medium, the backscatter pressure from any of the 3D printing materials is expected to be about 60% of the backscatter from a nylon scatterer, while producing fewer artefacts. However, because the level of the artefacts will increase with increasing scatterer dimensions, it is important to measure the size of the 3D printed filaments as well as observe their appearance on the ultrasound images. These are the topics of the next two subsections.

4.4.2 Characterization of printing accuracy

The filaments depicted in Figure 4.2 were of approximately rectangular cross section. Table 4.4 summarizes the printing accuracy and resolution obtained using the three materials ABS, PLA and photopolymer. Although FDM printing places 12% of the ABS and PLA filaments incorrectly, no such errors occur with DLP printing of the

DOI:10.15774/PPKE.ITK.2020.001

photopolymer. However, while the sought 0.5 x 0.5 mm dimensions of the filaments are largely maintained with FDM printing, DLP printing causes an approximate lengthening in the axial direction of 0.5 mm.

The relatively poor DLP printing resolution could be due to the relatively deep penetration of the UV radiation during printing (Figure 4.1), which could be corrected by using a different photopolymer with higher optical attenuation, by reducing exposure time or by reducing the designed height of the filaments, that is, by using fewer layers to print the filaments. With respect to the last option, because one of the aims of the current work was to compare FDM printing with DLP printing for phantom printing, this modification was not made, and the 0.5 x 0.5 mm design was kept for the filament target phantoms; the results are described in the next subsection. Nevertheless, it should be noted that standards for nylon filaments require diameters to be less than 0.3 mm [17], and modern phantoms routinely use 0.1 mm filaments. More generally, for a speed of sound of 1540 m/s, a Rayleigh scatterer should have dimensions less than $0.245/f$ mm, where f is the insonation frequency in megahertz. Clinical scanners do not typically exceed 20 MHz, corresponding to a scatterer dimension of 13 µm. These considerations indicate that future work should have this reduction in dimensions as a goal. The plausibility of this goal is supported by the ability of specialized DLP setups to reach < 2 µm resolutions [116]. For now, filaments with the aforestated dimensions are considered.

4.4.3 US characterization of filament target phantoms

In Figure 4.4 are the ultrasound images of the phantoms placed in de-ionized water. When placed midway between the two walls of the phantom (Figure 4.3), a 1 mm movement of the array toward either of the walls caused a negligible change in the ultrasound image. This suggests that the 10 mm distance between the walls was far enough to avoid their reflections from affecting the image.

The images in Figure 4.4 illustrate that although the letters “ITK” are easily recognizable, there appears to be considerable clutter in the images, especially between

DOI:10.15774/PPKE.ITK.2020.001

Accuracy measure	ABS	PLA	Photopolymer
Ratio of correctly placed filaments	88%	88%	100%
Maximum position error of incorrectly placed filament (mm)	1.63 ± 0.36	0.53 ± 0.12	N/A
Ratio of extra threads	4%	0%	0%
Filament target height (mm)	0.59 ± 0.03	0.54 ± 0.05	0.96 ± 0.09
Filament target width (mm)	0.38 ± 0.03	0.34 ± 0.03	0.61 ± 0.03

Table 4.4: Printing accuracy attained using different printing materials, as calculated using the grid of filaments illustrated in Figure4.2. ABS = acrylonitrile butadiene styrene; PLA = polylactic acid. The ratio of correctly placed filaments was calculated from all 26 filaments. The height and width were calculated from the 4 filaments at the edges.

Type of phantom	Axial FWHM (mm)	Axial FWLHM (mm)	Transverse FWHM (mm)
3D printed phantoms			
ABS	0.40 ± 0.06	0.93 ± 0.52	0.51 ± 0.06
PLA	0.47 ± 0.10	0.94 ± 0.33	0.60 ± 0.14
Photopolymer	0.45 ± 0.06	1.14 ± 0.21	0.56 ± 0.05
Reference measurements			
Simulated point	0.48	0.48	0.54
0.1 mm nylon filament	0.65	0.65	0.58

Table 4.5: Resolution parameters of ultrasound images of printed phantoms compared with those of a simulated point scatterer and a true 0.1-mm-diameter nylon filament from a phantom. ABS = acrylonitrile butadiene styrene; PLA = polylactic acid.; FWLHM = full width at last half-maximum. The axial FWLHM values indicate the necessity of printing filaments with smaller diameter.

DOI:10.15774/PPKE.ITK.2020.001

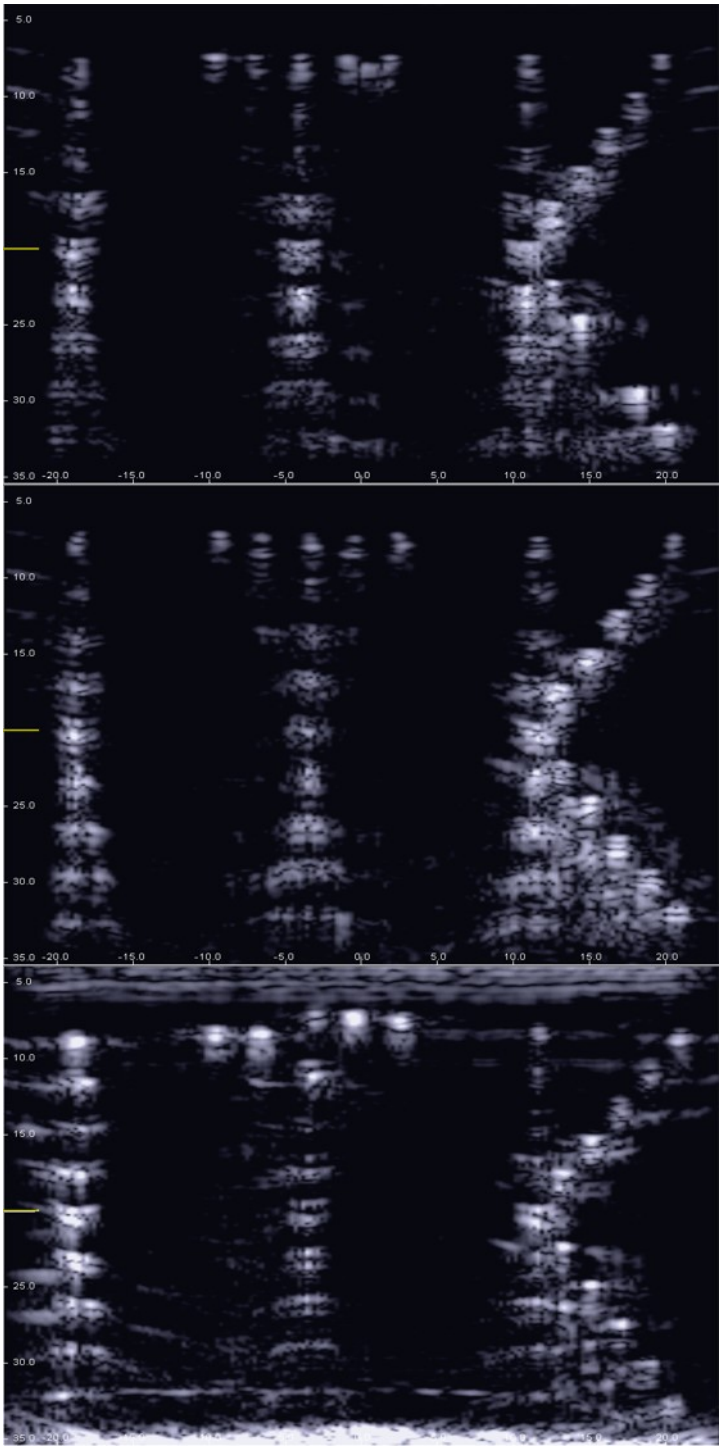

Figure 4.4: Ultrasound images of acrylonitrile butadiene styrene (top), polylactic acid (center) and digital light processing (bottom) phantoms in Figure 4.3 after placement in de-ionized water. The 20 mm transmit focus is indicated with a yellow line on the left side of the images (this also corresponds to the elevational focus of the linear array). The pattern of letters "ITK" is clearly identifiable. However, there is evidence of multiple reflections from each filament.

DOI:10.15774/PPKE.ITK.2020.001

the two legs of the letter 'K'. Some of this clutter could be reduced by replacing water as propagation medium with a gel containing an attenuating substance such as aluminum oxide [117]. Clutter is arguably also made worse by out-of-focus blurring in the imaging system, and it would be interesting to test the phantoms using a better depth of focus or even compound imaging. Nevertheless, even at the focus, there is evidence of multiple reflections from the filament targets. To test this hypothesis, consider Table 4.5, which outlines the spatial extent of the filament target responses at the focus. Although the axial FWHM values of the phantoms are even less than those obtained using reference images of a simulated point scatterer and real commercial phantom filament target, the axial FWLHM values suggest an axial response prolonged by about 0.5 mm. This is hypothesized to be due to reflection from the back wall of the filament targets, and highlights the importance of making the height of the filaments smaller. The transverse FWHM does not seem to be adversely affected by the filament dimensions; however, with a higher-resolution imaging system, it is probable that this dimension should be reduced as well.

4.5 Conclusions

The current work has investigated the feasibility of printing filament target phantoms using inexpensive FDM and DLP 3D printing technology. The materials used were found to have appropriate acoustic properties for scatterers. Immersing the phantom in the desired propagation medium (in the current case, de-ionized water; in the case of gels, before setting) is expected to result in the desired mean acoustic properties. A large number of filaments at desired positions can be easily placed using the described methods, pointing the way to the printing of more complex structures.

There are, however, some limitations to the methods. In FDM printing, around 12% of the filaments are incorrectly positioned, with the incorrectly positioned filaments being misplaced by up to 2 mm. By its nature, DLP does not suffer from such a limitation. However, using the current experimental setups, both the FDM and DLP methods suffer from a lack of printing resolution, with filament heights of

DOI:10.15774/PPKE.ITK.2020.001

around 0.5 and 1.0 mm, respectively. Ultrasound images of phantoms revealed that this resulted in an axial image width larger than that of the 100-mm-diameter nylon filament target of a commercial phantom or the simulated image of a point scatterer. Therefore, printing resolution needs to improve. Although FDM is limited by extrusion size (in the current setup, 0.35 mm), it is thought that DLP printing, with further refinements in the experimental methods (including printing parameters), will be able to reach sub-wavelength resolutions for typical ultrasound scanners.

Notwithstanding the aforementioned challenges, the current work has provided a useful comparative feasibility study of using FDM and DLP printing, with results pointing to the refinement and adoption of DLP printing. On reaching 0.3 mm resolution, the possibility of printing foam structures to investigate complex 3D scattering structures should also be considered.

DOI:10.15774/PPKE.ITK.2020.001

Chapter 5

Uses of High-Precision Ultrasound Phantoms

Previously, two cost-effective 3D printing methods were presented. However, as it was discussed, the limitations of these methods allowed us to create only 2D wire target phantoms. While the methods fit the means of modestly equipped labs, they are only suitable for investigating low frequency (<4 MHz), 2D ultrasound imaging.

To be able to create more complex and even 3D structures, our attention turned to PJ printing, as these printers could use several types of materials having versatile elasticity at high resolution (usually below 50 microns). Unfortunately, the reported speed of sound of the propagation medium in the case of PJ is 1617 m/s [30, 108], which is higher than 1540 m/s usual value obtained for average soft tissue and also the values measured for myocardial muscle (see Chapter 3). However, this only results in a 5% axial compression of the PSF considering the worst case scenario. Compared to the unique benefit of the technology provided by its high resolution and the opportunity to create fully customizable 3D structures, we consider this disadvantage to be acceptable.

5.1 Introduction

First, it is important to clarify what we mean under the expression 'high-precision ultrasound phantom'. The most elementary component of an ultrasound image is

DOI:10.15774/PPKE.ITK.2020.001

a scatterer, which is in general defined as a sub-wavelength inhomogeneity in the propagation medium. Usually the highest frequency used in diagnostic ultrasound is below 20 MHz. Considering the average speed of sound of human soft tissue (1540 m/s) the wavelength will be equal to 77 microns. Using this 'semi-arbitrary' constraint, a high-precision ultrasound phantom could be defined as follows. Such a phantom should be built up from scatterers comparable to the size of 77 microns. From these scatterers an arbitrary speckle pattern should be built up with a precision around 77 microns.

There are several new application areas of these kind of phantoms. One is quantitative validation of image restoration methods, which is the topic of Section 5.3. It is also possible to mimic a medical ultrasound image, if an adequate algorithm is given. I have developed such an algorithm, which is presented in Section 5.4.

5.2 Photopolymer jetting phantom manufacture

Recent work by Jacquet and colleagues [30] has shown that using PJ technology, phantoms containing high precision scatterer maps can be manufactured. The printer settings need to be modified to limit the polymerization of the support material, thus making it a suitable propagation medium. The Objet series of Stratasys (Eden Prairie, MN, USA) printers are able to create objects within a planar resolution limit of 42 µm and a layer thickness of 16-28 µm, depending on the type of the printer.

As in our lab the most used tool for preliminary phantom simulation is MATLAB, Field II toolbox, it was practical to create the real phantoms based on the parameters of simulations. For this reason, to generate the file used to print the phantom, the scatterer locations were first defined in MATLAB. A MATLAB script was then used to generate an AutoCAD script file ('.scr'), which was imported in AutoCAD 2017. The AutoCAD design was then exported as an '.stl' file recognized by the printer software (Objet Studio, Stratasys, Eden Prairie, MN, USA).

To print the phantoms of the current chapter, an Objet24 printer from Stratasys was used. Similarly to Jacquet et al. [30], the minimally polymerized support

DOI:10.15774/PPKE.ITK.2020.001

Setting name			Setting value
Main Grid	Grid Type		Step Grid
	Grid Width	X	0.09
		Y	0.09
		Z	2
	Grid Step	X	50
		Y	50
		Z	0
Fine Grid	Outline with fine grid		No
	Grid Thickness	X&Y	0
		Z	0.6
	Grid X&Y Sizes	Width	0.09
		Step	0.17
Body outline		X&Y	0.35
		Z	0

Table 5.1: Modified PJ printing parameters. The parameters shown in the table were modified in "File/Build Properties" menu, "Lite Grid" tab in Objet Studioí.

material (FC 705) acted as propagation medium, while the scatterers and the walls were made of VeroWhitePlus (VWP). The VWP wall was placed on 5 sides around the support material to minimize creep of the support material, thereby increasing the accuracy of scatterer placement.

To ensure the support material did not polymerize, the printer settings needed to be modified (see 5.1). These settings are available under File/Build Properties. In the settings of "Main Grid", the grid width should be as small as possible, while for the grid step a large value must be chosen, both for the X-Y printing direction.

Phantom quality and reproducibility

The reproducibility of phantom printing can refer to reproducibility between or within phantoms. While accurate scatterer positioning could be achieved with a

DOI:10.15774/PPKE.ITK.2020.001

judicious choice of printing parameters, it was found that even using the same printer settings, some printed phantoms showed contamination of the propagation medium with scattering material. The reason behind this merits further investigation.

There are two possible sources of these contaminations: I. during the printing procedure VWP mixed to FC 705, II. air bubbles mixed to FC 705 before curing – possibly while the raw material travelled to the printer head. Nevertheless, neither could be proved directly, two 1mm thick test objects filled with FC705 and containing microspheres made of VWP, were examined using an optical microscope. These were compared to a contamination free sample made of raw FC705 material, which was cured manually using a household nail dryer with a 9 W UV lamp. The examination suggests our second assumption; air bubble-like structures were found in the support material. Unfortunately, the reason of contaminations could not be explored by the maintenances to date. Due to the lack of control of the contaminations, only the phantom presented in the current chapter could be manufactured.

Although scatterer diameters as low as 50 µm could be printed (see Figure 5.1), setting it to 100 µm substantially reduced variations in scatterer diameter. In the current work always this setting was used to create scatterers in phantoms.

As regards variations of scatterer printing within phantoms, in the next section Figure 5.3 shows the B-mode image of a successfully printed typical phantom. It can be observed that the lateral variation of the scatterer responses around the outer frame is relatively small compared to the axial variation. This suggests that the scatterer diameters are fairly reproducible, with the relatively high amplitude of the response at 20 mm hypothesized to be due to elevational focusing of the transducer. As judged by the location of the outer ring of scatterers, the scatterer placement is also accurate.

PJ phantom limitations

As well as other phantom manufacturing techniques, PJ printing also suffers from some limiting factors. As a non-fully polymerized support material is used for the propagation medium (which is vulnerable for physical interactions by its nature),

DOI:10.15774/PPKE.ITK.2020.001

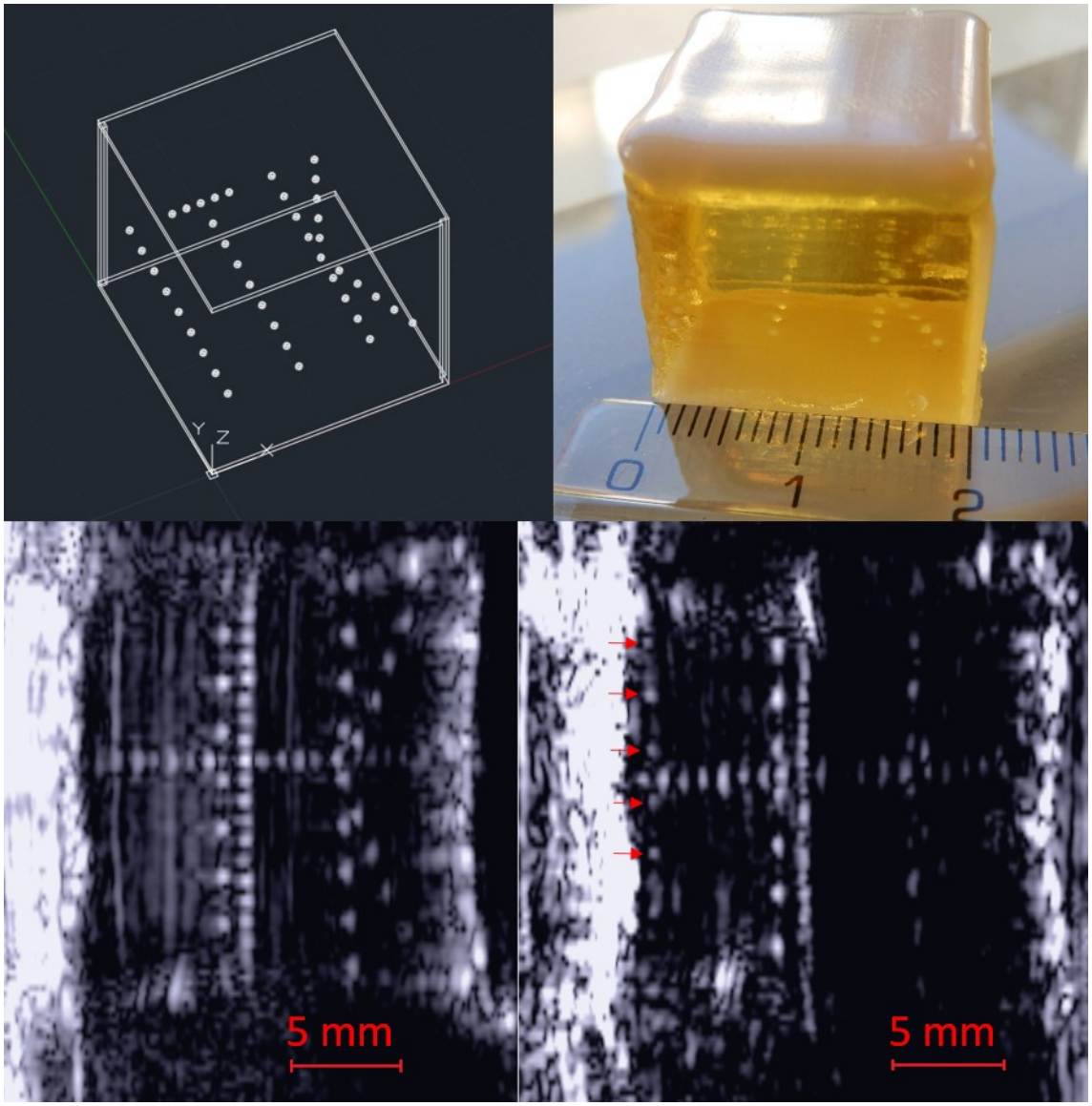

Figure 5.1: PJ phantom trial with different scatterer sizes. Letters of ITK acronym are printed using 50, 100 and 150 micron diameter VWP scatterers respectively. On the right bottom image the visibility of 50 micron spheres are demonstrated and for better visibility also red arrows pointing on them. As it can be seen, at that size the printer was not able to precisely print these scatterers. In contrast the 100 micron diameter scatterers are well visible. In these images a cross like structure is also visible, built up from dense points. With the modification of support structure grid parameters as shown in Table 5.1 this structure was disappeared.

sensitivity against UV radiation, physical interactions and storage conditions are both introduce difficulties in its usage. It was also observed that FC 705 and VWP

DOI:10.15774/PPKE.ITK.2020.001

are sensitive to water, thus for imaging unpolymerized FC 705 liquid is recommended for acoustic coupling. This material does not harm rubber/epoxy transducer surfaces, however, skin contact should be avoided as the raw liquid is irritating. For further information see 'OBJET SUPPORT SUP705' safety data sheet available on the website of the manufacturer. Storing the phantom in a dry and dark environment could lenghten its life cycle over a year.

Comparison of 3D printing methods in phantom manufacture

There are advantages of both three methods presented so far (FDM, DLP, PJ), thus mainly the goal of phantom manufacture will determine which one to use.

It was shown that considering FDM and DLP methods, widespread and cost effective solutions exist (even our 'home made' 3D printer worked well for DLP). However, consequently, fine tuning of these methods to the level of PJ printing are lacking if even possible. The resolution of FDM will always be limited by extruder size, while quality of DLP printing is determined by the resolution and quality of the optics used in the exact projector and also the viscosity of the photopolymer.

In contrast, PJ printers have a much higher price, but able to reach considerably higher resolution, due to the more standardized production cycle. Due to the fact that PJ printers are mostly used in the industry, the available materials are also more standardized (often only OEM) than those that are used in FDM and DLP printing.

Based on our experience, FDM and DLP printing are best fit for low cost, 'in house' calibration and test phantom manufacture for 2D imagers. Using a tuned DLP setup even imagers operating at higher frequencies could be well tested as well as the quantitative investigation of the performance of image enhancement algorithms would be feasible. Also, stereolithography (SLA) printers should be considered as an alternative.

Nevertheless, it should be considered that in a wire target phantom instead of the point spread function only the line spread function could be investigated. Thus, importance of phantoms, which are able to mimic the point spread function in 3D, is incontestable. Currently, only PJ printing offers such an opportunity, so despite

DOI:10.15774/PPKE.ITK.2020.001

its above-mentioned deficiencies, it would be a very useful and easy to use tool.

As a further development idea, creating a custom 3D printer using a hybrid technology combining gel-based bioprinting and DLP/SLA also emerged. Despite – due to the estimated development and validation time – its implementation was decided to be rejected, a brief description follows.

As one of the most common materials in in-lab ultrasound phantom manufacture is agarose-gel, similar could be used as propagation material built up layer-by-layer. The liquid could be doped with a heat or UV sensitive material, which finally should form the scatterers (projecting UV light to the top of the layers or using 2D LASER sweep at the desired locations of the scatterers).The simplest way would be to use proteins, which suffers irreversible denaturation by the UV light or heat impact. However, the main issue in the case of heat sensitive materials would be that the agarose-gel form crosslinks only after heating the solution over 90 °C and only highly stable special proteins [118] could be used. In the case of UV sensitive materials the longevity and long-term temporal behaviour of the phantoms would be problematic. Other possibility is the placement of e.g. glass or polystyrene microspheres as scatterers on the top of a created layer of propagation medium. For this, a precise microfluidic system should be also designed.

5.3 Validation of image restoration methods

5.3.1 Introduction

Image restoration problem

As discussed in Chapter 2, the resolution of ultrasound images depends on the central frequency and bandwidth of the imaging system, as well as the physical properties of the propagating medium. Using the convolutional model of image formation presented in Chapter 2, the RF ultrasound image y can be approximated by the shift-invariant convolution of the original scattering function x with the imaging system response or point spread function h [119]:

$$y = h * x + n \tag{5.1}$$

DOI:10.15774/PPKE.ITK.2020.001

where $*$ is the 2D convolution operator and n is additive noise, often assumed to be zero mean Gaussian white noise. Thus, the resolution of the image is limited by the bandwidth of the point spread function h, and image restoration or resolution enhancement consists of restoring out of bandwidth data. This is a well known ill-posed problem. To solve this problem, additional assumptions about x are thus required by adding a regularization term into the cost function to be minimized and to find x. Assuming x is distributed as generalized Gaussian (random) variable with parameter p, the minimization problem becomes:

$$argmin_x \left|\left|y - h * x\right|\right|_2 + \lambda \left|\left|x\right|\right|_p \tag{5.2}$$

where λ expresses the relative contribution of the prior term and p determines the nature of the sparsity assumption. With $p = 2$, the problem becomes the classical least-squares Tikhonov regularization, while values closer to 0 impose a stronger sparsity assumption. Many approaches exist for solving Equation 5.2; for more information, the reader is directed to [120, 121]. One of the most used methods is the alternating direction method of multipliers (ADMM) [122].

Validation of image restoration

Given the plethora of image restoration algorithms available, the question arises as to their applicability for real ultrasound images. Assuming the shift-invariant convolution model is accurate, simulations provide a method of checking solutions against a ground truth. However, any limitations of the model may degrade real-life results. For instance, shift-variance of h [123] may need to be accounted for by splitting the image into blocks, and even without shift-invariance, errors in estimating h may lead to restoration errors. In addition, non-linear propagation and/or scattering will also invalidate the model, the latter often causing image degradation that is partially responsible for image clutter [124].

Previous work has shown that a collection of polystyrene microspheres aligned on a planar surface may be used to investigate the validity of the shift-invariant convolution model [63]. This in turn may be used to assess the performance of image restoration methods. However, the method in [63] is limited as it does not allow

DOI:10.15774/PPKE.ITK.2020.001

precise positioning of the microspheres. Alternate possibilities are laser printing and transfer of patterns onto a phantom surface [29] or printing of filaments using low-cost 3D-printing technology [26]. However, neither methods allow the positioning of spherical scatterers in a 3D volume.

As it was shown in the previous section, the PJ technology offers a high degree of flexibility when creating customized 3D structures. Here, this capability is explored for creating a desired scattering function and assessing the accuracy of a recently published fast image restoration algorithm based on ADMM numerical optimization scheme [125, 126].

5.3.2 Methods

Phantom design

The PJ phantom was designed to contain: an outer frame of scatterers to check for the consistency of the printed scatterers and the point spread function h (the latter only expected to change in the axial direction); and an inner frame with a high concentration of scatterers so as to generate speckle (Figure 5.2). The diameter of the spheres was set to 100 µm, which was found to be the smallest size that could be printed with reliable size (for details see Section 5.2). All scatterers were placed at least 10 mm from the walls to minimize the effect of reflections from them.

Imaging

The ultrasound images were obtained using uniform delay ('plane-wave') emission from a 47.0 mm aperture, 3.3-10.0 MHz linear array (LA522E) connected to an ULA-OP Research US system. Thus, only elevational focus of the array transducer (equals 20 mm axial distance) could slightly distort the obtained images.

Previous experiments on FC 705 have shown that water absorption causes cracking and degradation of the material. Therefore, instead of a water-based gel, the unpolymerized support material was used as acoustic coupling between the transducer and the phantom.

DOI:10.15774/PPKE.ITK.2020.001

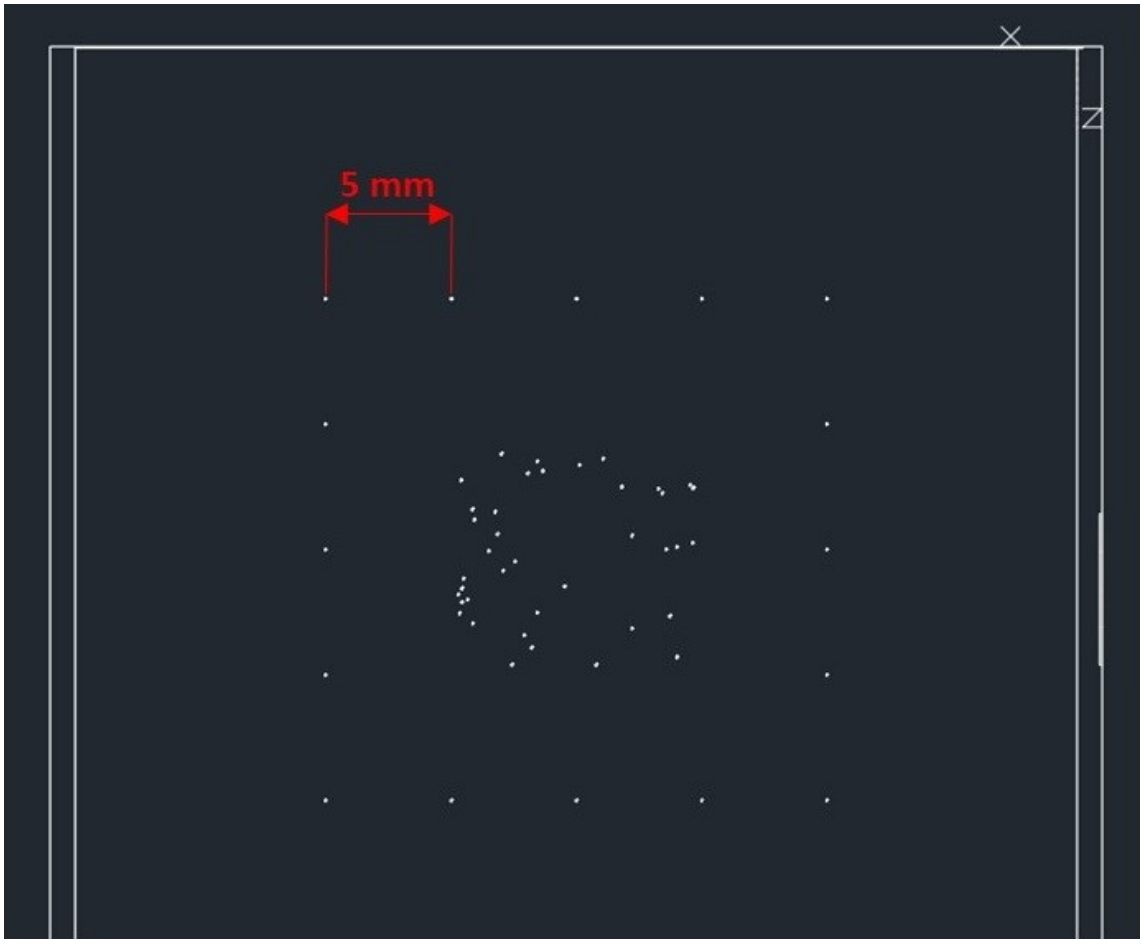

Figure 5.2: Design of PJ SR test phantom. Phantom design. In the outer frame, spheres were placed at 5 mm distances to each other and at least 10 mm from the walls. In the middle 10×10 mm region, 40 spheres were placed at random X-Z positions.

The center frequency of the array was set to 4MHz. The propagation speed was set to that of the photopolymer gel obtained experimentally (1660 m/s). The ultrasound wavelength was therefore 415 µm, yielding ka=0.76, that is, a fair (if imperfect) approximation to a point scatterer.

Further signal processing was carried out in MATLAB. Digital time gain compensation (TGC) was applied to compensate for acoustic attenuation, and hard thresholding was used to eliminate noise in regions without scatterers.

DOI:10.15774/PPKE.ITK.2020.001

Assessment of image restoration accuracy

The image restoration algorithm follows a recently developed fast, iterative, ADMM-based, lp-norm-regularized deconvolution method [125]. Although any $0 < p \leq 2$ could be chosen, to make the investigation tractable, $p = 0.5$ and 2 were compared, as they provided a good contrast between a highly sparse and a non-sparse solution. The algorithm-specific parameters [125] were manually set by cross-validation to their best values.

To estimate the point spread function h, the response to one of the scatterers on the outer frame was recorded. A 2-D parabolic window was applied to h in order to avoid edge effects during the deconvolution procedure.

Two measures of image restoration accuracy were used. The lateral and axial FWHM of an isolated scatterer on the outer frame of the phantom was calculated. The inner frame was used to calculate the normalized root mean square error (RMSE) of the true scattering function estimates.

5.3.3 Results and discussion

Assessment of image restoration accuracy

Figure 5.3 shows a comparison of the scattering function, the resulting B-mode image, and deconvolved images for $p = 0.5$ and 2. It can be observed that the spatial response to the outer frame of scatterers is made more spatially compact by deconvolution. Furthermore, many scatterers in the center of the images are close enough that they cannot be distinguished on the B-mode image, while deconvolution allows the separation of many of these scatterers. However, the difference between the deconvolved images for $p = 0.5$ and 2 is more difficult to ascertain visually and calls for the use of metrics.

Table 5.2 lists the resulting FWHM and RMSE values. For the settings used, $p = 0.5$ offers a higher spatial resolution gain than $p = 2$, and also provides a higher estimation accuracy of the scattering function in terms of RMSE. However, it can also be observed qualitatively that $p = 0.5$ has a tendency to amplify noise. Indeed, for other settings, $p = 0.5$ still yields better values of FWHM than $p = 0.5$ but with

DOI:10.15774/PPKE.ITK.2020.001

similar RMSE values, arguably due to increased noise.

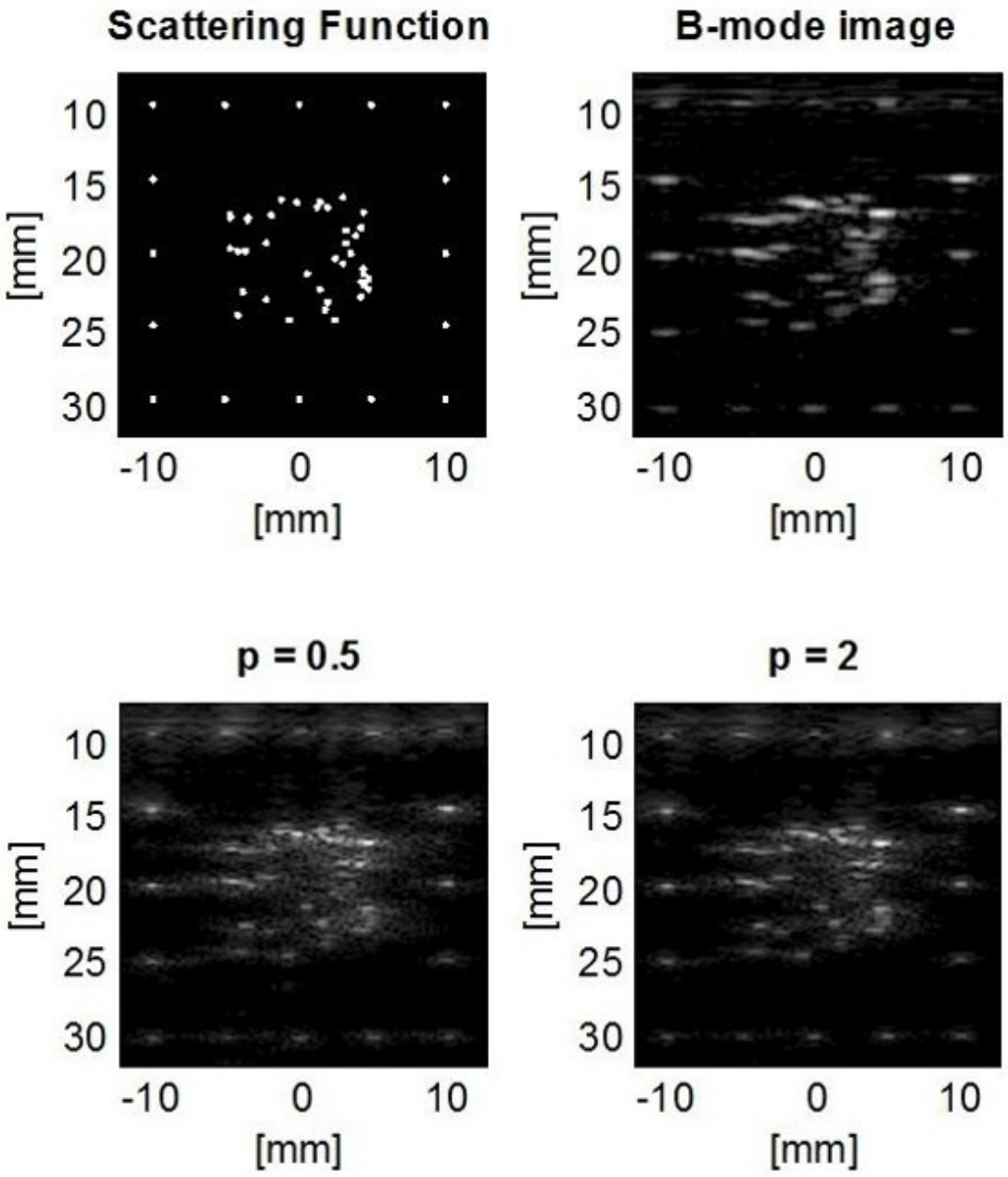

Figure 5.3: Scattering function of our phantom, the obtained B-mode image and two resulting images of the algorithms using $p = 0.5$ and 2 norm. Clusters of unresolvable scatterers became distinguishable in the center region.

A meaningful definition of the SNR still needs to be established that can quantify

DOI:10.15774/PPKE.ITK.2020.001

	B-mode image	Restored image (p=0.5)	Restored image (p=2)
$FWHM_x$ (mm)	1.42	0.78	0.98
$FWHM_z$ (mm)	0.37	0.26	0.27
RMSE	2.34	1.87	1.93

Table 5.2: Axial and transverse FWHM values of a single scatterer from the outer frame of the phantom shows an improvement in resolution using $p = 0.5$ and $p = 2$ norms. RMSE values obtained using the inner random scatterer pattern.

the effect of noise amplification. In the current work, the SNR had been calculated using a region of the image containing both signal and noise and a region containing just noise (due to orthogonality, the variances of signal and noise levels can be assumed to be additive). However, the measure gave misleading results since the noise levels in the region with and without signal were not necessarily the same.

5.4 A stippling algorithm to generate equivalent point scatterer distributions from US images

5.4.1 Introduction

The current section investigates the feasibility of PJ printing to mimic real US images speckle-by-speckle. As it was shown previously, knowing the scattering function of an image could help us to quantitatively analyze the performance of an image enhancement algorithm. Also, more reliable phantoms could be manufactured for training purposes or even to analyze sensitivity of ultrasound based security systems to spoofing attacks, as currently used techniques only mimic tissues on a macroscopic level.

To achieve adequate mimicking, a sparse representation of US images is needed. Mathematically, this is similar to the model described by Equation 5.2 at $p = 0$, however, considering the current problem, only local sparsity is required. Knowing the system PSF, a locally sparse map of scatterers is aimed to be generated using

DOI:10.15774/PPKE.ITK.2020.001

deconvolution and decimation on the original B-mode image. Thus, SF could be fitted the resolution of our printer.

5.4.2 Methods

Stippling algorithm

To be able to mimic US images using PJ, a sparse scattering function (SF) x of ultrasound images y must be created, using the idea of equivalent scatterers [60,127], or in other words a stippling algorithm (SA). SA is named after the artistic method of representing an image by a series of dots according to local density. Our method consists of two main steps as described below.

Step I: Wiener deconvolution of a RF image, using the PSF of the imaging system. The output of this step is denoted as x_{Wnr}. The PSF was previously extracted from a B-mode image of a 3D printed ultrasound phantom (see Section 5.3, Figure 5.3) at 10mm Z depth [27]. To avoid errors in the deconvolution, side regions of the PSF were smoothed using a Gaussian window of the same size as the PSF.

Step II: Decimation of the Wiener deconvolved image (x_{Wnr}). Setting the minimal distance between the scatterers in the X and Z directions (Dx,Dz) is one of the most important parameters, taking into account the printing quality/resolution of the used 3D printer (i.e. Objet 24 by Stratasys). Here Dx was set to 200 µm and Dz was set to 75 µm, the latter taking into account the higher variability of the RF data in the Z direction as well. The algorithm finds iteratively the global maximum of $|x_{Wnr}|$, then the value belonging to the index of actual maximum is stored in the decimated SF representation (x_{pnt}). Finally, a predefined Dx,Dz neighbourhood of the maximum is zeroed out in x_{Wnr}. The algorithm stops when maximum value in $|x_{Wnr}|$ reaches an intensity threshold or a maximal number of scatterers. The minimum threshold for absolute scatterer intensity (typically it was set about 1-10% according to estimated noise level) is able to remove noise from the solution to a certain level. However, similarly to noise-to-signal power ratio (NSR) parameter of Wiener deconvolution, on real images it is should be set experimentally.

DOI:10.15774/PPKE.ITK.2020.001

Matching pursuit

Our algorithm is compared to the well-known matching pursuit (MP) algorithm. At each step, the correlation coefficient (R) was calculated between the estimated SF of the algorithm and the input image. The algorithm ran for 5000 iterations or until the correlation coefficient R_I became smaller than the mean of the previous ten; the highest correlation coefficient was not included in the latest ten calculated R. The output is defined as the SF corresponding to the highest R.

Test data

Two randomly distributed scatterer maps were generated - a sparse and a dense one. US image simulations were obtained using 2D convolution of the scatterer maps with the PSF. A grayscale image of a cat was also processed to create simulated ultrasound images. To compare the noise-sensitivity of the algorithms -20dB white Gaussian noise were added to both.

To evaluate our algorithm on real-life examples, an ultrasound image of a 3D printed phantom and an image of a carotid artery were used. In the case of the phantom, the location of the scatterers were known a priori. Due to the sparse scatterer distribution, denoising in the pre-processing step was more effective than in the case of the carotid image, where simply the average of 100 scans was used. The US images were obtained using uniform delay ('plane-wave') emission from a 47.0 mm, 3.3-10.0 MHz linear array (LA522E) connected to an ULA-OP Research US system.

5.4.3 Results and discussion

Random pattern simulations

The MP and our own SA algorithm performed similarly for random pattern simulations. Adding -20 dB of Gaussian white noise degraded the results in all cases in terms of the correlation coefficient between the reference image and the resulting US images. However, SA performed $R^2 > 0.84$ in each case, while MP gave $R^2 > 0.66$.

DOI:10.15774/PPKE.ITK.2020.001

Simulations using a cat photo

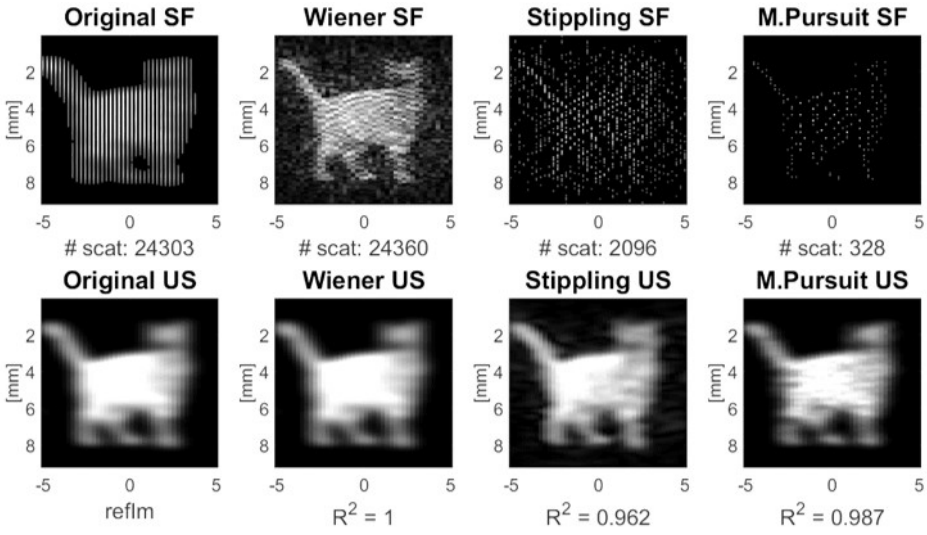

Figure 5.4: Synthetic SF-s and US images of a cat.

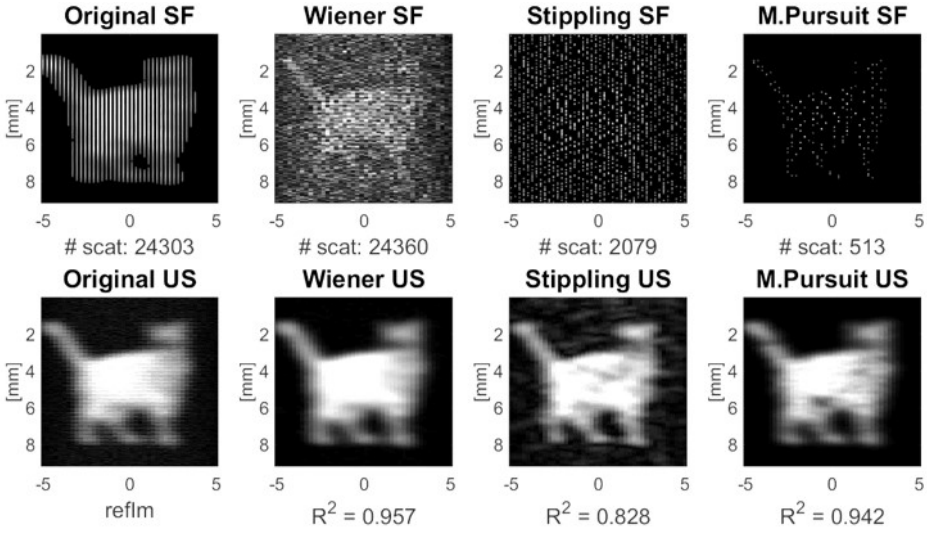

Figure 5.5: Synthetic SF-s and US images of a cat. -20dB Gaussian white noise had been added to the reference image.

As it is shown in Figure 5.4 and Figure 5.5, MP performs better for these images than SA. Presumably, this is due to the dense scatterer distribution on the original SF, because MP does not require local sparsity as SA does, hence noisy, dense structures could be restored better. The NSR parameter for the Wiener-deconvolution

DOI:10.15774/PPKE.ITK.2020.001

step was first set according to the noise level used for the simulations for both images. Interestingly, using 0.1 for noiseless image as well did not affected significantly the results.

Real ultrasound images

In Figure 5.6, the results for a 3D printed phantom are shown. Better results in the sense of R^2 values of SA ($R^2 = 0.932$ vs. $R^2 = 0.832$) is due to the relatively sparse scatterer distribution of the phantom. The NSR parameter for the Wiener-deconvolution step here was set first according to the noise level obtained in the previous section ('Validation of image restoration methods'). However, as discussed there, the NSR could be distorted slightly. For this reason, both for the image of the phantom and the carotid US images, the NSR parameter was adjusted empirically.

Interestingly, SA outperforms MP using a real US image of a carotid artery (Figure 5.7). Compared to the synthetic cat image, the real image contains more speckle, leading us to expect better results (R^2 >0.8).

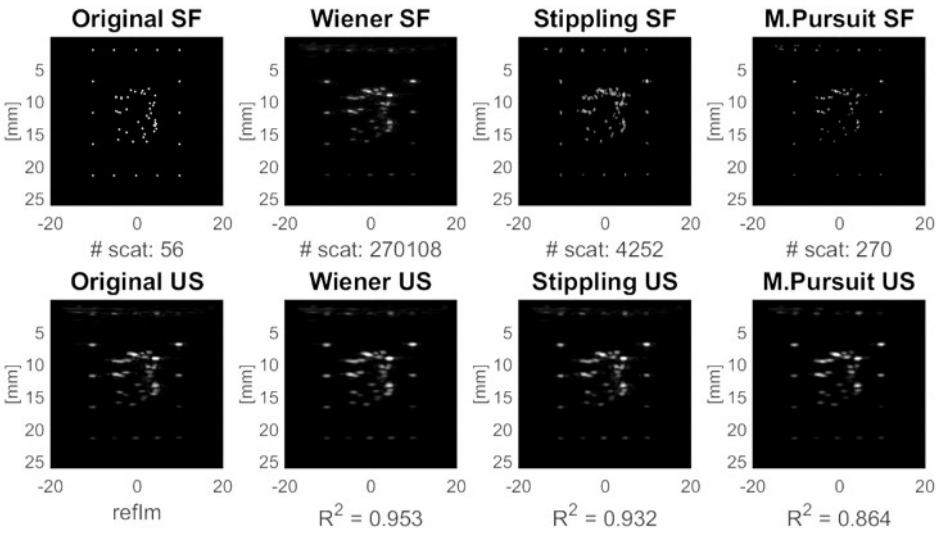

Figure 5.6: Images show the SF and the original and resulting ultrasound images of the 3D printed phantom. SA performed better than MP, even though for MP, local sparsity is not a requirement.

DOI:10.15774/PPKE.ITK.2020.001

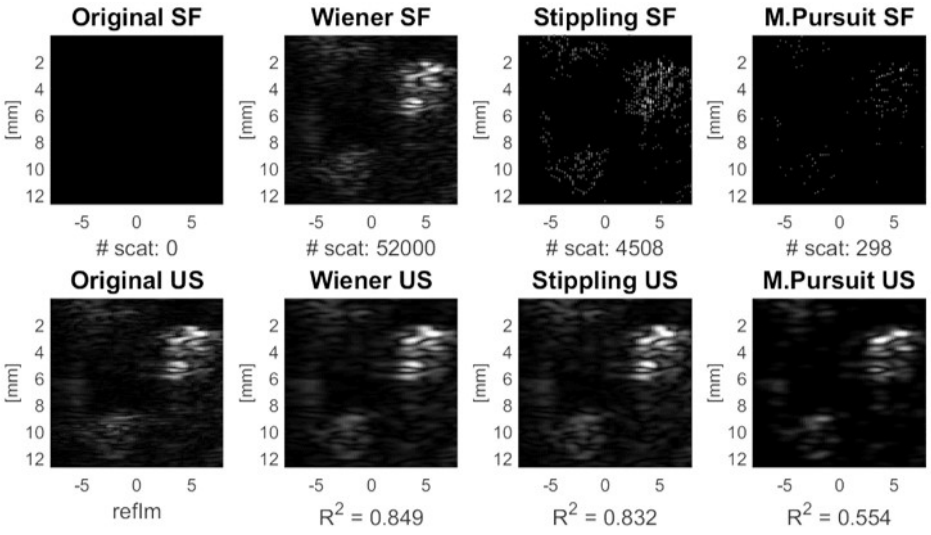

Figure 5.7: Images of a carotid artery. Here the original SF is unknown.

The right choice of the NSR parameter is critical in the Wiener deconvolution step. In the current work NSR values were determined empirically for real images. For simulated images, a modest value (< 1) works well universally. However, in the case of real images, the NSR value for Wiener deconvolution must be higher (i.e. 10 for the phantom and 100 for the carotid artery) to achieve the best result. One possible reason is the higher levels of noise, however, the reason why such (unrealistic) high values are needed merits further investigation. A possible reason could be the spatial variability of the experimental PSF and difficulties in accurately estimating it.

A possible solution could be to print scatterers at different depths – similarly to the 'frame' of the currently used phantom – and acquiring the PSF from them at different depths. Thus, applying the SA for different partitions of the image according to the PSF acquired from the corresponding partition, similarity between the original image and the resulting phantom could be further optimized.

5.5 Conclusions

The first part of the current work has shown how PJ 3D printing technology can – with a careful choice of settings – be used to print phantoms with a known scattering

DOI:10.15774/PPKE.ITK.2020.001

function. This allows the testing and quantitative comparison of image restoration methods, using metrics such as the RMSE to measure the difference of the solution from the true scattering function. Although the current method is limited to the use of a single scatterer material, some PJ printers allows the use of several materials, offering even greater flexibility in setting the scattering function. Moreover, modification of the support material could also lower the experimentally obtained speed of sound of 1660 m/s closer to tissue (generally assumed to be around 1540 m/s), or at least to the reported value of 1617 m/s [30, 31]. In addition to modification of the scattering and propagation materials, further work needs to establish realistic scattering functions for tissue that can be used as realistic test beds for image enhancement techniques.

Section 5.4 has shown that SA is able to create a locally sparse SF, while the resulting US images correlated well ($R^2 > 0.83$) with the original US images. However, the resulting SF (by SA) contains negative values as well, which means at those positions the local density should be reduced in a 3D printed phantom. This could be technically challenging using PJ printing with FC705 as the propagation medium [27, 30]. Future work should therefore focus on modifying the algorithm to force a positive SF, or on developing a novel 3D printing method that does not suffer from this limitation.

DOI:10.15774/PPKE.ITK.2020.001

Chapter 6

Summary

6.1 New scientific results

Thesis I: *I characterized the propagation speed of sound and acoustic attenuation, as well as the temperature dependence of the aforesaid parameters in porcine myocardium. The results confirm the feasibility of ultrasound in the monitoring of thermal therapy and show what properties a realistic muscle-tissue model should have.*

Corresponding publication: [25]

The temperature dependence of soft tissue acoustic properties is relevant for monitoring tissue hyperthermia and also when manufacturing customized tissue-mimicking ultrasound phantoms.

Therefore I investigated the propagation speed and attenuation of healthy porcine left ventricular myocardia ($N = 5$) in a frequency range relevant for clinical diagnostic imaging, i.e. $2.5 - 13.0$ MHz. Each tissue sample was held in a water bath at a temperature $T = 25\,^{\circ}\mathrm{C}$, heated to $45\,^{\circ}\mathrm{C}$, and allowed to cool back down to $25\,^{\circ}\mathrm{C}$. Due to initial tissue swelling, the data for decreasing temperatures was considered more reliable. In this case, the slope of the phase velocity versus temperature relation was measured to be 1.10 ± 0.04 m/s/ $^{\circ}$C, and the slope of the attenuation was 0.11 ± 0.04 dB/cm/ $^{\circ}$C at 10 MHz, or -0.0041 ± 0.0015 dB/cm/MHz$^{1.4336}$/ $^{\circ}$C as a function of frequency.

DOI:10.15774/PPKE.ITK.2020.001

Thesis II: *I compared the feasibility of two rapid 3D-prototyping methods in creating ultrasound phantoms. I have shown that Fused Deposition Modelling (FDM) and Digital Light Processing (DLP) are able to print ultrasound wire phantoms for 2D imaging at the resolution of 0.3mm, which is suitable for ultrasound imagers employing frequencies below 4 MHz.*

Corresponding publication: [26]

Recently, the use of 3D printing for manufacturing ultrasound phantoms has only emerged using expensive and complex technology of photopolymer jetting. Keeping in mind the modest means of many research laboratories, two reliable and cost-effective 3D printing methods were developed for phantom manufacturing, namely fused deposition modelling and digital light processing techniques.

After successful trials, wire target phantoms were printed and tested using both techniques. One photopolymer material was used in the custom-manufactured DLP printer and several other materials (ABS, PLA and TPU) in the FDM printer. Except TPU, the results of the prints were satisfactory and could be used as calibration phantoms, thus the achievements were published.

Thesis III: *I developed a method with which ultrasound phantoms can be manufactured using Photopolymer Jetting technology.*

The use of photopolymer jetting in the manufacture of ultrasound phantoms has been shown previously by Jacquet et. al. [30], however, a full description of the setup and parameters used was lacking. I developed a method with which FC705 support material could be printed to be a suitable propagation medium for ultrasound imaging. In my phantoms Vero White Plus serves as the material of scatterers and the enclosing wall.

DOI:10.15774/PPKE.ITK.2020.001

Thesis III.a.: *I have shown that such phantoms can be used to quantitatively test super-resolution algorithms.*

Corresponding publication: [27]

Ultrasound images are usually covered with speckle noise. This speckle pattern is originating from sub-wavelength scatterers, however, it makes the images hard to interpret to the user, moreover introduces additional uncertainty to measurements. Super-resolution algorithms are aiming to improve image quality and in parallel reduce measurement errors. Despite the importance to have quantitative feedback, testing of these algorithms usually includes only simulation results and presents in-vivo examples in a qualitative fashion. Using my custom manufactured phantoms I could measure quantitatively the effect of a super-resolution algorithm on FWHM and RMSE parameters of real ultrasound images.

Thesis III.b.: *I developed an algorithm with which arbitrary medical ultrasound images could be well ($R^2 \geq 80\,\%$) approximated and physically realized.*

Corresponding publication: [28]

In ultrasound imaging current phantoms can mimic tissues only on a macroscopic scale. One of the main reasons for this is the lack of usage of 3D printing methods – and looking into deeper, the lack of suitable 3D printing materials – in phantom manufacture. Relying on the previous results using photopolymer jetting technology I developed an iterative algorithm (Stippling Algorithm - SA), which is able to calculate the 2D (axial and lateral) position and intensity of scatterers based on a post-beamformed RF ultrasound image. A further advantage of the algorithm is that it is scalable to the resolution of any 3D-printer.

DOI:10.15774/PPKE.ITK.2020.001

Bibliography

[1] C. Hill, J. Bamber, and G. ter Haar, *Physical Principles of Medical Ultrasonics*, 2nd ed. Wiley, New York, 2004.

[2] J. Tsujino, M. Hongoh, R. Tanaka, R. Onoguchi, and T. Ueoka, "Ultrasonic plastic welding using fundamental and higher resonance frequencies," *Ultrasonics*, vol. 40, no. 1-8, pp. 375–378, may 2002.

[3] R. Adhami and P. Meenen, "Fingerprinting for security," *IEEE Potentials*, vol. 20, no. 3, pp. 33–38, 2001.

[4] R. J. Przybyla, S. E. Shelton, A. Guedes, I. I. Izyumin, M. H. Kline, D. A. Horsley, and B. E. Boser, "In-air rangefinding with an AlN piezoelectric micromachined ultrasound transducer," *IEEE Sensors Journal*, vol. 11, no. 11, pp. 2690–2697, nov 2011.

[5] S. C. Boon, K. R. Maile, W. J. Linder, P. Huelskamp, and R. Vijayagopal, "Method and apparatus for intra-body ultrasound communication," Patent, Oct. 16, 2012, uS Patent 8,290,598.

[6] T. L. Szabo, *Diagnostic Ultrasound Imaging: Inside Out*. Elsevier Science, 2004. [Online]. Available: https://www.ebook.de/de/product/15167690/thomas_l_szabo_diagnostic_ultrasound_imaging_inside_out.html

[7] J. Hatvani, A. Horvath, J. Michetti, A. Basarab, D. Kouame, and M. Gyongy, "Deep learning-based super-resolution applied to dental computed tomography," *IEEE Transactions on Radiation and Plasma Medical Sciences*, pp. 1–1, 2018.

DOI:10.15774/PPKE.ITK.2020.001

[8] G. Matrone, A. S. Savoia, G. Caliano, and G. Magenes, "The delay multiply and sum beamforming algorithm in ultrasound b-mode medical imaging," *IEEE Transactions on Medical Imaging*, vol. 34, no. 4, pp. 940–949, apr 2015.

[9] M. Mozaffarzadeh, M. Sadeghi, A. Mahloojifar, and M. Orooji, "Double-stage delay multiply and sum beamforming algorithm applied to ultrasound medical imaging," *Ultrasound in Medicine & Biology*, vol. 44, no. 3, pp. 677–686, mar 2018.

[10] T. Misaridis and J. Jensen, "Use of modulated excitation signals in medical ultrasound. part III: high frame rate imaging," *IEEE Transactions on Ultrasonics, Ferroelectrics and Frequency Control*, vol. 52, no. 2, pp. 208–219, feb 2005.

[11] R. B. Stamm and R. P. Martin, "Quantification of pressure gradients across stenotic valves by doppler ultrasound," *Journal of the American College of Cardiology*, vol. 2, no. 4, pp. 707–718, oct 1983.

[12] D. J. Robson and J. C. Flaxman, "Measurement of the end-diastolic pressure gradient and mitral valve area in mitral stenosis by doppler ultrasound," *European Heart Journal*, vol. 5, no. 8, pp. 660–667, aug 1984.

[13] M. Pasternak, E. Samset, J. D'hooge, and G. U. Haugen, "Temperature monitoring by channel data delays: Feasibility based on estimated delays magnitude for cardiac ablation," *Ultrasonics*, vol. 77, pp. 32–37, may 2017.

[14] M. O. Culjat, D. Goldenberg, P. Tewari, and R. S. Singh, "A review of tissue substitutes for ultrasound imaging," *Ultrasound in Medicine & Biology*, vol. 36, no. 6, pp. 861–873, jun 2010.

[15] F. Duck, *Physical properties of tissue.* San Diego: Academic Press, 1990.

[16] E. Filoux, J. Mamou, O. Aristizabal, and J. A. Ketterling, "Characterization of the spatial resolution of different high-frequency imaging systems using a novel anechoic-sphere phantom," *IEEE Transactions on Ultrasonics, Ferroelectrics and Frequency Control*, vol. 58, no. 5, pp. 994–1005, may 2011.

DOI:10.15774/PPKE.ITK.2020.001

[17] M. M. Goodsitt, P. L. Carson, S. Witt, D. L. Hykes, and J. M. Kofler, "Real-time B-mode ultrasound quality control test procedures. report of AAPM ultrasound task group no. 1," *Medical Physics*, vol. 25, no. 8, pp. 1385–1406, aug 1998.

[18] E. J. Boote, "Phantoms for ultrasound experimentation and quality control," in *The Phantoms of Medical and Health Physics*. Springer New York, nov 2014, pp. 159–179.

[19] K. Füzesi, "Ultrasound tissue-mimicking phantoms," 2016.

[20] F. Fani, E. Schena, P. Saccomandi, and S. Silvestri, "CT-based thermometry: An overview," *International Journal of Hyperthermia*, vol. 30, no. 4, pp. 219–227, jun 2014.

[21] L. E. Kinsler, *Fundamentals of acoustics*. Wiley, 1982. [Online]. Available: https://books.google.hu/books?id=i7MPAQAAMAAJ

[22] E. Constans. The acoustic wave equation. Last accessed: 2015. february. [Online]. Available: http://constans.pbworks.com/w/file/63957324/8.TheAcousticWaveEquation.docx

[23] R. S. C. Cobbold, *Foundations of Biomedical Ultrasound*. OXFORD UNIV PR, 2006. [Online]. Available: https://www.ebook.de/de/product/5362477/richard_s_c_cobbold_foundations_of_biomedical_ultrasound.html

[24] R. S. C. Cobbold, N. V. Sushilov, and A. C. Weathermon, "Transient propagation in media with classical or power-law loss," *The Journal of the Acoustical Society of America*, vol. 116, no. 6, pp. 3294–3303, dec 2004.

[25] K. Füzesi, N. Ilyina, E. Verboven, K. V. D. Abeele, M. Gyöngy, and J. D'hooge, "Temperature dependence of speed of sound and attenuation of porcine left ventricular myocardium," *Ultrasonics*, vol. 82, pp. 246–251, jan 2018.

DOI:10.15774/PPKE.ITK.2020.001

[26] K. Füzesi and M. Gyöngy, "Comparison of two inexpensive rapid prototyping methods for manufacturing filament target ultrasound phantoms," *Ultrasound in Medicine & Biology*, vol. 43, no. 3, pp. 712–720, mar 2017.

[27] K. Füzesi, A. Basarab, G. Cserey, D. Kouamé, and M. Gyöngy, "Validation of image restoration methods on 3d-printed ultrasound phantoms," in *2017 IEEE International Ultrasonics Symposium (IUS)*. IEEE, sep 2017.

[28] K. Füzesi, Á. Makra, and M. Gyöngy, "A stippling algorithm to generate equivalent point scatterer distributions from ultrasound images," in *Proceedings of Meetings on Acoustics 6ICU*. Acoustical Society of America, 2017.

[29] K. Füzesi, "Development of a pvc-based ultrasound phantom," Faculty of Information Technology and Bionics, Pázmány Péter Catholic University, Tech. Rep., 2015.

[30] J.-R. Jacquet, F. Levassort, F. Ossant, and J.-M. Grégoire, "3d printed phantom for high frequency ultrasound imaging," in *Ultrasonics Symposium (IUS), 2015 IEEE International*. IEEE, 2015, pp. 1–4.

[31] J.-R. Jacquet, F. Ossant, F. Levassort, and J.-M. Gregoire, "3-d-printed phantom fabricated by photopolymer jetting technology for high-frequency ultrasound imaging," *IEEE Transactions on Ultrasonics, Ferroelectrics, and Frequency Control*, vol. 65, no. 6, pp. 1048–1055, jun 2018.

[32] K. Zell, J. I. Sperl, M. W. Vogel, R. Niessner, and C. Haisch, "Acoustical properties of selected tissue phantom materials for ultrasound imaging," *Physics in Medicine and Biology*, vol. 52, no. 20, pp. N475–N484, oct 2007.

[33] A. Cafarelli, A. Verbeni, A. Poliziani, P. Dario, A. Menciassi, and L. Ricotti, "Tuning acoustic and mechanical properties of materials for ultrasound phantoms and smart substrates for cell cultures," *Acta Biomaterialia*, vol. 49, pp. 368–378, feb 2017.

DOI:10.15774/PPKE.ITK.2020.001

[34] G. Menikou and C. Damianou, "Acoustic and thermal characterization of agar based phantoms used for evaluating focused ultrasound exposures," *Journal of Therapeutic Ultrasound*, vol. 5, no. 1, jun 2017.

[35] H. Pierce, "TU-c-202-01: Ultrasound phantoms: B-mode, doppler mode and others," *Medical Physics*, vol. 37, no. 6Part14, pp. 3388–3388, jun 2010.

[36] N. Hungr, J.-A. Long, V. Beix, and J. Troccaz, "A realistic deformable prostate phantom for multimodal imaging and needle-insertion procedures," *Medical Physics*, vol. 39, no. 4, pp. 2031–2041, mar 2012.

[37] A. Pacioni, M. Carbone, C. Freschi, R. Viglialoro, V. Ferrari, and M. Ferrari, "Patient-specific ultrasound liver phantom: materials and fabrication method," *International Journal of Computer Assisted Radiology and Surgery*, vol. 10, no. 7, pp. 1065–1075, oct 2014.

[38] F. Adams, T. Qiu, A. Mark, B. Fritz, L. Kramer, D. Schlager, U. Wetterauer, A. Miernik, and P. Fischer, "Soft 3d-printed phantom of the human kidney with collecting system," *Annals of Biomedical Engineering*, vol. 45, no. 4, pp. 963–972, nov 2016.

[39] J. An, J. E. M. Teoh, R. Suntornnond, and C. K. Chua, "Design and 3d printing of scaffolds and tissues," *Engineering*, vol. 1, no. 2, pp. 261–268, jun 2015.

[40] S. F. S. Shirazi, S. Gharehkhani, M. Mehrali, H. Yarmand, H. S. C. Metselaar, N. A. Kadri, and N. A. A. Osman, "A review on powder-based additive manufacturing for tissue engineering: selective laser sintering and inkjet 3d printing," *Science and Technology of Advanced Materials*, vol. 16, no. 3, p. 033502, jun 2015.

[41] M. Gatto, G. Memoli, A. Shaw, N. Sadhoo, P. Gelat, and R. A. Harris, "Three-dimensional printing (3dp) of neonatal head phantom for ultrasound: Thermocouple embedding and simulation of bone," *Medical Engineering & Physics*, vol. 34, no. 7, pp. 929–937, sep 2012.

DOI:10.15774/PPKE.ITK.2020.001

[42] S. J. West, J.-M. Mari, A. Khan, J. H. Y. Wan, W. Zhu, I. G. Koutsakos, M. Rowe, D. Kamming, and A. E. Desjardins, "Development of an ultrasound phantom for spinal injections with 3-dimensional printing," *Regional Anesthesia and Pain Medicine*, vol. 39, no. 5, pp. 429–433, 2014.

[43] J. Young, J. Coles-Black, I. Chao, and M. Barrington, "Steps on how a phantom can be 3d printed and embedded within a medium suitable for training of ultrasound-guided procedures," *Journal of 3D Printing in Medicine*, vol. 1, no. 3, pp. 149–154, jul 2017.

[44] M. Gyöngy, "Passive cavitation mapping for monitoring ultrasound therapy," 2010.

[45] Y. Zhou, "Noninvasive thermometry in high-intensity focused ultrasound ablation," *Ultrasound Quarterly*, vol. 33, no. 4, pp. 253–260, dec 2017.

[46] E. Schena, F. Giurazza, C. Massaroni, Y. Fong, J. J. Park, and P. Saccomandi, "Thermometry based on computed tomography images during microwave ablation: Trials on ex vivo porcine liver," in *2017 IEEE International Instrumentation and Measurement Technology Conference (I2MTC)*. IEEE, may 2017.

[47] E. V. Petrova, H. P. Brecht, M. Motamedi, A. A. Oraevsky, and S. A. Ermilov, "In vivo optoacoustic temperature imaging for image-guided cryotherapy of prostate cancer," *Physics in Medicine & Biology*, vol. 63, no. 6, p. 064002, mar 2018.

[48] A. A. Anosov, A. S. Kazansky, P. V. Subochev, A. D. Mansfeld, and V. V. Klinshov, "Passive estimation of internal temperatures making use of broadband ultrasound radiated by the body," *The Journal of the Acoustical Society of America*, vol. 137, no. 4, pp. 1667–1674, apr 2015.

[49] A. Anosov, P. Subochev, A. Mansfeld, and A. Sharakshane, "Physical and computer-based modeling in internal temperature reconstruction by the

DOI:10.15774/PPKE.ITK.2020.001

method of passive acoustic thermometry," *Ultrasonics*, vol. 82, pp. 336–344, jan 2018.

[50] E. S. Ebbini, C. Simon, and D. Liu, "Real-time ultrasound thermography and thermometry [life sciences]," *IEEE Signal Processing Magazine*, vol. 35, no. 2, pp. 166–174, mar 2018.

[51] J. Bamber and C. Hill, "Ultrasonic attenuation and propagation speed in mammalian tissues as a function of temperature," *Ultrasound in Medicine & Biology*, vol. 5, no. 2, pp. 149–157, jan 1979.

[52] I. McRury and D. Haines, "Ablation for the treatment of arrhythmias," *Proceedings of the IEEE*, vol. 84, no. 3, pp. 404–416, mar 1996.

[53] E. Bertaglia, F. Zoppo, C. Tondo, A. Colella, R. Mantovan, G. Senatore, N. Bottoni, G. Carreras, L. Corò, P. Turco, M. Mantica, and G. Stabile, "Early complications of pulmonary vein catheter ablation for atrial fibrillation: A multicenter prospective registry on procedural safety," *Heart Rhythm*, vol. 4, no. 10, pp. 1265–1271, oct 2007.

[54] Y. Ni, S. Mulier, Y. Miao, L. Michel, and G. Marchal, "A review of the general aspects of radiofrequency ablation," *Abdominal Imaging*, vol. 30, no. 4, pp. 381–400, mar 2005.

[55] D. P. Redfearn, G. M. Trim, A. C. Skanes, B. Petrellis, A. D. Krahn, R. Yee, and G. J. Klein, "Esophageal temperature monitoring during radiofrequency ablation of atrial fibrillation," *Journal of Cardiovascular Electrophysiology*, vol. 16, no. 6, pp. 589–593, jun 2005.

[56] S. M. Singh, A. d'Avila, S. K. Doshi, W. R. Brugge, R. A. Bedford, T. Mela, J. N. Ruskin, and V. Y. Reddy, "Esophageal injury and temperature monitoring during atrial fibrillation ablation," *Circulation: Arrhythmia and Electrophysiology*, vol. 1, no. 3, pp. 162–168, jun 2008.

[57] P. Müller, J.-W. Dietrich, P. Halbfass, A. Abouarab, F. Fochler, A. Szöllösi, K. Nentwich, M. Roos, J. Krug, A. Schade, A. Mügge, and T. Deneke, "Higher

incidence of esophageal lesions after ablation of atrial fibrillation related to the use of esophageal temperature probes," *Heart Rhythm*, vol. 12, no. 7, pp. 1464–1469, jul 2015.

[58] A. Koh, S. R. Gutbrod, J. D. Meyers, C. Lu, R. C. Webb, G. Shin, Y. Li, S.-K. Kang, Y. Huang, I. R. Efimov, and J. A. Rogers, "Ultrathin injectable sensors of temperature, thermal conductivity, and heat capacity for cardiac ablation monitoring," *Advanced Healthcare Materials*, vol. 5, no. 3, pp. 373–381, dec 2015.

[59] M. G. Daly, I. Melton, G. Roper, G. Lim, and I. G. Crozier, "High-resolution infrared thermography of esophageal temperature during radiofrequency ablation of atrial fibrillation," *Circulation: Arrhythmia and Electrophysiology*, vol. 11, no. 2, p. e005667, feb 2018.

[60] R. G. Dantas, E. T. Costa, and S. Leeman, "Ultrasound speckle and equivalent scatterers," *Ultrasonics*, vol. 43, no. 6, pp. 405–420, may 2005.

[61] M. E. Anderson and G. E. Trahey, "A seminar on k-space applied to medical ultrasound," *Department of Biomedical Engineering, Duke University*, 2000.

[62] O. Michailovich and A. Tannenbaum, "Despeckling of medical ultrasound images," *IEEE Transactions on Ultrasonics, Ferroelectrics and Frequency Control*, vol. 53, no. 1, pp. 64–78, jan 2006.

[63] M. Gyöngy and Á. Makra, "Experimental validation of a convolution- based ultrasound image formation model using a planar arrangement of micrometer-scale scatterers," *IEEE Transactions on Ultrasonics, Ferroelectrics, and Frequency Control*, vol. 62, no. 6, pp. 1211–1219, jun 2015.

[64] F. Dunn, M. Tanaka, S. Ohtsuki, and Y. Saijo, Eds., *Ultrasonic Tissue Characterization*. Springer Japan, 1996.

[65] V. A. D. Grosso and C. W. Mader, "Speed of sound in pure water," *The Journal of the Acoustical Society of America*, vol. 52, no. 5B, pp. 1442–1446, nov 1972.

[66] O. Corporation. Tables of acoustic properties of materials. [Online]. Available: http://www.ondacorp.com/tecref_acoustictable.shtml

[67] H. Calkins, K. H. Kuck, R. Cappato, J. Brugada, A. J. Camm, S.-A. Chen, H. J. Crijns, R. J. Damiano, D. W. Davies, J. DiMarco *et al.*, "2012 hrs/ehra/ecas expert consensus statement on catheter and surgical ablation of atrial fibrillation [...]," *Heart rhythm*, vol. 9, no. 4, pp. 632–696, 2012.

[68] H. Calkins, E. Prystowsky, M. Carlson, L. S. Klein, J. P. Saul, and P. Gillette, "Temperature monitoring during radiofrequency catheter ablation procedures using closed loop control. atakr multicenter investigators group," *Circulation*, vol. 90, no. 3, pp. 1279–1286, sep 1994.

[69] W. Kwiecinski, F. Bessière, E. C. Colas, W. A. N'Djin, M. Tanter, C. Lafon, and M. Pernot, "Cardiac shear-wave elastography using a transesophageal transducer: application to the mapping of thermal lesions in ultrasound transesophageal cardiac ablation," *Physics in Medicine & Biology*, vol. 60, no. 20, p. 7829, 2015.

[70] Y.-S. Hsiao, R. E. Kumon, and C. X. Deng, "Characterization of lesion formation and bubble activities during high-intensity focused ultrasound ablation using temperature-derived parameters," *Infrared Physics & Technology*, vol. 60, pp. 108–117, sep 2013.

[71] C. Damianou and K. Hynynen, "The effect of various physical parameters on the size and shape of necrosed tissue volume during ultrasound surgery," *The Journal of the Acoustical Society of America*, vol. 95, no. 3, pp. 1641–1649, mar 1994.

[72] D. E. Haines, "The biophysics of radiofrequency catheter ablation in the heart: The importance of temperature monitoring," *Pacing and Clinical Electrophysiology*, vol. 16, no. 3, pp. 586–591, mar 1993.

[73] J. Lu, H. Ying, Z. Sun, M. Motamedi, B. Bell, and L. Sheppard, "In vitro measurement of speed of sound during coagulate tissue heating," in *Ultrasonics*

Symposium, 1996. Proceedings., 1996 IEEE, vol. 2. IEEE, 1996, pp. 1299–1302.

[74] A. Worthington and M. Sherar, "Changes in ultrasound properties of porcine kidney tissue during heating," *Ultrasound in Medicine & Biology*, vol. 27, no. 5, pp. 673–682, may 2001.

[75] C. A. Damianou, N. T. Sanghvi, F. J. Fry, and R. Maass-Moreno, "Dependence of ultrasonic attenuation and absorption in dog soft tissues on temperature and thermal dose," *The Journal of the Acoustical Society of America*, vol. 102, no. 1, pp. 628–634, jul 1997.

[76] E. D. Verdonk, S. A. Wickline, and J. G. Miller, "Anisotropy of ultrasonic velocity and elastic properties in normal human myocardium," *The Journal of the Acoustical Society of America*, vol. 92, no. 6, pp. 3039–3050, 1992.

[77] K. R. Marutyan, M. Yang, S. L. Baldwin, K. D. Wallace, M. R. Holland, and J. G. Miller, "The frequency dependence of ultrasonic velocity and the anisotropy of dispersion in both freshly excised and formalin-fixed myocardium," *Ultrasound in Medicine & Biology*, vol. 32, no. 4, pp. 603–610, apr 2006.

[78] S. L. Baldwin, M. Yang, K. R. Marutyan, K. D. Wallace, M. R. Holland, and J. G. Miller, "Measurements of the anisotropy of ultrasonic velocity in freshly excised and formalin-fixed myocardial tissue," *The Journal of the Acoustical Society of America*, vol. 118, no. 1, pp. 505–513, 2005.

[79] E. D. Verdonk, B. K. Hoffmeister, S. A. Wickline, and J. G. Miller, "Anisotropy of the slope of ultrasonic attenuation in formalin fixed human myocardium," *The Journal of the Acoustical Society of America*, vol. 99, no. 6, pp. 3837–3843, jun 1996.

[80] S. L. Baldwin, K. R. Marutyan, M. Yang, K. D. Wallace, M. R. Holland, and J. G. Miller, "Measurements of the anisotropy of ultrasonic attenuation in

freshly excised myocardium," *The Journal of the Acoustical Society of America*, vol. 119, no. 5, pp. 3130–3139, 2006.

[81] M. O'Donnell, J. W. Mimbs, B. E. Sobel, and J. G. Miller, "Ultrasonic attenuation of myocardial tissue: Dependence on time after excision and on temperature," *The Journal of the Acoustical Society of America*, vol. 62, no. 4, pp. 1054–1057, oct 1977.

[82] C. H. Seo, D. N. Stephens, J. Cannata, A. Dentinger, F. Lin, S. Park, D. Wildes, K. E. Thomenius, P. Chen, T. Nguyen, A. de La Rama, J. S. Jeong, A. Mahajan, K. Shivkumar, A. Nikoozadeh, O. Oralkan, U. Truong, D. J. Sahn, P. T. Khuri-Yakub, and M. O'Donnell, "The feasibility of using thermal strain imaging to regulate energy delivery during intracardiac radio-frequency ablation," *IEEE Transactions on Ultrasonics, Ferroelectrics and Frequency Control*, vol. 58, no. 7, pp. 1406–1417, jul 2011.

[83] P. Baki, S. J. Sanabria, G. Kosa, G. Szekely, and O. Goksel, "Thermal expansion imaging for monitoring lesion depth using m-mode ultrasound during cardiac RF ablation: in vitro study," *International Journal of Computer Assisted Radiology and Surgery*, vol. 10, no. 6, pp. 681–693, apr 2015.

[84] R. M. Arthur, W. L. Straube, J. W. Trobaugh, and E. G. Moros, "Noninvasive estimation of hyperthermia temperatures with ultrasound," *International Journal of Hyperthermia*, vol. 21, no. 6, pp. 589–600, sep 2005.

[85] E. C. Verboven, "Feasibility study of the ultrasonic dispersion characteristics of contrast agent enriched media for radiation dosimetry," 2011.

[86] R. L. Nasoni, T. Bowen, W. G. Connor, and R. R. Sholes, "In vivo temperature dependence of ultrasound speed in tissue and its application to noninvasive temperature monitoring," *Ultrasonic Imaging*, vol. 1, no. 1, pp. 34–43, jan 1979.

[87] N. P. L. (UK). Tables of physical & chemical constants. [Online]. Available: http://www.kayelaby.npl.co.uk./general_physics/2_4/2_4_6.html

DOI:10.15774/PPKE.ITK.2020.001

[88] C. Zanini, E. Gerbaudo, E. Ercole, A. Vendramin, and M. Forni, "Evaluation of two commercial and three home-made fixatives for the substitution of formalin: a formaldehyde–free laboratory is possible," *Environmental Health*, vol. 11, no. 1, p. 59, 2012.

[89] H. Azhari, "Appendix a: typical acoustic properties of tissues," *Basics of Biomedical Ultrasound for Engineers*, pp. 313–314, 2010.

[90] G. D. Ludwig, "The velocity of sound through tissues and the acoustic impedance of tissues," *The Journal of the Acoustical Society of America*, vol. 22, no. 6, pp. 862–866, 1950.

[91] A. Selfridge, "Approximate material properties in isotropic materials," *IEEE Transactions on Sonics and Ultrasonics*, vol. 32, no. 3, pp. 381–394, may 1985.

[92] J. Miller, D. Yuhas, J. Mimbs, S. Dierker, L. Busse, J. Laterra, A. Weiss, and B. Sobel, "Ultrasonic tissue characterization: Correlation between biochemical and ultrasonic indices of myocardial injury," in *1976 Ultrasonics Symposium*. IEEE, 1976, pp. 33–43.

[93] M. O'Donnell, J. W. Mimbs, and J. G. Miller, "The relationship between collagen and ultrasonic attenuation in myocardial tissue," *The Journal of the Acoustical Society of America*, vol. 65, no. 2, pp. 512–517, feb 1979.

[94] R. T. Towa, R. J. Miller, L. A. Frizzell, J. F. Zachary, and W. D. O'Brien, "Attenuation coefficient and propagation speed estimates of rat and pig intercostal tissue as a function of temperature," *ieee transactions on ultrasonics, ferroelectrics, and frequency control*, vol. 49, no. 10, pp. 1411–1420, 2002.

[95] C. M. Sehgal, "Quantitative relationship between tissue composition and scattering of ultrasound," *The Journal of the Acoustical Society of America*, vol. 94, no. 4, pp. 1944–1952, oct 1993.

[96] J. Browne, K. Ramnarine, A. Watson, and P. Hoskins, "Assessment of the acoustic properties of common tissue-mimicking test phantoms," *Ultrasound in Medicine & Biology*, vol. 29, no. 7, pp. 1053–1060, jul 2003.

[97] M. K. Chmarra, R. Hansen, R. Maarvik, and T. Langø, "Multimodal phantom of liver tissue," *PLoS ONE*, vol. 8, no. 5, p. e64180, may 2013.

[98] "Acr-aapm technical standard for diagnostic medical physics performance monitoring of real time ultrasound equipment." 2016.

[99] C. Kollmann, C. deKorte, N. Dudley, N. Gritzmann, K. Martin, and D. Evans, "Guideline for technical quality assurance (TQA) of ultrasound devices (b-mode) – version 1.0 (july 2012)," *Ultraschall in der Medizin - European Journal of Ultrasound*, vol. 33, no. 06, pp. 544–549, nov 2012.

[100] C. M. Moran, W. Ellis, S. D. Pye, and S. Smart, "Characterising the performance of a high resolution ultrasound scanner for pre-clinical ultrasound imaging," in *2008 IEEE Ultrasonics Symposium*. IEEE, nov 2008.

[101] A. Shaw and R. Hekkenberg, *Standards to support performance evaluation for diagnostic ultrasound imaging equipment*. National Physical Laboratory, 2007.

[102] D. E. Rowland, V. R. Newey, D. P. Turner, and D. K. Nassiri, "The automated assessment of ultrasound scanner lateral and slice thickness resolution: Use of the step response," *Ultrasound in Medicine & Biology*, vol. 35, no. 9, pp. 1525–1534, sep 2009.

[103] S. D. Pye and W. Ellis, "The resolution integral as a metric of performance for diagnostic grey-scale imaging," *Journal of Physics: Conference Series*, vol. 279, p. 012009, feb 2011.

[104] S. D. Pye, W. Ellis, and T. MacGillivray, "Medical ultrasound: a new metric of performance for grey-scale imaging," *Journal of Physics: Conference Series*, vol. 1, pp. 187–192, jan 2004.

[105] J. Li and P. Stoica, *Robust adaptive beamforming*. John Wiley & Sons, 2005, vol. 88.

[106] C.-I. Nilsen and I. Hafizovic, "Beamspace adaptive beamforming for ultrasound imaging," *IEEE Transactions on Ultrasonics, Ferroelectrics and Frequency Control*, vol. 56, no. 10, pp. 2187–2197, oct 2009.

[107] S. M. Sakhaei, "A decimated minimum variance beamformer applied to ultrasound imaging," *Ultrasonics*, vol. 59, pp. 119–127, may 2015.

[108] A. J. Cloonan, D. Shahmirzadi, R. X. Li, B. J. Doyle, E. E. Konofagou, and T. M. McGloughlin, "3d-printed tissue-mimicking phantoms for medical imaging and computational validation applications," *3D Printing and Additive Manufacturing*, vol. 1, no. 1, pp. 14–23, mar 2014.

[109] C. Hill, J. Bamber, and G. ter Haar, *Physical principles of medical ultrasonics*. Chichester: Wiley, 2004, vol. Vol. 2.

[110] J. Jensen and N. Svendsen, "Calculation of pressure fields from arbitrarily shaped, apodized, and excited ultrasound transducers," *IEEE Transactions on Ultrasonics, Ferroelectrics and Frequency Control*, vol. 39, no. 2, pp. 262–267, mar 1992.

[111] J. A. Jensen, "Field: A program for simulating ultrasound systems," in *10th Nordbaltic Conference on Biomedical Imaging, Vol. 4, Suppl. 1, Part 1: 351–353*. Citeseer, 1996.

[112] A. B. y Jimenez, I. Seviaryna, M. Sain, and E. Y. Maeva, "Acoustic, tomographic, and morphological properties of bismaleimide-modified PLA green composites," *Journal of Reinforced Plastics and Composites*, vol. 30, no. 16, pp. 1329–1340, aug 2011.

[113] T. L. Szabo, "Time domain wave equations for lossy media obeying a frequency power law," *The Journal of the Acoustical Society of America*, vol. 96, no. 1, pp. 491–500, jul 1994.

[114] G. Lévêque, E. Rosenkrantz, and D. Laux, "Correction of diffraction effects in sound velocity and absorption measurements," *Measurement Science and Technology*, vol. 18, no. 11, pp. 3458–3462, sep 2007.

DOI:10.15774/PPKE.ITK.2020.001

[115] K. A. Wear, "Measurement of dependence of backscatter coefficient from cylinders on frequency and diameter using focused transducers—with applications in trabecular bone," *The Journal of the Acoustical Society of America*, vol. 115, no. 1, pp. 66–72, jan 2004.

[116] J.-W. Choi, R. Wicker, S.-H. Lee, K.-H. Choi, C.-S. Ha, and I. Chung, "Fabrication of 3d biocompatible/biodegradable micro-scaffolds using dynamic mask projection microstereolithography," *Journal of Materials Processing Technology*, vol. 209, no. 15-16, pp. 5494–5503, aug 2009.

[117] S. Rajagopal, N. Sadhoo, and B. Zeqiri, "Reference characterisation of sound speed and attenuation of the IEC agar-based tissue-mimicking material up to a frequency of 60 MHz," *Ultrasound in Medicine & Biology*, vol. 41, no. 1, pp. 317–333, jan 2015.

[118] Y. Matsuura, M. Takehira, Y. Joti, K. Ogasahara, T. Tanaka, N. Ono, N. Kunishima, and K. Yutani, "Thermodynamics of protein denaturation at temperatures over 100 °c: CutA1 mutant proteins substituted with hydrophobic and charged residues," *Scientific Reports*, vol. 5, no. 1, oct 2015.

[119] J. C. Bamber and R. J. Dickinson, "Ultrasonic b-scanning: a computer simulation," *Physics in Medicine and Biology*, vol. 25, no. 3, pp. 463–479, may 1980.

[120] M. V. Afonso, J. M. Bioucas-Dias, and M. A. T. Figueiredo, "An augmented lagrangian approach to the constrained optimization formulation of imaging inverse problems," *IEEE Transactions on Image Processing*, vol. 20, no. 3, pp. 681–695, mar 2011.

[121] M. Elad, *Sparse and Redundant Representations*. Springer New York, 2010.

[122] R. Morin, A. Basarab, and D. Kouame, "Alternating direction method of multipliers framework for super-resolution in ultrasound imaging," in *2012 9th IEEE International Symposium on Biomedical Imaging (ISBI)*. IEEE, may 2012.

DOI:10.15774/PPKE.ITK.2020.001

[123] J. Ng, R. Prager, N. Kingsbury, G. Treece, and A. Gee, "Modeling ultrasound imaging as a linear, shift-variant system," *IEEE Transactions on Ultrasonics, Ferroelectrics and Frequency Control*, vol. 53, no. 3, pp. 549–563, mar 2006.

[124] B. Byram, K. Dei, J. Tierney, and D. Dumont, "A model and regularization scheme for ultrasonic beamforming clutter reduction," *IEEE Transactions on Ultrasonics, Ferroelectrics, and Frequency Control*, vol. 62, no. 11, pp. 1913–1927, nov 2015.

[125] N. Zhao, Q. Wei, A. Basarab, N. Dobigeon, D. Kouame, and J.-Y. Tourneret, "Fast single image super-resolution using a new analytical solution for l_2-l_2 problems," *IEEE Transactions on Image Processing*, vol. 25, no. 8, pp. 3683–3697, aug 2016.

[126] N. Zhao, Q. Wei, A. Basarab, D. Kouame, and J.-Y. Tourneret, "Single image super-resolution of medical ultrasound images using a fast algorithm," in *2016 IEEE 13th International Symposium on Biomedical Imaging (ISBI)*. IEEE, apr 2016.

[127] Á. Makra, J. Hatvani, and M. Gyöngy., "Calculation of equivalent ultrasound scatterers using a time-domain method," Pázmány Péter Catholic University, Jedlik Laboratories Reports, Tech. Rep., 2015.

DOI:10.15774/PPKE.ITK.2020.001

Acknowledgements

I would like to express my very great appreciation to my supervisor, Dr. Miklós Gyöngy, who gave me guidance to further improve not only in professional knowledge but in human qualities. I am grateful for the conscientious discussions and his patience even when I made some silly mistakes. Nevertheless, he founded Dermus Ltd. and made superhuman efforts to achieve his dreams and help people suffering from skin disease, he could always find some time to supervise me. I feel honoured working as a colleague in his team both in the university and in Dermus. He is a great inspiration for me and I hope we can continue to work together successfully.

I am grateful to Dr. Jan D'hooge, who gave me opportunity to work in his research group in UZ Gasthuisberg Medical Imaging Research Centre (Leuven, Belgium). Special thanks to Natalia Ilyina for her kind help with through transmission measurements and Christel Huysmans for her help providing tissue samples.

I would like to offer my special thanks to Dr. György Cserey and Dr. György Falk (Varinex ZRt.) for their kind help and guidance in photopolymer jetting 3D printing.

I am particularly grateful for the cooperation in the validation of image enhancement algorithms to Adrian Basarab and Denis Kouamé (IRIT, Toulouse, France).

I would like to thank Janka Hatvani for the discussions and advice she gave, thus improving the quality of the manuscript.

I would also like to acknowledge the constructive and well-detailed critics of the reviewers, which considerably helped the manuscript to be more precise and coherent.

I am also grateful for all my colleagues for their encouragement and also their meritorious critics. I truly believe that one of the best ways to improve our weaknesses is to perceive and process the opinion of others.

Finally, I wish to thank my family for their support and encouragement throughout my studies. I would like to dedicate this thesis to my wife, Kati, and my daughter, Mira, who have always helped me to get through difficulties in my personal life and served as an inexhaustible source of fun.